The Astrophysical Journal, 978:115 (32pp), 2025 January 01 https://doi.org/10.3847/1538-4357/ad9272

Combining Direct Black Hole Mass Measurements and Spatially Resolved Stellar Kinematics to Calibrate the $M_{\rm BH}$–$\sigma_\star$ Relation of Active Galaxies

Nico Winkel[1], Vardha N. Bennert[2], Raymond P. Remigio[3], Tommaso Treu[4], Knud Jahnke[1], Vivian U[3], Aaron J. Barth[3], Matthew Malkan[4], Bernd Husemann[1,5], Xuheng Ding[6], and Simon Birrer[7]
[1] Max-Planck-Institut für Astronomie, Königstuhl 17, D-69117 Heidelberg, Germany; winkel@mpia.de
[2] Physics Department, California Polytechnic State University, San Luis Obispo, CA 93407, USA
[3] Department of Physics and Astronomy, 4129 Frederick Reines Hall, University of California, Irvine, CA 92697, USA
[4] Department of Physics and Astronomy, University of California, Los Angeles, 430 Portola Plaza, Los Angeles, CA 90095, USA
[5] European Organisation for the Exploitation of Meteorological Satellites (EUMETSAT), Eumetsat Allee 1, 64295 Darmstadt, Germany
[6] School of Physics and Technology, Wuhan University, Wuhan 430072, People's Republic of China
[7] Department of Physics and Astronomy, Stony Brook University, Stony Brook, NY 11794, USA
Received 2024 August 26; revised 2024 November 3; accepted 2024 November 12; published 2024 December 30

Abstract

The origin of the tight scaling relation between the mass of supermassive black holes (SMBHs; $M_{\rm BH}$) and their host-galaxy properties remains unclear. Active galactic nuclei (AGNs) probe phases of ongoing SMBH growth and offer the only opportunity to measure $M_{\rm BH}$ beyond the local Universe. However, determining an AGN's host galaxy's stellar velocity dispersion, $\sigma_\star$, and its galaxy dynamical mass, $M_{\rm dyn}$, is complicated by AGN contamination, aperture effects, and different host-galaxy morphologies. We select a sample of AGNs for which $M_{\rm BH}$ has been independently determined to high accuracy by state-of-the-art techniques: dynamical modeling of the reverberation signal and spatially resolving the broad-line region with the Very Large Telescope Interferometer/GRAVITY. Using integral-field spectroscopic observations, we spatially map the host-galaxy stellar kinematics across the galaxy and bulge effective radii. We find that the dynamically hot component of galaxy disks correlates with $M_{\rm BH}$; however, the correlations are tightest for aperture-integrated $\sigma_\star$ measured across the bulge. Accounting for the different $M_{\rm BH}$ distributions, we demonstrate—for the first time—that AGNs follow the same $M_{\rm BH}$–$\sigma_\star$ and $M_{\rm BH}$–$M_{\rm bulge,dyn}$ relations as quiescent galaxies. We confirm that the classical approach of determining the virial factor as a sample average, yielding $\log f = 0.65 \pm 0.18$, is consistent with the average f from individual measurements. The similarity between the underlying scaling relations of AGNs and quiescent galaxies implies that the current AGN phase is too short to have altered black hole masses on a population level. These results strengthen the local calibration of f for measuring single-epoch $M_{\rm BH}$ in the distant Universe.

Unified Astronomy Thesaurus concepts: AGN host galaxies (2017); Active galaxies (17); Supermassive black holes (1663); Scaling relations (2031); Seyfert galaxies (1447); Black hole physics (159); Galaxy evolution (594); Active galactic nuclei (16)

1. Introduction

Supermassive black holes (SMBHs) are located in the hearts of most, if not all, massive galaxies. Their masses $M_{\rm BH}$ form tight correlations with various properties of their host galaxies. Prominent examples include the scaling relations between $M_{\rm BH}$ and bulge stellar mass (J. Magorrian et al. 1998; N. Häring & H.-W. Rix 2004), bulge luminosity (J. Kormendy & D. Richstone 1995; A. Marconi & L. K. Hunt 2003), or bulge stellar velocity dispersion $\sigma_\star$ (L. Ferrarese & D. Merritt 2000; K. Gebhardt et al. 2000; D. Merritt & L. Ferrarese 2001; S. Tremaine et al. 2002; T. Treu et al. 2004). One way to interpret these scaling relations is a coupling between the growth of SMBHs to that of their host galaxies (e.g., L. Ferrarese & D. Merritt 2000; J. Kormendy & L. C. Ho 2013), implying a causal connection between the processes involved. Among the scaling relations, the $M_{\rm BH}$–$\sigma_\star$ correlation stands out as particularly tight. The $M_{\rm BH}$–$\sigma_\star$ relation exhibits a remarkably small intrinsic scatter of ∼0.4 dex over many orders of $M_{\rm BH}$ and host-galaxy mass (K. Gültekin et al. 2009; R. P. Saglia et al. 2016; R. C. E. van den Bosch 2016), providing important insights into SMBH formation scenarios, such as black hole (BH) seeding models (M. Volonteri & P. Natarajan 2009) and models for SMBH-galaxy coevolution (P. F. Hopkins et al. 2006; B. Robertson et al. 2006; H. Mo et al. 2024). Considering the tightness of the relation, and that $\sigma_\star$ is a direct tracer for dynamical mass, the $M_{\rm BH}$–$\sigma_\star$ relation is often interpreted as the most direct probe for the formation and coevolution of SMBHs with their host galaxies (S. Tremaine et al. 2002; A. Beifiori et al. 2012; R. P. Saglia et al. 2016; R. C. E. van den Bosch 2016; S. de Nicola et al. 2019; A. W. Graham 2023). As such, the $M_{\rm BH}$ scaling relations for quiescent galaxies are well established. However, any kind of evolutionary study of the $M_{\rm BH}$ scaling relation relies on $M_{\rm BH}$ measured in active galactic nuclei (AGNs).

The $M_{\rm BH}$ scaling relations in local AGNs are essential for various reasons. For one, broad-line (type 1) AGNs are the objects targeted in reverberation mapping (RM) studies, a unique way to determine the mass of the SMBH. In short, RM observes variability in the accretion-disk luminosity and the time-delayed response of ionized gas in the broad-line region (BLR). While the light travel time provides constraints on the size of the BLR, Doppler-broadened emission lines give the velocity of the BLR clouds. The main uncertainties are due to the unknown geometry and kinematics of the BLR, summarized in the "virial" factor f. A sample-averaged value of f has traditionally been determined assuming that AGNs follow the same $M_{\rm BH}$–$\sigma_\star$ relation as quiescent galaxies. By combining *f* with the empirical relation between BLR radius and luminosity ("*R*–*L* relation"), a single spectrum becomes sufficient for estimating $M_{\rm BH}$ for broad-line AGNs. This estimate is commonly referred to as the single-epoch method, which enables $M_{\rm BH}$ measurements across cosmic time.

Second, host galaxies build up their stellar mass, traced by $\sigma_\star$, through secular processes on $>10^7$ yr timescales, much longer than the duration of single AGN episodes of 10^4–10^6 yr (R. C. Hickox et al. 2014; K. Schawinski et al. 2015). Despite their relatively short lifetimes, the bulk of cosmic SMBH mass growth occurs during luminous AGN phases (A. Merloni 2004; A. Schulze et al. 2015). This implies that $M_{\rm BH}$ in AGNs is growing rapidly compared to the host galaxy, so that AGNs might probe a special state during the evolution of the $M_{\rm BH}$ scaling relations.

Third, AGNs are considered crucial for shaping the $M_{\rm BH}$ scaling relations. The energy from the central accretion disk can significantly affect the host galaxy by either heating the interstellar medium or expelling cold gas, which suppresses star formation and limits the buildup of stellar mass in the bulge (T. Di Matteo et al. 2005; D. J. Croton 2006; R. S. Somerville et al. 2008; Y. Dubois et al. 2013; C. M. Harrison 2017). These processes, collectively known as AGN feedback, can also regulate SMBH growth (Y. Dubois et al. 2012; W. Massonneau et al. 2023). Although the exact timing and mechanisms of AGN feedback are still debated, these effects are expected to influence the $M_{\rm BH}$–$\sigma_\star$ relation: J. Silk & M. J. Rees (1998) predict a slope of $\beta \approx 4$ for momentum-driven feedback, while energy-driven feedback should yield $\beta = 5$ (A. King 2003).

As an alternative to self-regulated SMBH growth, the hierarchical assembly of galaxy mass over cosmic time could create a noncausal link between $M_{\rm BH}$ and host-galaxy properties, mimicking the observed scaling relations (C. Y. Peng 2007; M. Hirschmann et al. 2010; K. Jahnke & A. V. Macciò 2011). To achieve high stellar mass by redshift zero, a galaxy must have experienced multiple mergers, during which the central BHs also merged. If $M_{\rm BH}$ and host-galaxy stellar masses are randomly sampled during each merger, the central limit theorem predicts a correlation between them after several mergers. This scenario suggests that AGN feedback is not necessary for the formation of the ~$M_{\rm BH}$–host-galaxy scaling relations over cosmic time.

All these open questions have continued to spark great interest in the community, in particular whether the $M_{\rm BH}$–galaxy scaling relations of active and inactive galaxies are identical. A series of studies have reported shallower $M_{\rm BH}$–$\sigma_\star$ relations for RM AGNs, while also highlighting the challenge of extracting host-galaxy kinematics in luminous AGNs and the small dynamic range in $M_{\rm BH}$ (J.-H. Woo et al. 2010, 2013; D. Park et al. 2012; M. Batiste et al. 2017b). J.-H. Woo et al. (2015) explain the initial tension by selection effects, which are sufficient to explain this flattening of the AGNs' relation. Indeed, several groups reported that the $M_{\rm BH}$–$\sigma_\star$ relation of AGNs and quiescent galaxies share similar slopes (e.g., F. Shankar et al. 2019; T. Caglar et al. 2020). While larger samples allow the relative slopes to be compared, the offset between the $M_{\rm BH}$–$\sigma_\star$ relation of AGNs and quiescent galaxies remains unconstrained, because it is used to calibrate the sample-average virial factor *f*.

Recent advancements have enabled more robust and independent methods for measuring $M_{\rm BH}$ in AGNs. Compared to classical RM, velocity-resolved BLR lags from high signal-to-noise ratio (S/N) and high-cadence spectroscopic data allow the BLR gas-flow structure to be resolved (e.g., R. D. Blandford & C. F. McKee 1982; K. Horne et al. 2004). For data sets with the highest S/N, it is possible to extract more detailed properties of the BLR. However, the information is convolved with the BLR signal through the so-called transfer function, which describes the intrinsic time-delay distribution of the broad emission line (B. M. Peterson 1993; A. Skielboe et al. 2015). To overcome degeneracies arising from similar BLR geometries, A. Pancoast et al. (2011) have introduced the Bayesian Code for AGN Reverberation and Modeling of Emission Lines (`CARAMEL`). `CARAMEL` provides a phenomenological description of the BLR dynamics, and thereby the inference of the BLR parameters and associated uncertainties in RM data sets. This method yielded precise and independent $M_{\rm BH}$ measurements for a statistically meaningful sample of 30 objects (e.g., B. J. Brewer et al. 2011; Y.-R. Li et al. 2013; A. Pancoast et al. 2014, 2018; P. R. Williams et al. 2018; M. C. Bentz et al. 2022; L. Villafaña et al. 2022; P. R. Williams & T. Treu 2022; for a recent compilation, see Y. Shen et al. 2024).

A novel third method involves spatially resolving the BLR, allowing for independent measurements of $M_{\rm BH}$. What was first deemed impossible due to the small angular size of the BLR ($\sim 10^{-4}$ arcsec) has become technically feasible with GRAVITY, the second-generation near-infrared beam combiner at the Very Large Telescope Interferometer (VLTI). The differential phase measures how the photocenter shifts at different wavelengths of the broad-line emission compared to the continuum. Fitting the full differential phase spectra (rather than the time-resolved RM data) with a BLR model allows the BLR structure and kinematics to be constrained. Based on the same BLR model parameterization as for `CARAMEL` (A. Pancoast et al. 2014), so far six objects have robust $M_{\rm BH}$ from this technique (GRAVITY Collaboration et al. 2018, 2020, 2024). As this approach provides another independent method to constrain $M_{\rm BH}$, this sample is complementary to the AGNs modeled with `CARAMEL`.

In terms of the host galaxy's contribution in shaping the $M_{\rm BH}$–$\sigma_\star$ relation, previous studies suggested a dependence on host morphology. Specifically, galaxies with structures like bars and pseudobulges deviate from the elliptical-only relation seen in quiescent galaxies (e.g., A. W. Graham 2008; J. Hu 2008; K. Gültekin et al. 2009). This morphological dependence is particularly relevant for AGNs, as $\sigma_\star$ measurements are typically based on single-aperture spectra, in which bars and pseudobulges are often unresolved (e.g., A. W. Graham et al. 2011; J.-H. Woo et al. 2013). Aperture-integrated kinematics are often the only diagnostic available when covering a large dynamic range in $M_{\rm BH}$. Consequently, inclination (T. Xiao et al. 2011; J. M. Bellovary et al. 2014), substructures (M. Hartmann et al. 2014), and rotational broadening from the disk contribution are likely impacting various recent calibrations of the AGN $M_{\rm BH}$–$\sigma_\star$ relation, such as, e.g., J.-H. Woo et al. (2015) and T. Caglar et al. (2020, 2023). Long-slit spectroscopy partially addresses this challenge by resolving the host galaxy along the slit axis. Using this technique, V. N. Bennert et al. (2015) demonstrated that $\sigma_\star$ measurements can vary by up to 40% on average across different definitions. Nevertheless, slit orientation relative to substructures, such as bars, can still dramatically impact $\sigma_\star$

(M. Batiste et al. 2017a). M. Batiste et al. (2017b) found a 10% shallower slope for the $M_{\rm BH}$–$\sigma_\star$ relation when accounting for rotational broadening in spatially resolved AGN host galaxies. However, their recalibration is indistinguishable from that of previous studies due to a small sample of only 10 RM AGNs. Likewise, many previous studies suffered from a combination of lacking spatial resolution, poorly constrained $M_{\rm BH}$, and/or limited dynamic range in $M_{\rm BH}$ and $\sigma_\star$. In a recent study, J. Molina et al. (2024) used spatially resolved kinematics from the local AGN population from the Close AGN Reference Survey (CARS; B. Husemann et al. 2022) and Palomar-Green (PG) quasars, reporting no difference between the $M_{\rm BH}$–σ relation in active and inactive galaxies. However, this study is still based on single-epoch BH mass estimates and did not consider selection effects. These limitations have hindered a consistent calibration of the $M_{\rm BH}$–$\sigma_\star$ relation in AGNs and the determination of its intrinsic scatter and trends with AGN parameters or host-galaxy properties.

In this work, we use deep high-spectral-resolution integral-field spectroscopic (IFU) observations to spatially resolve $\sigma_\star$ across various host-galaxy components in a robust local AGN sample. High angular resolution imaging from the Hubble Space Telescope (HST) will be used in a companion paper to decompose the host galaxy into its morphological components (V. N. Bennert et al. 2024, in preparation). We match the apertures for stellar kinematics extraction to the radii determined from imaging, addressing aperture effects to account for differences in galaxy morphologies, AGN luminosities, and distances. This approach ensures a consistent framework for calibrating the $M_{\rm BH}$–$\sigma_\star$ across a wide range of AGN properties.

This paper is organized as follows. Section 2 covers sample selection, while Section 3 details the IFU observations and data reduction, and Section 4 the data analysis. In Section 5, we present and discuss the $M_{\rm BH}$–$\sigma_\star$ relation in the context of previous work. Section 6 provides a summary. The Appendix includes details on fitting procedures, comparisons of different IFU data sets, and the impact of the AGN subtraction method in our 3D spectroscopic data. Throughout this work, we have adopted $H_0 = 67.8$ km/s/Mpc, $\Omega_{\rm m} = 0.308$, and $\Omega_{\rm vac} = 0.692$ (Planck Collaboration et al. 2016). In the following, we refer to the stellar velocity dispersion, commonly denoted as $\sigma_\star$, as σ.

2. Sample Selection

2.1. AGN Sample

The core sample for this work is composed of AGNs with velocity-resolved BLR lags that have been modeled with `CARAMEL`. Since this technique constrains the virial factor f individually ($f_{\rm dyn}$), a major source of systematic uncertainty is eliminated compared to $M_{\rm BH}$ from classical RM (cRM). In other words, AGNs with dynamically modeled $M_{\rm BH}$ provide the most pristine sample for inferring the underlying scaling relations. Furthermore, dynamical modeling reduces the statistical uncertainties of individual measurements from ∼0.4 dex (single epoch) and ∼0.3 dex (cRM) to typically 0.2 dex (A. Pancoast et al. 2014; L. Villafaña et al. 2022). Thanks to a number of recent campaigns, the sample of CARAMEL AGNs has grown to 30 objects (for a recent compilation, see Y. Shen et al. 2024), covering a large range in BH masses and AGN luminosities ($\log(M_{\rm BH}/M_\odot) \sim 6.4{-}8.3\, M_\odot$; $0.01 \leqslant z \leqslant 0.16$).

In addition, we complement the sample with AGNs whose $M_{\rm BH}$ has been measured from spatially resolving the BLR with VLTI/GRAVITY. This has been achieved for a total of seven objects so far (GRAVITY Collaboration et al. 2018, 2020, 2021, 2024), of which NGC 3783 and IC 4329A overlap with the CARAMEL AGN sample. Of the remaining five, we include the four that have deep optical IFU observations plus broadband HST imaging publicly available: Mrk 1239, Mrk 509, IRAS 09149–6206, and 3C 273. In the following, we refer to these six objects as GRAVITY AGNs.

To further increase the range of AGN luminosities, $M_{\rm BH}$, and host morphologies, but without sacrificing data quality, we additionally include the complete set of unobscured AGNs that have (i) $M_{\rm BH}$ determined from cRM, (ii) existing deep optical 3D spectroscopy, and (iii) archival broadband imaging at high angular resolution from HST. In the following, we refer to these 10 objects as cRM AGNs. In total, our extended sample consists of 44 objects: 30 CARAMEL AGNs, six GRAVITY AGNs, and 10 cRM AGNs.

2.1.1. Black Hole Masses

The black hole masses, $M_{\rm BH}$, for the entire sample are listed in Table 1, with column (2) indicating the technique used for $M_{\rm BH}$ determination. For CARAMEL and GRAVITY AGNs, $M_{\rm BH}$ was determined independently, without assuming the virial factor f, avoiding assumptions about BLR geometry. NGC 3783 and IC 4329A, present in both samples, have $M_{\rm BH}$ values consistent between both techniques. The $M_{\rm BH}$ from CARAMEL is used for the analysis unless stated otherwise. NGC 3227 is the only AGN with $M_{\rm BH}$ measured using a third technique, stellar dynamical modeling, suitable for nearby galaxies where the BH sphere of influence is spatially resolved (R. I. Davies et al. 2006). The value from this method $\log(M_{\rm BH}/M_\odot) = 7.0 \pm 0.3$ agrees with the $\log(M_{\rm BH}/M_\odot) = 7.04 \pm 0.11$ from `CARAMEL` modeling (M. C. Bentz et al. 2023a), with the latter adopted for analysis.

The cRM AGNs require assuming an f factor to determine $M_{\rm BH}$. Previous studies have used different calibrations of $\langle f \rangle$ for deriving $M_{\rm BH}$, e.g., 5.5 (C. A. Onken et al. 2004), 5.2 (J.-H. Woo et al. 2010), 2.8 (A. W. Graham et al. 2011), 5.1 (D. Park et al. 2012), 4.3 (C. J. Grier et al. 2013), or 4.8 (M. Batiste et al. 2017b). For consistency, we standardize the virial product (VP) by computing it from the broad Hβ emission-line time lag, $\tau_{\rm cen}^{\rm rms}$, and the line dispersion $\sigma_{\rm line}^{\rm rms}$ via

$$\mathrm{VP} = c\tau_{\rm cen}^{\rm rms}{\sigma_{\rm line}^{\rm rms}}^2/G. \tag{1}$$

If $\sigma_{\rm line}^{\rm rms}$ is unavailable, we estimate it using the relation with $\sigma_{\rm line}^{\rm mean}$, or, if both are not available, $\mathrm{FWHM}_{\rm line}^{\rm mean}$ (E. Dalla Bontà et al. 2020, their Table 3). We then adopt the virial factor of $\log f = 0.65$ ($f = 4.47$) from J.-H. Woo et al. (2015), consistent with the average of the individual values $\log f_{\rm dyn} = 0.66 \pm 0.07$ determined here (see also L. Villafaña et al. 2023) to derive the BH masses via

$$M_{\rm BH} = f\frac{\langle \Delta v\rangle^2\, R_{\rm BLR}}{G}, \tag{2}$$

where G is the gravitational constant. A summary of $M_{\rm BH}$, Hβ time lags, line widths, and VPs is provided in Table 1.

Table 1
Black Hole Masses

AGN Name (1)	Sample (2)	$\tau_{\rm cen}^{\rm rms}$ (day) (3)	τ Reference (4)	$\sigma_{\rm line}^{\rm rms}$ (km s^{-1}) (5)	v-ind. Reference (6)	VP [log $M_{\odot}$] (7)	$M_{\rm BH}$ [log $M_{\odot}$] (8)	$M_{\rm BH}$ Reference (9)	log $f_{\rm dyn}$ (10)
NGC 3227	CARAMEL	$4.03^{+0.85}_{-0.94}$	B23a	1682 ± 39	B23a	$6.35^{+0.11}_{-0.13}$	$7.04^{+0.11}_{-0.11}$	B23a	$0.72^{+0.15}_{-0.17}$
NGC 6814	CARAMEL	$6.64^{+0.87}_{-0.90}$	B09b	1610 ± 108	B09b	$6.52^{+0.11}_{-0.12}$	$6.42^{+0.24}_{-0.16}$	P14	$-0.14^{+0.26}_{-0.20}$
NGC 4593	CARAMEL	$3.54^{+0.76}_{-0.82}$	W18	1601 ± 40	B15	$6.25^{+0.11}_{-0.13}$	$6.65^{+0.27}_{-0.15}$	W18	$0.41^{+0.29}_{-0.20}$
NGC 3783	CARAMEL	$9.60^{+0.65}_{-0.72}$	B21a	1619 ± 137	B21a	$6.69^{+0.10}_{-0.11}$	$7.45^{+0.07}_{-0.10}$	B21b	$0.82^{+0.12}_{-0.15}$
	GRAVITY	…	…	…	…	…	$7.40^{+0.13}_{-0.14}$	G21	…
NGC 2617	cRM	$6.38^{+0.44}_{-0.50}$	F17	2424 ± 91	F17	$6.86^{+0.06}_{-0.07}$	$7.51^{+0.47}_{-0.47}$	This work	$^{*}0.65$
IC 4329 A	CARAMEL	$16.33^{+2.59}_{-2.28}$	B23b	2112 ± 93	B23b	$7.15^{+0.10}_{-0.11}$	$7.64^{+0.53}_{-0.25}$	B23b	$0.49^{+0.54}_{-0.27}$
	GRAVITY	…	…	…	…	…	$7.15^{+0.38}_{-0.26}$	G24	…
Mrk 1044	cRM	$10.50^{+3.30}_{-2.70}$	D15	$^{\dagger}831 \pm 43$	D15	$6.15^{+0.15}_{-0.19}$	$6.45^{+0.12}_{-0.10}$	This work	$^{*}0.65$
NGC 5548	CARAMEL	$4.17^{+0.36}_{-0.36}$	P17	4115 ± 513	P17	$7.14^{+0.14}_{-0.15}$	$7.64^{+0.21}_{-0.18}$	W20	$0.37^{+0.25}_{-0.24}$
NGC 7469	cRM	$8.00^{+0.80}_{-1.50}$	L21	1485 ± 34	L21	$6.53^{+0.08}_{-0.09}$	$7.18^{+0.05}_{-0.09}$	This work	$^{*}0.65$
Mrk 1310	CARAMEL	$3.66^{+0.59}_{-0.61}$	B09b	755 ± 138	B09b	$5.61^{+0.21}_{-0.25}$	$7.42^{+0.26}_{-0.27}$	P14	$1.63^{+0.34}_{-0.37}$
Mrk 1239	GRAVITY	…	…	…	…	…	$7.47^{+0.15}_{-0.92}$	G24	…
Arp 151	CARAMEL	$3.99^{+0.49}_{-0.68}$	B09b	1252 ± 46	B09b	$6.08^{+0.09}_{-0.10}$	$6.62^{+0.10}_{-0.13}$	P14	$0.51^{+0.14}_{-0.16}$
Mrk 50	CARAMEL	$8.66^{+1.63}_{-1.51}$	W18	2020 ± 103	B15	$6.84^{+0.12}_{-0.13}$	$7.51^{+0.06}_{-0.07}$	W18	$0.72^{+0.13}_{-0.15}$
Mrk 335	CARAMEL	$18.86^{+1.81}_{-2.34}$	G17	1239 ± 78	G17	$6.75^{+0.10}_{-0.11}$	$7.25^{+0.10}_{-0.10}$	G17	$0.59^{+0.14}_{-0.15}$
Mrk 590	cRM	$20.50^{+4.50}_{-3.00}$	P98	…	…	…	$7.58^{+0.07}_{-0.07}$	This work	$^{*}0.65$
SBS 1116+583A	CARAMEL	$2.31^{+0.62}_{-0.49}$	B09b	1528 ± 184	B09b	$6.02^{+0.19}_{-0.23}$	$6.99^{+0.32}_{-0.25}$	P14	$0.96^{+0.37}_{-0.34}$
Zw 229-015	CARAMEL	$3.86^{+0.69}_{-0.90}$	B11	1590 ± 47	B11	$6.28^{+0.11}_{-0.13}$	$6.94^{+0.14}_{-0.14}$	W18	$0.66^{+0.18}_{-0.19}$
Mrk 279	CARAMEL	$16.00^{+5.40}_{-5.80}$	W18	1778 ± 7	B15	$6.99^{+0.13}_{-0.19}$	$7.58^{+0.08}_{-0.08}$	W18	$0.78^{+0.16}_{-0.21}$
Ark 120	CARAMEL	$18.70^{+5.90}_{-4.50}$	U22	1882 ± 42	U22	$7.11^{+0.13}_{-0.16}$	$8.26^{+0.12}_{-0.17}$	V22	$1.15^{+0.17}_{-0.23}$
3C 120	CARAMEL	$25.90^{+2.30}_{-2.30}$	G12	1514 ± 65	G12	$7.06^{+0.07}_{-0.08}$	$7.84^{+0.14}_{-0.19}$	G17	$0.75^{+0.16}_{-0.21}$
MCG +04-22-042	CARAMEL	$13.30^{+2.40}_{-1.80}$	U22	977 ± 29	U22	$6.39^{+0.09}_{-0.10}$	$7.59^{+0.42}_{-0.28}$	V22	$1.06^{+0.43}_{-0.30}$
Mrk 1511	CARAMEL	$5.44^{+0.67}_{-3.00}$	W18	1506 ± 42	B15	$6.38^{+0.15}_{-0.20}$	$7.11^{+0.20}_{-0.17}$	W18	$0.63^{+0.25}_{-0.26}$
PG 1310–108	CARAMEL	$7.20^{+2.41}_{-3.11}$	W18	$^{\dagger}1978 \pm 104$	B15	$6.74^{+0.19}_{-0.26}$	$6.48^{+0.21}_{-0.18}$	W18	$-0.26^{+0.28}_{-0.31}$
Mrk 509	GRAVITY	…	…	…	…	…	$8.00^{+0.06}_{-0.23}$	G24	…
Mrk 110	CARAMEL	$27.80^{+4.30}_{-5.10}$	U22	1314 ± 69	U22	$6.97^{+0.11}_{-0.13}$	$7.17^{+0.67}_{-0.26}$	V22	$0.20^{+0.68}_{-0.29}$
Mrk 1392	CARAMEL	$26.70^{+3.50}_{-3.90}$	U22	1501 ± 38	U22	$7.07^{+0.08}_{-0.09}$	$8.16^{+0.11}_{-0.13}$	V22	$1.01^{+0.13}_{-0.16}$
Mrk 841	CARAMEL	$11.20^{+4.80}_{-3.50}$	U22	2278 ± 96	U22	$7.05^{+0.17}_{-0.24}$	$7.62^{+0.50}_{-0.30}$	V22	$0.60^{+0.53}_{-0.38}$
Zw 535-012	cRM	$20.30^{+8.10}_{-4.60}$	U22	1259 ± 112	U22	$6.80^{+0.19}_{-0.24}$	$7.57^{+0.15}_{-0.10}$	This work	$^{*}0.65$
Mrk 141	CARAMEL	$5.63^{+2.64}_{-2.98}$	W18	$^{\dagger}2473 \pm 125$	B15	$6.83^{+0.22}_{-0.35}$	$7.46^{+0.15}_{-0.21}$	W18	$0.70^{+0.27}_{-0.40}$
RBS 1303	CARAMEL	$18.70^{+3.40}_{-4.30}$	U22	1292 ± 156	U22	$6.78^{+0.18}_{-0.21}$	$6.79^{+0.19}_{-0.11}$	V22	$0.04^{+0.26}_{-0.24}$
Mrk 1048	CARAMEL	$7.40^{+9.70}_{-9.40}$	U22	1726 ± 76	U22	…	$7.79^{+0.44}_{-0.48}$	V22	…
Mrk 142	CARAMEL	$2.74^{+0.73}_{-0.83}$	B09b	859 ± 102	B09b	$5.59^{+0.21}_{-0.26}$	$6.23^{+0.30}_{-0.30}$	L18	$0.74^{+0.36}_{-0.39}$
RX J2044.0+2833	CARAMEL	$14.40^{+1.60}_{-1.90}$	U22	870 ± 50	U22	$6.33^{+0.10}_{-0.11}$	$7.09^{+0.17}_{-0.17}$	V22	$0.66^{+0.20}_{-0.20}$
IRAS 09149–6206	GRAVITY	…	…	…	…	…	$8.00^{+0.30}_{-0.40}$	G20	…
PG 2130+099	CARAMEL	$9.60^{+1.20}_{-1.20}$	G12	1825 ± 65	G12	$6.79^{+0.08}_{-0.09}$	$6.92^{+0.24}_{-0.23}$	G17	$0.00^{+0.25}_{-0.25}$
NPM 1G+27.0587	CARAMEL	$8.00^{+4.70}_{-4.50}$	U22	1735 ± 136	U22	$6.67^{+0.26}_{-0.44}$	$7.64^{+0.40}_{-0.36}$	V22	$0.93^{+0.48}_{-0.57}$
RBS 1917	CARAMEL	$11.90^{+4.30}_{-3.90}$	U22	851 ± 154	U22	$6.22^{+0.27}_{-0.36}$	$7.04^{+0.23}_{-0.35}$	V22	$0.54^{+0.36}_{-0.50}$
PG 2209+184	CARAMEL	$13.70^{+2.80}_{-2.90}$	U22	1353 ± 64	U22	$6.69^{+0.12}_{-0.14}$	$7.53^{+0.19}_{-0.20}$	V22	$0.72^{+0.23}_{-0.25}$
PG 1211+143	cRM	$103.00^{+32.00}_{-44.00}$	K00	$^{\dagger}981 \pm 120$	K00	$7.28^{+0.24}_{-0.31}$	$8.07^{+0.11}_{-0.15}$	This work	$^{*}0.65$
PG 1426+015	cRM	$115.00^{+49.00}_{-68.00}$	K00	$^{\dagger}3345 \pm 471$	K00	$8.40^{+0.29}_{-0.44}$	$9.02^{+0.11}_{-0.15}$	This work	$^{*}0.65$
Mrk 1501	CARAMEL	$15.50^{+2.20}_{-1.80}$	G12	3321 ± 107	G12	$7.52^{+0.08}_{-0.09}$	$7.86^{+0.20}_{-0.17}$	G17	$0.34^{+0.22}_{-0.19}$
PG 1617+175	cRM	$34.30^{+6.80}_{-3.80}$	H21	1288 ± 347	H21	$7.04^{+0.27}_{-0.35}$	$7.69^{+0.21}_{-0.38}$	This work	$^{*}0.65$
PG 0026+129	cRM	$126.80^{+37.50}_{-32.50}$	P04	1719 ± 495	P04	$7.86^{+0.33}_{-0.44}$	$8.50^{+0.07}_{-0.11}$	This work	$^{*}0.65$
3C 273	GRAVITY	$170.00^{+9.60}_{-14.00}$	Z19	1099 ± 40	Z19	$7.60^{+0.06}_{-0.06}$	$9.06^{+0.21}_{-0.27}$	L22	$1.52^{+0.22}_{-0.28}$

Note. AGNs are listed in order of increasing redshift. Column (1): most common identifier. Column (2): sample based on $M_{\rm BH}$ measurement. Column (3): cross-correlation Hβ emission-line lag. Column (4): reference for Hβ lag. Column (5): velocity indicator. Values marked with (†) are estimated from $\sigma_{\rm line}^{\rm mean}$ or FWHM$_{\rm line}^{\rm mean}$. Column (6): reference for velocity indicator. Column (7): virial product (VP) as calculated from Equation (1). Column (8): black hole mass $M_{\rm BH}$. Column (9): reference for $M_{\rm BH}$. "This work" indicates that we have standardized the *f* factor. Column (10): independent *f* factor inferred from dynamical modeling; (*) indicates the sample-average for cRM. Reference keys are as follows: P98: B. M. Peterson et al. (1998); K00: S. Kaspi et al. (2000); P04: B. M. Peterson et al. (2004); B09b: M. C. Bentz et al. (2009b); B11: A. J. Barth et al. (2011); G12: C. J. Grier et al. (2012); P14: A. Pancoast et al. (2014); B15: A. J. Barth et al. (2015); D15: P. Du et al. (2015); F17: M. M. Fausnaugh et al. (2017); G17: C. J. Grier et al. (2017); P17: L. Pei et al. (2017); L18: Y.-R. Li et al. (2018); W18: P. R. Williams et al. (2018); Z19: Z.-X. Zhang et al. (2019); G20: GRAVITY Collaboration et al. (2020); W20: P. R. Williams et al. (2020); B21a: M. C. Bentz et al. (2021a); B21b: M. C. Bentz et al. (2021b); G21: GRAVITY Collaboration et al. (2021); H21: C. Hu et al. (2021); L21: K.-X. Lu et al. (2021); L22: Y.-R. Li et al. (2022); U22: V. U et al. (2022); V22: L. Villafaña et al. (2022); B23a: M. C. Bentz et al. (2023a); B23b: M. C. Bentz et al. (2023b); G24: GRAVITY Collaboration et al. (2024).

2.2. *Quiescent Galaxy Sample*

To compare the AGN scaling relations between $M_{\rm BH}$ and σ to those of quiescent galaxies, we adopt the sample from Kormendy & Ho (2013, hereafter KH13). This sample includes eight local galaxies with $M_{\rm BH}$ measurements based on dynamical modeling of spatially resolved stellar kinematics. Of 86 galaxies in total, we include 44 elliptical galaxies, 20 spiral and S0 galaxies with classical bulges, and 21 spiral and S0 galaxies with pseudobulges. While more recent compilations extend to lower galaxy masses, the definition of host-galaxy parameters in the KH13 sample is closest to our properties used in the following analysis. In particular, the bulge dynamical mass is derived from the spheroid effective radius, allowing for a consistent comparison. We have tested that changing the quiescent sample to those from N. J. McConnell & C.-P. Ma (2013) or R. C. E. van den Bosch (2016) does not qualitatively affect the conclusions.

3. Observations and Data Reduction

3.1. *IFU Observations*

Our team carried out IFU observations for 33/44 of the AGNs in our sample. For the remaining objects, archival IFU observations are available from public repositories. Details of the observations are provided in Table 2. In the following, we describe data acquisition and reduction.

3.1.1. *Keck/KCWI Observations*

Many of the AGNs were initially monitored in the LAMP2011 and LAMP16 RM campaigns to study BLR dynamics and measurements (A. J. Barth et al. 2015; V. U et al. 2022). We followed up with 3D spectroscopy of their host galaxies using the Keck Cosmic Web Imager (KCWI; P. Morrissey et al. 2018) on Keck II under several programs. Key diagnostic features were the stellar absorption lines, in particular the Mg Ib $\lambda\lambda\lambda$5167, 5173, 5184 triplet (hereafter Mg Ib), and the Fe I+Fe II complex. KCWI was configured with the medium IFU slicer and medium-resolution blue grating, providing a $16\farcs5 \times 20\farcs4$ field of view (FOV) and $0\farcs69$ spatial sampling, covering the 4700–5700 Å range optimized for Hβ, [O III], and Mg Ib +Fe lines.

Our observing programs followed the same general strategy: given the rectangular shape of the KCWI FOV, we chose its position angle such that the FOV major axis matched that of the galaxy, as estimated from archival images. For each object, we first took a short exposure (60–120 s, depending on redshift and AGN luminosity), guaranteeing that at least one exposure was available, for which the AGN emission lines in the center were not saturated. We used this exposure to scale up the exposure time of the following frames such that the continuum in the center was close to saturation. For most objects, except nearby bright AGNs, this resulted in 600 s or 990 s science exposures, which we dither-offset by $1''$ along the FOV major axis in between adjacent exposures. In between every other science exposure, we took sky frames by nodding away from the target (T) to obtain external sky exposures (S), e.g., the sequence TSTTSTTST. We chose sky pointings carefully such that they were at least $1'$ away from the AGN, in blank patches of the sky, as verified by Sloan Digital Sky Survey (SDSS), DSS, and Two Micron All Sky Survey (2MASS) images.

The pilot program 2018B_U171 began on 2018 February 8, with observations under photometric conditions and $1\farcs5$–$2''$. We observed during three more nights on 2018 August 7, August 15, and October 3 under program ID 2018B_U012. In total, our observations during 2018B_U171 and 2018B_U012 yielded data of eight AGNs from the LAMP2016 campaign (4200–5400 s on-source times) and for Mrk 50 from the LAMP2011 campaign (900 s on-source). During program 2023B_U114, conducted on four nights between 2023 October and 2024 January, the setup of the BM grating was maintained while using the novel KCWI red arm. We observed 10 AGNs from the LAMP16 campaign under mostly clear conditions, with total integration times from 1800 s to 7200 s. Under program 2024A_U118, we conducted two consecutive runs, observing the last seven objects from the LAMP2016 campaign with total integration times from 1800 s to 7200 s. In addition, we collected some more integration on RXJ 2044.0+2833 and NPM1G +27.0587 to improve the S/N. Although observations since 2023 with the Keck Cosmic Reionization Mapper cover the Ca II $\lambda\lambda\lambda$8498, 8542, and 8662 (hereafter CaT), temporal variation in strong sky emission lines made their accurate subtraction difficult. We tried methods like CubePCA and other approaches based on principle component analysis, like the one from J. S. Gannon et al. (2020), but these were hindered by the absence of empty sky regions in the science exposure or strong spatial variation of the science spectra. As a result, we decided to rely solely on KCWI blue spectra for consistent analysis across the AGN sample.

We reduced the data using the Python KCWI Data Reduction Pipeline, including bias subtraction, flat field correction, and flux calibration. Additionally, we aligned science frames, replaced saturated pixels, and coadded reduced data cubes, as described in our companion paper (R. Remigio et al. 2024, in preparation). The [O I]λ5577 sky emission line indicates an instrumental resolution of FWHM = 0.95Å ($\sim$32 km s^{-1}), with a common wavelength coverage of $\sim$4700–5600 Å and 0.28 Å pix^{-1} sampling.

3.1.2. *Very Large Telescope/MUSE Observations*

We acquired IFU observations for eight of 44 AGNs using the Multi-Unit Spectroscopic Explorer (MUSE) at the Very Large Telescope (VLT). All observations were taken in MUSE wide-field mode, covering a $1' \times 1'$ FOV at $0\farcs2$ sampling, and 4750–9300 Å spectral coverage at a spectral resolution of $R \sim 2500$. Observations were conducted across various programs with consistent strategies. Mrk 1044 and Mrk 1048 had already been observed as part of CARS, while five luminous cRM AGNs were observed under program ID 097.B-0080(A) with integration times between 2800 s and 4500 s, employing standard dither-offset strategies. Observations were conducted in March, April, and July 2016 under gray moon and clear conditions with a seeing of $0\farcs4$–$1\farcs0$. In addition, IRAS 09149–6206 was observed under program ID 113.26SK.001(B), with 260 s exposures split into three observing blocks. Observations on 2024 May 4 and 8, and June 8, achieved a total integration time of 3360 s. For another nine CARAMEL AGNs and two cRM AGNs, we retrieved phase 3 archival data from the ESO archive.

We processed the data using MUSE pipeline v2.8.3-1 with ESO Reflex v2.11.0, following standard reduction procedures including bias frames, continuum lamp frames, arc lamp frames for wavelength calibration, standard star frames for flux calibration, and twilight flats. For AGN host galaxies covering

Table 2
Observational Parameters for the IFU Data

AGN Name (1)	α (J2000) (2)	δ (J2000) (3)	Instrument (4)	UT Date (5)	$t_{\rm exp}$ (s) (6)	$\theta_{\rm FWHM}$ (7)	Prog. ID (8)
NGC 3227	10:23:30.57	+19:51:54.28	VLT/MUSE	2022-03-31	2660	0.96	0108.B-0838(A)
NGC 6814	19:42:40.64	−10:19:24.60	Keck/KCWI	2023-10-17	1650	1.06	2023B_U114
NGC 4593	12:37:04.67	−05:04:10.79	VLT/MUSE	2019-04-28	4750	0.62	099.B-0242(B)
NGC 3783	11:39:01.70	−37:44:19.01	VLT/MUSE	2015-04-19	3600	0.90	095.B-0532(A)
NGC 2617	08:35:38.80	−04:05:18.00	VLT/MUSE	2020-12-23	2300	1.04	0106.B-0996(B)
IC 4329 A	13:49:19.26	−30:18:34.21	VLT/MUSE	2022-04-01	2200	0.81	60.A-9100(A)
Mrk 1044	02:30:05.52	−08:59:53.20	VLT/MUSE	2019-08-24	1200	1.20	094.B-0345(A)
NGC 5548	14:17:59.54	+25:08:12.60	Keck/KCWI	2024-04-29	3305	0.83	2024A_U118
NGC 7469	23:03:15.67	+08:52:25.28	VLT/MUSE	2014-08-19	2400	0.84	60.A-9339(A)
Mrk 1310	12:01:14.36	−03:40:41.10	Keck/KCWI	2024-04-29	3840	1.02	2024A_U118
Mrk 1239	09:52:19.16	−01:36:44.10	VLT/MUSE	2021-01-27	4600	1.14	0106.B-0996(B)
Arp 151	11:25:36.17	+54:22:57.00	Keck/KCWI	2024-01-04	1890	1.22	2023B_U114
Mrk 50	12:20:50.69	+02:57:21.99	Keck/KCWI	2018-02-08	900	1.62	2018B_U171
Mrk 335	00:06:19.52	+20:12:10.50	Keck/KCWI	2023-10-17	2570	0.69	2023B_U114
Mrk 590	02:14:33.56	−00:46:00.18	VLT/MUSE	2017-10-28	9900	0.76	099.B-0294(A)
SBS 1116+583A	11:18:57.69	+58:03:23.70	Keck/KCWI	2024-01-04	2840	1.22	2023B_U114
Zw 229-015	19:03:50.79	+42:23:00.82	Keck/KCWI	2018-08-15	3600	1.01	2018B_U012
Mrk 279	13:53:03.45	+69:18:29.60	Keck/KCWI	2024-04-30	5400	0.84	2024A_U118
Ark 120	05:13:37.87	−00:12:15.11	Keck/KCWI	2018-02-08	4800	1.75	2018B_U171
3C 120	04:33:11.09	+05:21:15.61	Keck/KCWI	2024-01-04	2760	1.12	2023B_U114
MCG +04-22-042	09:23:43.00	+22:54:32.64	Keck/KCWI	2018-02-08	5400	1.87	2018B_U171
Mrk 1511	15:31:18.07	+07:27:27.90	Keck/KCWI	2024-04-29	5910	0.84	2024A_U118
PG 1310–108	13:13:05.79	−11:07:42.40	Keck/KCWI	2024-04-29	5810	1.03	2024A_U118
Mrk 509	20:44:09.75	−10:43:24.70	Keck/KCWI	2024-04-29	4830	1.18	2024A_U118
Mrk 110	09:21:44.37	+52:30:07.63	Keck/KCWI	2018-02-08	5400	2.09	2018B_U171
Mrk 1392	15:05:56.55	+03:42:26.33	Keck/KCWI	2018-02-08	4200	1.71	2018B_U171
Mrk 841	15:01:36.31	+10:37:55.65	Keck/KCWI	2018-02-08	5400	2.01	2018B_U171
Zw 535-012	00:36:20.98	+45:39:54.08	Keck/KCWI	2018-10-03	4500	1.13	2018B_U012
Mrk 141	10:19:12.56	+63:58:02.80	Keck/KCWI	2024-01-04	3770	1.25	2023B_U114
RBS 1303	13:41:12.88	−14:38:40.24	VLT/VIMOS	2009-04-27	2000	1.19	083.B-0801(A)
Mrk 1048	02:34:37.88	−08:47:17.02	VLT/MUSE	2015-01-12	1200	1.21	094.B-0345(A)
Mrk 142	10:25:31.28	+51:40:34.90	Keck/KCWI	2024-04-30	6690	0.76	2024A_U118
RX J2044.0+2833	20:44:04.50	+28:33:12.10	Keck/KCWI	2018-08-07	5400	0.85	2018B_U012
IRAS 09149–6206	09:16:09.36	−62:19:29.56	VLT/MUSE	2024-05-08	1600	1.01	113.26SK.001(B)
PG 2130+099	21:30:01.18	+09:55:00.84	VLT/MUSE	2019-06-09	2440	0.53	0103.B-0496(B)
NPM 1G+27.0587	18:53:03.87	+27:50:27.70	Keck/KCWI	2023-10-20	6000	0.96	2023B_U114
RBS 1917	22:56:36.50	+05:25:17.20	Keck/KCWI	2023-10-17	5550	0.83	2023B_U114
PG 2209+184	22:11:53.89	+18:41:49.90	Keck/KCWI	2023-10-20	6960	0.78	2023B_U114
PG 1211+143	12:14:17.67	+14:03:13.18	VLT/MUSE	2016-04-01	2800	0.66	097.B-0080(A)
PG 1426+015	14:29:06.57	+01:17:06.15	VLT/MUSE	2016-04-04	2800	0.45	097.B-0080(A)
Mrk 1501	00:10:31.01	+10:58:29.00	Keck/KCWI	2023-11-03	4050	0.82	2023B_U114
PG 1617+175	16:20:11.27	+17:24:27.51	VLT/MUSE	2016-04-04	2800	0.52	097.B-0080(A)
PG 0026+129	00:29:13.70	+13:16:03.94	VLT/MUSE	2016-07-31	2250	0.62	097.B-0080(A)
3C 273	12:29:06.69	+02:03:08.59	VLT/MUSE	2016-03-31	4750	0.47	097.B-0080(A)

Note. AGNs are listed in order of increasing redshift (as in Table 1). Column (1): AGN name. Column (2): right ascension. Column (3): decl. Column (4): IFU instrument used to conduct the observations. Column (5): observing date. Column (6): total of on-source exposure time combined for the final cube after rejecting low-quality individual exposures. Column (7): seeing in the final combined cubes inferred from 2D Moffat modeling of the broad Hβ intensity maps. Column (8): program ID of the data set under which the program was executed. Our team carried out observations with the Very Large Telescope (VLT)/MUSE and Keck/KCWI under the program IDs 097.B-0080(A) and U114, U118, and U171, respectively. For approximately a quarter of the sample, we collected archival data.

only a small part of the FOV, we created a mean sky spectrum from the lowest 20% flux in white light images and subtracted it from the cube. When the host galaxy filled the FOV, we used dedicated sky exposures from the archive. Telluric absorption bands were corrected by dividing the spectra by normalized transmission from standard star exposures taken close in time. Residuals in spectra arose from skyline subtraction issues due to the timing of standard stars and spatial variations in the line-spread function. To address these, we used `CubePCA`. This tool identifies the principal components (PCs) in the skyline residuals by fitting orthogonal eigenspectra to the individual spectra, and then subtracts the PCs.

3.1.3. VLT/VIMOS Observations

Three of the 30 CARAMEL AGNs (RBS 1303, PG 1310–108, and NGC 5548) were observed with the VIsible Multi-Object Spectrograph IFU (VIMOS; O. Le Fèvre et al. 2003). The

VIMOS blue and orange cubes cover wavelengths of 3700–5222 Å and 5250-7400 Å, respectively, with a 27″ × 27″ FOV and 0.″6 pixel sampling. While PG 1310–108 and NGC 5548 have higher-resolution, deeper data from Keck/KCWI, RBS 1303 was only observed with VIMOS. We used reduced data cubes from CARS Data Release 1 (B. Husemann et al. 2022), which were initially processed with the `Py3D` package and included standard reduction steps. For specific details on data reduction, including exposure alignment and drizzling, see B. Husemann et al. (2022). Our analysis focuses on the blue cubes, as they cover the essential Mg Ib and Fe I absorption lines for measuring stellar kinematics.

3.1.4. AGN Host-galaxy Deblending

The AGN featureless continuum and broad emission lines (in the wavelength range covering Hβ, He I, and Fe II) can easily outshine the underlying host-galaxy spectrum. It is therefore essential to subtract the unresolved AGN emission before analyzing the faint host-galaxy emission. For this task, we use the approach outlined by B. Husemann et al. (2022): (1) we first estimate the empirical point-spread function (PSF) at and from the broad wavelengths available in each data set using `QDeblend`^{3D} (B. Husemann et al. 2013, 2014). (2) We model the PSFs with a 2D Moffat profile to suppress noise at large distances from the center. (3) If multiple broad lines are available, we interpolate the PSF as a function of wavelength. (4) We reconstruct the intrinsic host-galaxy surface brightness profile from 2D image modeling. (5) Finally, we iteratively subtract the point-like AGN emission from the extended host-galaxy emission, combining the wavelength-dependent PSF with the host-galaxy surface brightness profile. For a more detailed description of the method and an illustration of the deblending, we refer to B. Husemann et al. (2022) and N. Winkel et al. (2022).

Deblending is crucial for accurately extracting host-galaxy stellar kinematics, as shown in Appendix B. Without deblending, the stellar velocity dispersion σ can be overestimated by up to a factor of 2, particularly near the AGN, which severely biases the luminosity-weighted mean σ due to poorly fitted spaxels. An alternative is to fit the AGN spectrum simultaneously with the host-galaxy emission, as used for a subset of the LAMP AGNs by R. Remigio et al. (2024, in preparation). This method, compared in Appendix H, generally provides results consistent with our deblending approach within the nominal uncertainties.

3.2. HST Imaging

Considering the large range of AGN parameters in our sample, the host galaxies are also likely to cover a large range in stellar masses, sizes, and morphologies. To enable a consistent calibration of the scaling relations, we need a consistent measurement of the host-galaxy kinematics. This can be achieved by measuring the kinematics of different host-galaxy morphological components and separating their contributions to the galaxy-integrated kinematics. We characterize the host-galaxy morphologies from high-resolution images obtained with HST. For 33/44 of the AGNs in the sample, archival wide-field imaging data exist, which were acquired with either WFC3/UVIS, Advanced Camera for Surveys (ACS)/High-Resolution Channel (HRC), or WFPC2/Planetary Camera 1 in optical broad or medium bands. The program HST-GO 17103 (PI: Bennert) acquired broadband imaging from WFC3/UVIS for the remaining 11 objects of the CARAMEL AGN sample. A detailed description of the data acquisition, data reduction, PSF subtraction, host-galaxy decomposition, 2D surface photometry, and derived host-galaxy parameters will be presented in our companion paper (V. N. Bennert et al. 2024, in preparation).

3.2.1. Special Handling of Individual Objects

The host-galaxy decomposition based on HST/WFC3 images did not yield stable solutions for three objects at the very low and high-redshift ends. For the nearby galaxy NGC 3227, the WFC3 FOV covers only a small fraction of its 5.′4 × 3.′6 size. For NGC 3227's galaxy effective radius, we adopt the scale radius from an exponential fit to the SDSS photometry in the *r* band (*exprad_r*). Although this approach assumes that the PSF has a minimal impact on NGC 3227's light profile, it provides a quantity closest to the $R_{\mathrm{eff}}^{\mathrm{gal}}$ definition used for the other objects. We encountered the same challenge for IC 4329A, where the highly inclined galaxy extends beyond the HST ACS/HRC FOV. While structural decomposition allows fitting the bulge, we adopt the galaxy-scale length of 25.″2 from the NASA/IPAC Extragalactic Database (NED), which was fitted to the *k*-band photometry from 2MASS.

For PG 0026+129, an extremely bright quasar, the host-galaxy parameters recovered in Section 4.1 did not converge to stable solutions. Therefore, we adopted the host-galaxy effective radius $R_{\mathrm{eff}}^{\mathrm{gal}} = 2.''6$ from K. K. McLeod & B. A. McLeod (2001), which was estimated based on HST/NIC2 F160W imaging. We encountered the same issue with the HST/WFC3 image of the bright quasar 3C 273. We adopt an effective radius of 2.″3 for the host galaxy, as reported by J. N. Bahcall et al. (1997). Their measurement is based on HST/WFPC F606W imaging and is consistent with the 2.″3–2.″6 range reported by A. R. Martel et al. (2003), measured from coronagraphic imaging with HST/ACS in the *V* and *I* bands, respectively.

4. Analysis

4.1. Surface Photometry

For the purpose of this work, we are exclusively interested in the stellar kinematics of different host-galaxy components for which we adopt effective radii derived by fitting the 2D surface brightness profiles. For this task, we used the public code `lenstronomy` (S. Birrer & A. Amara 2018), as outlined by V. N. Bennert et al. (2021). We measure the host-galaxy effective radius, $R_{\mathrm{eff}}^{\mathrm{gal}}$, from the PSF-subtracted host-galaxy surface profile. We used a universal parameterization of a single spheroidal component (s), i.e., using a single Sérsic component as the input for `lenstronomy`, as is often done for marginally resolved high-redshift galaxies or massive elliptical galaxies. In reality, however, only a minority of galaxies in our sample are well described by a spheroidal model. The majority of our AGN hosts are late-type galaxies, with a large morphological diversity, including bars, bulges, and disks, which can be seen in the reconstructed continuum images in Figure 1. The HST imaging allows us to decompose the host galaxy into its morphological components. For many nearby AGNs, morphological classifications are available in the literature. Based on the high-quality imaging data collected for this project (V. N. Bennert et al. 2024, in preparation), we

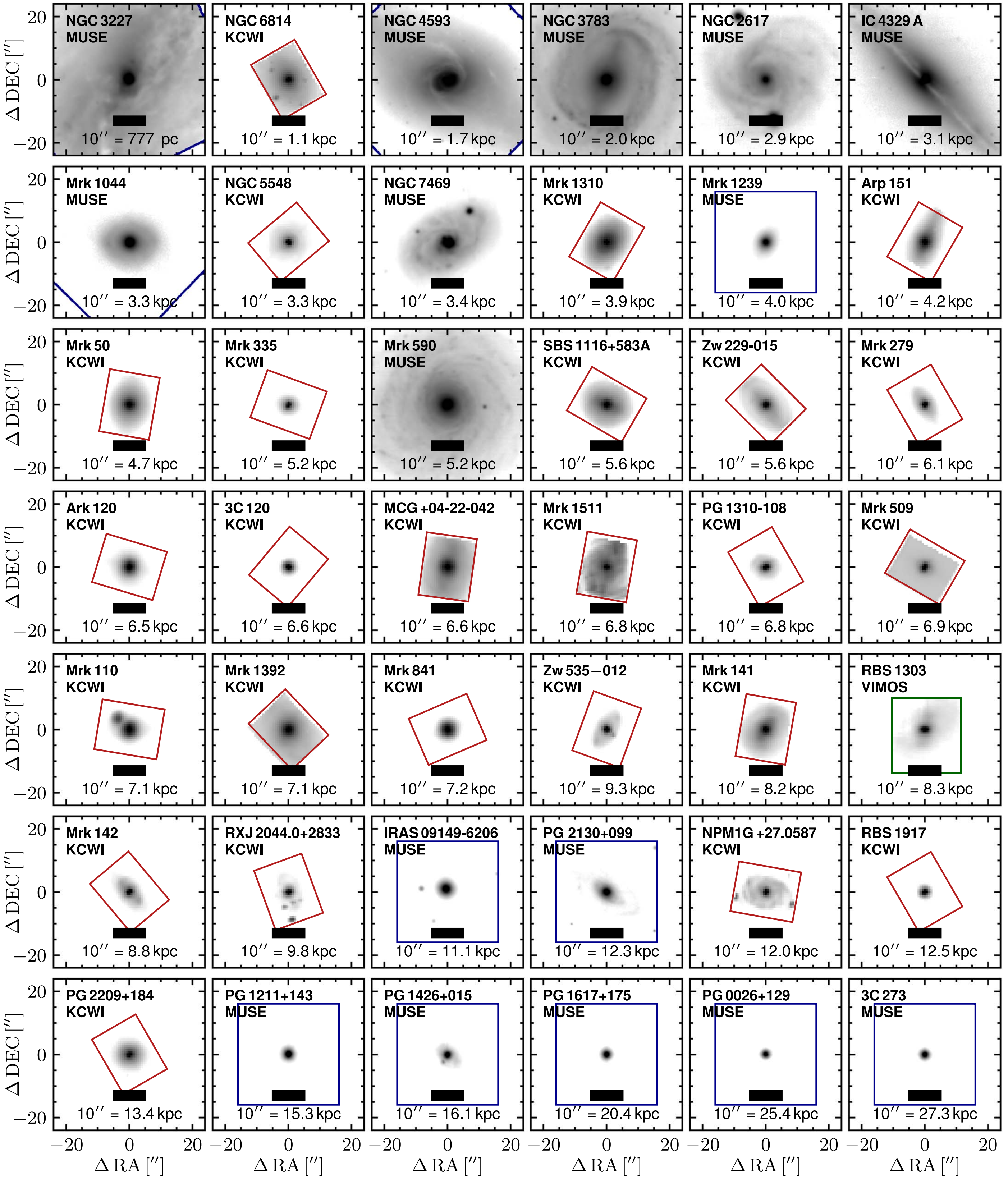

Figure 1. Gallery of *V*-band images. Images were reconstructed from the IFU data cubes (Table 2) with frames centered on the AGN position. North is up and east is to the left. Rectangles indicate the FOV covered by the IFU instrument: VLT/MUSE (blue), Keck/KCWI (red), and VLT/VIMOS (green). For more distant AGNs observed with MUSE, cutouts are shown. AGN luminosity, host-galaxy sizes, IFU field coverage, and depth of the observations vary substantially between the data sets.

Table 3
Host-galaxy Parameters

AGN Name (1)	Alt. Name (2)	z (3)	Scale (kpc per arsec) (4)	Morph. (5)	Morph. Reference (6)	Model (7)	$R_{\rm eff}^{\rm gal}$ (arsec) (8)	$R_{\rm eff}^{\rm bulge}$ (arsec) (9)	i (deg) (10)	Comment (11)
NGC 3227	…	0.004	0.08	SAc	This work	sd	28.6	1.7	65	
NGC 6814	…	0.005	0.11	SABc	S11	sdb	45.1	1.3	22	
NGC 4593	Mrk 1330	0.008	0.17	SABb	S11	sdb	16.9	6.2	46	
NGC 3783	…	0.010	0.20	SABb	V91	sdb	14.0	2.2	33	
NGC 2617	LEDA 24141	0.014	0.29	SAa	This work	sd	12.1	1.2	18	
IC 4329 A	RBS 1319	0.015	0.31	SA	V91	sd	^35.2	2.9	20	
Mrk 1044	HE 0227-0913	0.016	0.33	SABc	This work	sdb	6.0	0.8	28	
NGC 5548	Mrk 1509	0.016	0.33	SAa	This work	sd	11.3	8.4	28	Asym. morph.
NGC 7469	Mrk 1514	0.017	0.34	SABc	This work	sd	9.3	8.3	65	
Mrk 1310	RBS 1058	0.019	0.39	SAc	B19	sd	4.1	4.2	43	
Mrk 1239	LEDA 28438	0.020	0.40	S0A	This work	s	3.2	3.2	41	
Arp 151	Mrk 40	0.021	0.42	S0	S11	s	3.2	3.2	67	Interacting
Mrk 50	RBS 1105	0.023	0.47	S0A	N10	s	4.0	4.0	39	
Mrk 335	PG 0003+199	0.026	0.52	E	K21	s	2.6	2.6	24	
Mrk 590	NGC 863	0.026	0.52	SAa	S11	sdb	2.0	1.4	35	
SBS 1116+583A	Zw 291-51	0.028	0.56	SABa	This work	sdb	4.1	0.6	28	
Zw 229-015	…	0.028	0.56	SBd	K21	sdb	7.3	0.8	49	
Mrk 279	…	0.030	0.61	SAa	This work	sd	4.2	2.3	50	Companion
Ark 120	Mrk 1095	0.033	0.65	SAa	This work	sd	5.7	2.0	30	Asym. morph.
3C 120	Mrk 1506	0.033	0.66	S0A	S11	s	2.7	2.7	39	Tidal tails
MCG +04-22-042	Zw 121-75	0.033	0.66	SABb	This work	sdb	11.7	0.9	56	
Mrk 1511	NGC 5940	0.034	0.68	SABc	B19	sd	11.6	0.5	40	
PG 1310–108	HE 1310-1051	0.034	0.68	SABa	This work	sdb	3.2	0.4	24	Tidal tails
Mrk 509	…	0.035	0.69	*E2	B09a	s	2.4	2.4	39	
Mrk 110	PG 0921+525	0.035	0.71	*S0	This work	s	1.5	1.5	…	
Mrk 1392	Zw 48-115	0.036	0.71	SBb	This work	sdb	10.4	0.7	59	
Mrk 841	PG 1501+106	0.036	0.72	E	This work	s	3.6	3.6	18	
Zw 535-012	LEDA 2172	0.048	0.93	SBb	This work	sdb	5.7	0.6	58	
Mrk 141	Zw 313-11	0.042	0.82	SABa	B19	sdb	5.6	0.4	40	Companion
RBS 1303	HE 1338-1423	0.042	0.83	SBa	This work	sdb	7.1	0.9	53	
Mrk 1048	NGC 985	0.043	0.84	SBc	S02	sd	11.9	2.7	46	Interacting
Mrk 142	PG 1022+519	0.045	0.88	SBa	This work	sdb	5.6	0.4	34	
RX J2044.0+2833	…	0.050	0.98	SBd	K21	sdb	4.2	0.2	46	
IRAS 09149–6206	…	0.057	1.11	S0	This work	s	5.2	5.2	49	
PG 2130+099	Mrk 1513	0.064	1.23	Sa	B09a	sd	2.5	0.3	52	
NPM 1G+27.0587	…	0.062	1.20	SAb	This work	sd	6.5	0.6	38	Companion
RBS 1917	…	0.065	1.25	SB	This work	sdb	1.7	0.1	23	
PG 2209+184	…	0.070	1.34	S	This work	sd	2.9	2.9	30	
PG 1211+143	…	0.081	1.53	E2	B09a	s	0.2	0.2	…	
PG 1426+015	Mrk 1383	0.086	1.61	E2	B09a	s	2.0	2.0	…	
Mrk 1501	PG 0007+107	0.087	1.63	*S0	S11	s	5.3	5.3	52	Companion
PG 1617+175	Mrk 877	0.112	2.04	E2	B09a	s	1.2	1.2	…	
PG 0026+129	RBS 68	0.145	2.54	E1	B09a	s	*2.3	*2.3	…	
3C 273	PG 1226+023	0.158	2.73	E3	B09a	s	†2.3	†2.3	…	

Note. AGNs are listed in order of increasing redshift (as in Table 1). Column (1): most common identifier. Column (2): alternative identifier. Column (3): source redshift from NED. Column (4): physical scale of 1″. Column (5): host-galaxy morphological classification, simplified to the de Vaucouleurs system. Values marked with (*) are uncertain due to strong AGN blending. Column (6): reference key for morphological classification. Column (7): adopted parameterization for the host-galaxy morphology (s = Sérsic only, sd = Sérsic + disk ($n = 1$) fit; sdb = Sérsic + disk ($n = 1$) + bar ($n = 0.5$) fit; a detailed presentation will be outlined in V. N. Bennert et al. 2024, in preparation). Column (8): galaxy effective radius from fitting a single Sérsic component. Column (9): bulge effective radius. Column (10): inclination based on the disk axis ratio a/b, which is retrieved from the best-fit `lenstronomy` model. Column (11): additional note regarding host morphology. (^) Adopted from NED. (*) Adopted from K. K. McLeod & B. A. McLeod (2001). (†) Adopted from J. N. Bahcall et al. (1997). Reference keys are as follows: V91: G. de Vaucouleurs et al. (1991); S02: M. Salvato (2002); J04: K. Jahnke et al. (2004); N10: P. B. Nair & R. G. Abraham (2010); B09a: M. C. Bentz et al. (2009a); S11: L. Slavcheva-Mihova & B. Mihov (2011); A15: H. B. Ann et al. (2015); B19: R. J. Buta (2019); K21: M. Kim et al. (2021).

complemented (or revised) literature classifications, and standardized the nomenclature to the de Vaucouleurs system (see column (5) of Table 3). We use this prior information for parameterizing the host model, listed in Table 3. Models include bulge-only (s), bulge+disk (sd), or bulge+disk+bar (sdb) components. The best-fit effective radii of the entire galaxy and bulge only, $R_{\rm eff}^{\rm gal}$ and $R_{\rm eff}^{\rm bulge}$, serve as a standardized measure across which stellar kinematics are extracted. After running a minimum of 10 decompositions for each object using different starting parameters, we estimate 0.1 dex systematic uncertainty for effective radii, and 0.2 dex if strong residuals from the PSF subtraction are present on scales of the spheroid.

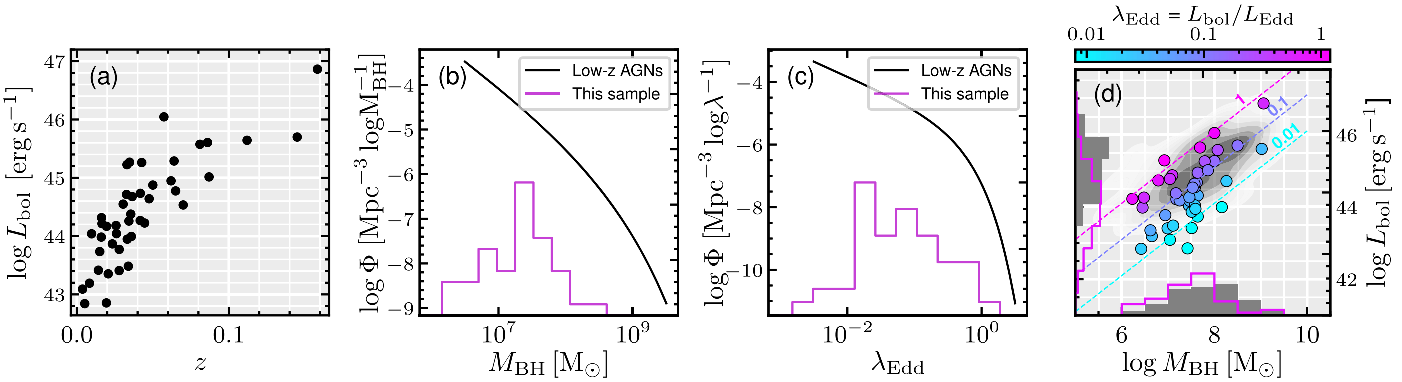

Figure 2. Properties of our AGN sample. From left to right, the panels show the AGN sample in (a) AGN bolometric luminosity as a function of galaxy redshift, (b) distribution of BH masses (purple) compared to BH mass function (BHMF) obtained from the local AGN population in the Hamburg/ESO (HES) survey, and (c) Eddington ratio distribution compared with the global Eddington ratio distribution function (ERDF) from HES. Panels (b) and (c) show that our sample's distribution in $M_{\rm BH}$ (and $\lambda_{\rm Edd}$) is mostly shaped by the luminosity bias at the low-$M_{\rm BH}$ end, and the cutoff of the BHMF (ERDF) at the massive end, respectively. Panel (d) shows that our AGNs sample has a similar range in $M_{\rm BH}$ and luminosity compared to HES, characteristic of a flux-limited sample.

More details on the HST imaging data, the fitting process, and the full set of parameters will be presented in our companion paper (V. N. Bennert et al. 2024, in preparation).

4.1.1. Disk Axis Ratio as Proxy for Inclination

The inclination of a galaxy disk can be estimated from its axis ratio as $i_{b/a} = \arccos(b/a)$. However, structural decomposition carried out with `lenstronomy` is sensitive to the parameterization defined by the user. While we are careful to check the parameterization, systematic uncertainties from limited FOV, prominent dust lanes crossing the galaxy center, and PSF mismatches likely contribute systematic uncertainties to the structural decomposition (V. N. Bennert et al. 2024, in preparation; see also Section 5.1). To test whether the disk axis ratio is a good proxy for the galaxy inclination, we compare $i_{b/a}$ with a visual estimate of the galaxy inclination $i_{\rm vis}$. In general, it is possible to estimate the inclination if the host galaxy can be robustly separated from the PSF, and a disk component is clearly visible. For the majority of the sample, we based our estimate on the original HST images. However, for NGC 3227 and NGC 4593, the WFC3 FOV covers only a fraction of the galaxy, so that we used the PanSTARRS i-band images. We were able to estimate $i_{\rm vis}$ for each of the 29 disk galaxies, which are preferentially located at a lower redshift and show a prominent disk component. Depending on how well the galaxy is resolved and how dominant the PSF is, we estimate that the associated uncertainties of $i_{\rm vis}$ range from approximately 10° to 20°. Overall, the visual estimates agree with the `lenstronomy` measurements within these uncertainties. We conclude that $i_{b/a}$, derived from the disk axis ratio, is a suitable indicator for the galaxy inclination. In the following, we adopt $i_{b/a}$ as a proxy for the galaxy inclination, and refer to it as i, as listed in Table 3. As a side note, the consistent inclination values provide further evidence that the `lenstronomy` fits have resulted in realistic physical parameters of the host galaxy.

4.2. AGN Parameters

The AGNs in our sample were exclusively selected based on their spectral properties, more precisely the ability to temporally resolve the broad emission-line lags. Considering that only a fraction of AGNs show the required variability to monitor them in RM campaigns, we are interested in quantifying to what extent our sample is representative of the overall AGN population. Important properties that can be easily compared are the AGN bolometric luminosity $L_{\rm bol}$, the BH mass $M_{\rm BH}$, and the Eddington ratio $\lambda_{\rm Edd}$. They can be directly estimated from the unobscured AGN spectra available in the host-subtracted IFU data.

We constrain the AGN spectral modeling to the Hβ–[O III] wavelength range, for which various studies have provided calibrations (e.g., S. Kaspi et al. 2000; B. M. Peterson et al. 2004; J. E. Greene & L. C. Ho 2005a; M. Vestergaard & B. M. Peterson 2006; M. C. Bentz et al. 2013; J.-H. Woo et al. 2015). A detailed description of our fitting methodology is given in Appendix A. We estimated the bolometric luminosity from the 5100 Å continuum luminosity using a bolometric correction factor: $L_{\rm bol} = 10 \times L_{5100}$ (G. T. Richards et al. 2006). The Eddington ratio is $\lambda_{\rm Edd} = L_{\rm bol}/L_{\rm Edd}$, where $L_{\rm Edd}/{\rm erg\ s}^{-1} = 1.26 \times 10^{38} M_{\rm BH}/M_\odot$ with $M_{\rm BH}$ taken from Table 1. The AGN parameters are shown in Figure 2, where we compare our sample with the properties of the overall local AGN population in the flux-limited Hamburg ESO survey (L. Wisotzki et al. 2000; A. Schulze & L. Wisotzki 2010). The unimodal distribution of our AGNs in $M_{\rm BH}$ (and $\lambda_{\rm Edd}$ analogously) can be explained by the primary sample selection criteria. At low $M_{\rm BH}$, the distribution is incomplete due to the low S/N of the AGN spectral features, whereas at high $M_{\rm BH}$, the number of AGNs decreases due the cutoff of the SMBH mass function. The selection effects are discussed in more detail in Section 5.4.

4.3. Spectral Synthesis Modeling

To determine the host-galaxy stellar kinematics, we used the first and second moments of the line-of-sight velocity distribution (LOSVD) obtained by fitting the stellar continuum after subtracting AGN emission (see Section 3.1.4). However, data from Keck/KCWI, VLT/MUSE, and VLT/VIMOS vary in wavelength coverage, field coverage, and resolution. Additionally, the depth of observations and the brightness of the central AGN limit the mapping of stellar kinematics. To ensure a consistent analysis across data sets, we developed a common methodology.

The extraction of stellar kinematics involves several interconnected steps, each affecting the kinematic parameters.

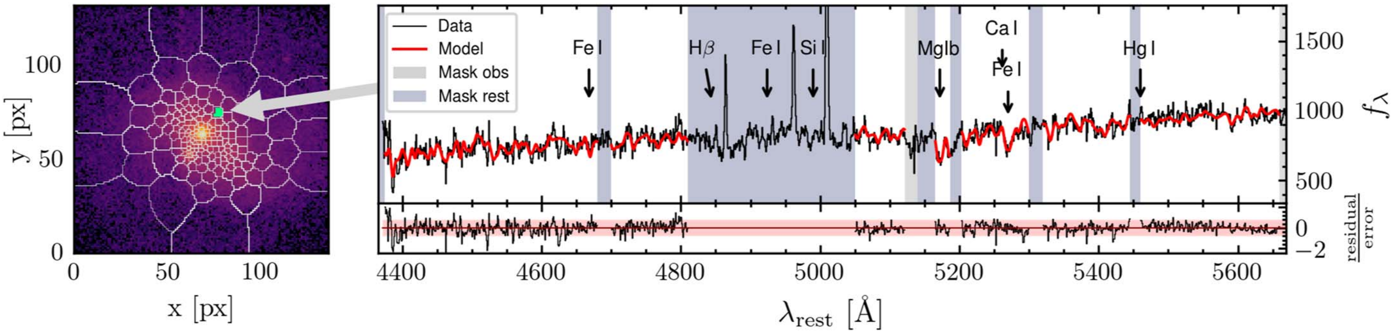

Figure 3. Spatially resolved spectral synthesis modeling, demonstrated for PG 1426+015. The left panel shows a continuum image from integrating the wavelength range 5100–5200 Å of the AGN-subtracted MUSE data cube. The overlaid grid depicts the Voronoi cells, within which spectra are coadded to achieve a minimum S/N of 20. The example spectrum from the arbitrary cell (highlighted green) is shown as a black line in the upper-right panel. We constrain the spectral fitting to regions in the rest frame that are free from contamination from broad emission lines and residuals from narrow emission lines (blue stripes). In the observed frame, we mask skyline residuals (gray stripes). The best-fit stellar continuum model (red line) closely reproduces the continuum emission within the 1σ error, as illustrated by the normalized residuals shown in the bottom-right panel.

We tested various approaches to optimize results and maintain general applicability, with details provided in Appendix H.

1. We tested stellar kinematics extraction with `pPXF` (M. Cappellari & E. Emsellem 2004; M. Cappellari 2017), `PyParadise` (B. Husemann et al. 2016a), and `BADASS` (R. O. Sexton et al. 2021), all yielding consistent results despite differing methodologies. A detailed comparison is in Appendix H.
2. We tested fitting different wavelength regions ([4750–5300 Å], [5150–5200 Å], [8450–8650 Å]), each containing key diagnostic features for stellar kinematics. A comparison is detailed in Appendix E.
3. We tested the robustness of our results using various stellar and simple stellar population (SSP) template libraries: the 2009 Galaxy Spectral Evolution Library (G. Bruzual & S. Charlot 2003), the high-resolution SSP library from ELODIE (M11; C. Maraston & G. Stromback 2011), the X-shooter Spectral Library (XSL; K. Verro et al. 2022), and the Indo-U.S. Library of Coudé Feed Stellar Spectra (F. Valdes et al. 2004). A comparison of the impact on stellar kinematics is detailed in Appendix G.
4. For AGNs observed with multiple IFU instruments (e.g., VLT/MUSE plus Keck/KCWI or VLT/VIMOS), we verified the consistency of our method by analyzing them with the same procedures. Details are provided in Appendix D.

After evaluating the options detailed in the appendices, we summarize our findings:

(1) *Template comparison*. `PyParadise` is superior with large wavelength coverage, e.g., for MUSE spectra, while `pPXF` offers more robust stellar kinematics extraction for smaller wavelength ranges.

(2) *Wavelength range*. A larger wavelength range provides more diagnostic features and better kinematic constraints. However, CaT cleaned from skyline contamination is covered for objects observed with MUSE. We adopted the 4750–5200 Å range, which is covered by all data sets and contains key absorption features.

(3) *Template tesolution*. Higher spectral resolution reduces statistical uncertainties. Among higher-resolution templates, XSL and M11 yield consistent results, but XSL's greater number of spectra (130 versus 10) offers more robust absorption line reproduction and better kinematic fits.

(4) *Instrumental comparison*. For objects observed with multiple instruments, deep MUSE observations generally provide the highest S/N stellar continuum and superior spatial resolution and field coverage compared to Keck/KCWI and VLT/VIMOS. Thus, we prefer VLT/MUSE data for our analysis when available.

For all objects, we adopt the following universal strategy: after subtracting the point-like AGN emission, as described in Section 3.1.4, we increase the S/N of the host-galaxy emission either by taking aperture-integrated spectra (see Section 4.4.1), or by binning the cube using Voronoi tessellation to a spectral S/N of 20 in the rest-frame wavelength range 5100–5200 Å. Next, we fit the stellar continuum emission in the 4750–5200 Å range using the `pPXF` code (M. Cappellari & E. Emsellem 2004; M. Cappellari 2017), typically with fifth-order polynomials to account for nonphysical continuum variations from 3D-PSF subtraction. We mask the Na I $\lambda\lambda$ 5890 and 5896 skylines, as well as Hγ, Hβ, [O III][O III]$\lambda\lambda$ 4960, and 5007 emission lines (hereafter [O III]), and the [O I]λ5577 night skyline. An example spectrum from a MUSE data cube is shown in Figure 3, along with the best-fit stellar continuum model and residuals.

4.4. Host-galaxy Stellar Kinematics

Most previous studies investigating the $M_{\rm BH}$–$\sigma_\star$ relation have used aperture-integrated spectra to measure the AGN host-galaxy properties for large data sets (e.g., T. Treu et al. 2004; A. W. Graham et al. 2011; C. J. Grier et al. 2013; J.-H. Woo et al. 2015; T. Caglar et al. 2020, 2023, and many more). The statistical power for calibrating scaling relations comes at the cost of larger uncertainties, for example, due to the unknown fraction of the host galaxy covered by the fibers. Long-slit spectroscopy in combination with high-resolution imaging has enabled resolving the host-galaxy kinematics along their photometric major axis (V. N. Bennert et al. 2015). Thanks to IFU observations, we can now spatially resolve the host-galaxy kinematics in two dimensions and differentiate them for different host-galaxy morphological components.

To determine if the kinematics are resolved, we required at least five Voronoi cells with constrained kinematics and centroids within the galaxy's effective radius. The IFU observations are deep enough to spatially map the host-galaxy stellar kinematics for 34/44 AGNs. As illustrated in Figure 4, sub-kpc kinematic structures can be resolved in nearby

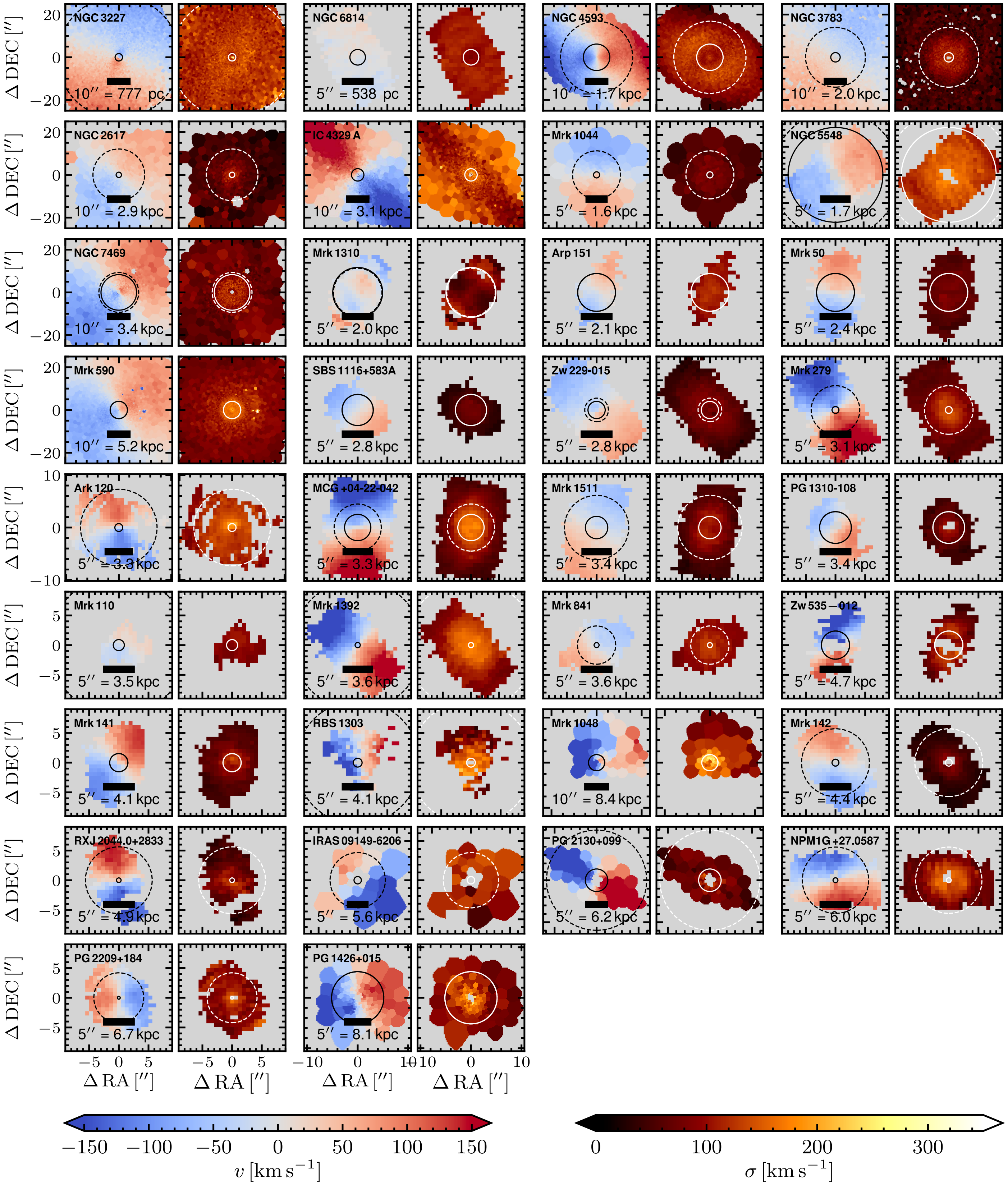

Figure 4. Spatially resolved stellar-kinematic maps of the AGN host galaxies. We show the first moment (line-of-sight velocity v) and second moment (dispersion σ), measured from 2D continuum modeling of the AGN-subtracted data cubes (see Section 4.3). Two neighboring panels belong to the same objects, and the velocity and dispersion color maps share a common scaling, which is indicated by the color bars at the bottom. Black (left panels) or white (right panels) circles indicate $R_{\rm eff}^{\rm bulge}$ (continuous line) and $R_{\rm eff}^{\rm gal}$ (dashed line), as described in Section 4.1. The AGN host galaxies show a large diversity in their kinematic structures. In some cases, either the kinematics in $R_{\rm eff}^{\rm bulge}$ cannot be resolved, or $R_{\rm eff}^{\rm gal}$ is larger than the FOV covered by the IFU.

systems. Examples are nuclear disks in NGC 3227 and NGC 2617, or the counterrotating disk in Mrk 1310. Such features are commonly identified from photometric decomposition of barred galaxies (S. Comeron et al. 2010; D. A. Gadotti et al. 2020) and have been referred to as "pseudobulges" (J. Kormendy & R.C. Kennicutt 2004). Due to lower spatial resolution, kinematic substructures remain unresolved in more distant galaxies. In addition, by selection, those distant galaxies tend to host more luminous AGNs. Their blending emission can hamper an accurate mapping of the host-galaxy stellar kinematics so that, for 12/44 galaxies, the galaxy kinematics cannot be spatially mapped. AGNs for which this is the case are typically high specific-accretion-rate AGNs like Mrk 335, Mrk 1239 3C 120, or the PG quasars contained in our sample. Furthermore, we note that accessing the kinematics within $R_{\rm eff}^{\rm bulge}$ and $R_{\rm eff}^{\rm gal}$ can be limited by spatial resolution close to the AGN or the size of the FOV, respectively. Given these limitations, establishing a consistent method for extracting σ is essential. This consistency will enable us to fully leverage the strength of this AGN sample, covering a broad range of $M_{\rm BH}$, $L_{\rm bol}$, z, and host morphologies.

4.4.1. Two Methods For Measuring σ

There is no standard definition for measuring the stellar velocity dispersion σ from the spatially resolved first and second moments of the LOSVD. As a result, it is unclear over what fraction of $R_{\rm eff}^{\rm gal}$ the kinematics should be averaged or how this averaging should be performed. The literature presents two different approaches for measuring stellar velocity dispersion. For measuring the kinematics within the bulge effective radius of quiescent galaxies, several studies have favored including rotational broadening by explicitly combining the first and second velocity moments through Equation (C1); KH13 refer to this technique as Nuker team practice (see, e.g., J. Pinkney et al. 2003; K. Gültekin et al. 2009; M. Cappellari et al. 2013; R. C. E. van den Bosch 2016; and for AGNs also see V. N. Bennert et al. 2015, 2021). This approach is motivated by the equipartition of energy in the dynamically relaxed bulge, where the combination of $v_{\rm spat}$ and $\sigma_{\rm spat}$ accurately traces the gravitational potential imposed by the stellar mass. However, the bulge component is often barely resolved in AGN host galaxies, resulting in substantial contributions from disk rotation to dispersion being measured from aperture-integrated spectra. When removing rotational broadening through spatially resolving the LOSVD, M. Batiste et al. (2017b) reported that σ decreases by 13 km s^{-1} on average. They underscore that the difference is strongest for inclined spiral galaxies with a significant substructure, highlighting the necessity of maintaining a consistent definition. We briefly review the details of both methods for measuring σ specific to our sample.

4.4.2. Spatially Resolved Kinematics

For the first method, we average the spatially resolved velocity dispersion σ within a chosen aperture. In the following, we refer to this quantity as the *spatially resolved* stellar velocity dispersion, $\sigma_{\rm spat}$. We note that this quantity is different from the definition used by V. N. Bennert et al. (2015), who reconstructed the aperture-integrated dispersion from the spatially resolved first and second velocity moment. We have defined a similar quantity $\sigma_{\rm spat}^{\rm recon}$ and explain its behavior relative to $\sigma_{\rm ap}$ in more detail in Appendix C. In short, the definition from V. N. Bennert et al. (2015) explicitly includes rotational broadening, whereas our $\sigma_{\rm spat}$ implicitly removes rotational broadening from kinematic structures down to the spatial scales that are resolved. We estimate the uncertainties of $\sigma_{\rm spat}$ from the scatter, half of the 16th to 84th percentile range, divided by the square root of the number of independent σ measurements. To account for the systematic uncertainties from limited spectral resolution (see Appendix G), we quadratically add the resolution limit to the respective template used to determine the statistical uncertainties. Due to the number of individual spectra, the resulting uncertainties of the $\sigma_{\rm spat}$ are typically much smaller than what we get from fitting a single aperture-integrated spectrum.

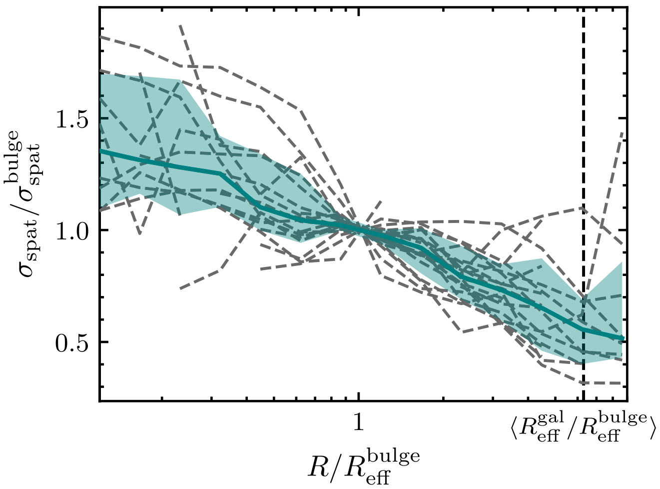

Figure 5. Radial profile of the spatially resolved stellar velocity dispersion $\sigma_{\rm spat}$ across AGN host-galaxy bulges. We measure the spatially resolved stellar dispersion $\sigma_{\rm spat}$ in concentric annuli centered on the AGN position. Values of $\sigma_{\rm spat}$ are normalized to the value measured at the bulge effective radius $R_{\rm eff}^{\rm bulge}$. Dashed lines show the spatially resolved $\sigma_{\rm spat}$ of individual AGN host galaxies; shaded green regions show the 16th to 84th percentile range of the stacked profile.

In Figure 5, we show the radial profile of the spatially resolved dispersion component $\sigma_{\rm spat}$, as a function of distance from the center R. While all late-type galaxies (LTGs) in the sample are displayed, measuring $\sigma_{\rm spat}$ in early-type galaxies (ETGs) is often not possible due to the bright AGN, or $\sigma_{\rm spat}$ only sparsely samples the R range; therefore, these are not included. The spatially resolved stellar dispersion of LTGs exhibits a steep radial profile. While, on average, the offset between $\sigma_{\rm spat}$ measured at $R_{\rm eff}^{\rm gal}$ and $R_{\rm eff}^{\rm bulge}$ is a factor of 1.9 ± 0.4, it can be as large as a factor of 3 for individual galaxies. This underscores the importance of considering the aperture size over which $\sigma_{\rm spat}$ is measured.

4.4.3. Aperture-integrated Kinematics

Another approach is to coadd the spectra in a given aperture, providing a rotationally broadened spectrum, from which the aperture-integrated kinematics can be derived. We refer to this quantity as the *aperture-integrated* stellar velocity dispersion $\sigma_{\rm ap}$. Since the most luminous AGNs are typically hosted by ETGs, which do not exhibit a detectable disk component, disk rotational broadening is expected to contribute a minor contamination in $\sigma_{\rm ap}$. Varying the aperture size allows us to study the radial behavior of $\sigma_{\rm ap}$ across different morphological components. More precisely, we trace bulge velocity dispersion $\sigma_{\rm ap}^{\rm bulge}$ or galaxy-wide velocity dispersion $\sigma_{\rm ap}^{\rm gal}$ by aligning the aperture with the bulge's luminosity-weighted centroid and

Table 4
Stellar Velocity Dispersion Measurements

AGN Name (1)	$\sigma_{\rm ap}^{\rm gal}$ (km s^{-1}) (2)	$\sigma_{\rm ap}^{\rm bulge}$ (km s^{-1}) (3)	$\sigma_{\rm spat}^{\rm gal}$ (km s^{-1}) (4)	$\sigma_{\rm spat}^{\rm bulge}$ (km s^{-1}) (5)	Lit. σ (km s^{-1}) (6)	Lit. σ Reference (7)	$M_{\rm bulge,dyn}$ [log $M_\odot$] (8)	$M_{\rm gal,dyn}$ [log $M_\odot$] (9)
NGC 3227	140 ± 11	133 ± 11	133 ± 9	118 ± 8	92 ± 6	W13	9.23 ± 0.23	10.49 ± 0.23
NGC 6814	107 ± 9	95 ± 8	109 ± 8	92 ± 7	69 ± 3	B17	8.96 ± 0.25	10.59 ± 0.23
NGC 4593	146 ± 12	142 ± 11	119 ± 8	110 ± 8	144 ± 5	B17	10.18 ± 0.23	10.64 ± 0.23
NGC 3783	104 ± 8	130 ± 10	93 ± 7	122 ± 9	95 ± 10	O04	9.72 ± 0.23	10.32 ± 0.23
NGC 2617	84 ± 9	114 ± 9	83 ± 6	109 ± 8	128 ± 9	C23	9.52 ± 0.23	10.24 ± 0.29
IC 4329 A	165 ± 13	172 ± 14	142 ± 10	166 ± 12			10.27 ± 0.23	11.32 ± 0.23
Mrk 1044	84 ± 7	76 ± 7	76 ± 8	⋯			9.01 ± 0.24	9.99 ± 0.24
NGC 5548	163 ± 13	163 ± 13	154 ± 11	154 ± 11	162 ± 12	B17	10.72 ± 0.23	10.85 ± 0.23
NGC 7469	129 ± 10	131 ± 10	111 ± 8	113 ± 8	131 ± 5	N04	10.53 ± 0.23	10.56 ± 0.23
Mrk 1310	82 ± 7	82 ± 7	74 ± 5	74 ± 5	84 ± 5	W10	9.90 ± 0.23	9.89 ± 0.23
Mrk 1239	99 ± 8	† 99 ± 8	⋯	⋯			9.95 ± 0.33	9.95 ± 0.33
Arp 151	120 ± 10	† 120 ± 10	113 ± 8	† 113 ± 8	118 ± 4	W10	10.13 ± 0.33	10.13 ± 0.33
Mrk 50	91 ± 10	† 91 ± 10	73 ± 5	† 73 ± 5	109 ± 14	B11	10.05 ± 0.38	10.05 ± 0.38
Mrk 335	66 ± 6	† 66 ± 6	⋯	⋯			9.63 ± 0.36	9.63 ± 0.36
Mrk 590	184 ± 15	189 ± 15	168 ± 12	178 ± 12	189 ± 6	N04	10.28 ± 0.23	10.40 ± 0.23
SBS 1116+583A	77 ± 10	77 ± 10	60 ± 5	74 ± 5	92 ± 4	W10	9.13 ± 0.33	9.98 ± 0.32
Zw 229-015	83 ± 16	88 ± 7	77 ± 5	70 ± 6			9.37 ± 0.23	10.30 ± 0.45
Mrk 279	158 ± 13	160 ± 13	109 ± 8	129 ± 9	156 ± 17	B17	10.41 ± 0.23	10.65 ± 0.23
Ark 120	168 ± 13	182 ± 15	133 ± 9	160 ± 11	192 ± 8	W13	10.48 ± 0.23	10.87 ± 0.23
3C 120	178 ± 14	† 178 ± 14	⋯	⋯	162 ± 20	N95	10.59 ± 0.33	10.59 ± 0.33
MCG +04-22-042	170 ± 14	183 ± 15	85 ± 6	173 ± 12			10.16 ± 0.23	11.20 ± 0.23
Mrk 1511	87 ± 7	106 ± 11	87 ± 6	104 ± 7	115 ± 9	C23	9.39 ± 0.27	10.62 ± 0.23
PG 1310–108	94 ± 8	129 ± 11	70 ± 8	⋯			9.53 ± 0.24	10.13 ± 0.24
Mrk 509	130 ± 10	† 130 ± 10	⋯	⋯	184 ± 12	G13	10.29 ± 0.33	10.29 ± 0.33
Mrk 110	100 ± 8	† 100 ± 8	95 ± 8	† 95 ± 8	91 ± 9	C23	9.89 ± 0.34	9.89 ± 0.34
Mrk 1392	168 ± 13	181 ± 15	140 ± 10	⋯	161 ± 9	C23	10.09 ± 0.23	11.17 ± 0.23
Mrk 841	115 ± 9	† 115 ± 9	109 ± 8	† 109 ± 8			10.39 ± 0.33	10.39 ± 0.33
Zw 535-012	152 ± 12	164 ± 13	106 ± 7	⋯			10.01 ± 0.23	10.94 ± 0.23
Mrk 141	130 ± 10	131 ± 12	77 ± 8	⋯	135 ± 5	C23	9.59 ± 0.26	10.74 ± 0.23
RBS 1303	203 ± 16	208 ± 17	134 ± 9	176 ± 12			10.37 ± 0.23	11.23 ± 0.23
Mrk 1048	193 ± 15	237 ± 19	179 ± 13	223 ± 16			10.95 ± 0.23	11.42 ± 0.23
Mrk 142	85 ± 11	87 ± 13	54 ± 5	⋯			9.29 ± 0.37	10.39 ± 0.34
RX J2044.0+2833	141 ± 11	153 ± 12	84 ± 7	⋯			9.59 ± 0.23	10.76 ± 0.23
IRAS 09149–6206	155 ± 12	† 155 ± 12	123 ± 9	† 123 ± 9			10.99 ± 0.33	10.99 ± 0.33
PG 2130+099	173 ± 14	160 ± 16	111 ± 8	⋯	163 ± 19	G13	9.88 ± 0.27	10.80 ± 0.23
NPM 1G+27.0587	150 ± 13	183 ± 15	93 ± 6	⋯			10.24 ± 0.23	11.09 ± 0.25
RBS 1917	90 ± 10	101 ± 10	⋯	⋯			8.99 ± 0.26	10.08 ± 0.29
PG 2209+184	136 ± 11	136 ± 11	113 ± 8	113 ± 8			10.70 ± 0.23	10.70 ± 0.23
PG 1211+143	101 ± 11	† 101 ± 11	⋯	⋯			9.24 ± 0.39	9.24 ± 0.39
PG 1426+015	186 ± 15	† 186 ± 15	171 ± 12	† 171 ± 12	217 ± 15	W08	10.89 ± 0.33	10.89 ± 0.33
Mrk 1501	97 ± 10	† 97 ± 10	⋯	⋯			10.76 ± 0.38	10.76 ± 0.38
PG 1617+175	174 ± 20	† 174 ± 20	⋯	⋯	201 ± 37	G13	10.72 ± 0.40	10.72 ± 0.40
PG 0026+129	233 ± 21	† 233 ± 21	⋯	⋯			11.35 ± 0.35	11.35 ± 0.35
3C 273	214 ± 17	† 214 ± 17	⋯	⋯	210 ± 10	H19	11.31 ± 0.33	11.31 ± 0.33

Note. AGNs are listed in order of increasing redshift (as in Table 1). Column (1): AGN name. Column (2): aperture-integrated σ over $R_{\rm eff}^{\rm gal}$. Column (3): aperture-integrated σ over $R_{\rm eff}^{\rm bulge}$. Values marked with (†) are ETGs, for which $R_{\rm eff}^{\rm bulge} = R_{\rm eff}^{\rm gal}$, and thus $\sigma^{\rm bulge} = \sigma^{\rm gal}$ are equal. Column (4): spatially resolved σ over $R_{\rm eff}^{\rm gal}$. Column (5): spatially resolved σ over $R_{\rm eff}^{\rm bulge}$. Column (6): stellar velocity dispersion reported in the literature. Column (7): reference for the literature σ. Column (8): logarithm of the bulge dynamical mass. Column (8): logarithm of the galaxy dynamical mass. Reference keys are as follows: N95: C. H. Nelson & M. Whittle (1995); N04: C. H. Nelson et al. (2004); O04: C. A. Onken et al. (2004); W08: L. C. Watson et al. (2008); W10: J.-H. Woo et al. (2010); B11: A. J. Barth et al. (2011); G13: C. J. Grier et al. (2013); W13: J.-H. Woo et al. (2013); B17: M. Batiste et al. (2017a); H19: B. Husemann et al. (2019); C23: T. Caglar et al. (2023).

matching its size to $R_{\rm eff}^{\rm bulge}$. More details on comparing aperture-integrated with spatially resolved measurements of σ are described in Appendix C. While this approach reduces the spatial resolution of the radial axis, coadding the spectra has the advantage of a substantially higher S/N. This is particularly beneficial for luminous AGNs, where extracting $\sigma_{\rm spat}$ is often hampered by the poor contrast between the AGN continuum and the underlying stellar absorption lines. Moreover, using aperture-integrated spectra diminishes the contribution from systematic artifacts caused by PSF subtraction, which can be especially severe near the galaxy center.

The results of measuring the dispersion using the two methods are summarized in Table 4 and illustrated in Figure 6. Overall, the values of $\sigma_{\rm ap}^{\rm bulge}$ tend to be higher than those of $\sigma_{\rm ap}^{\rm gal}$. Averaged over the entire sample, this offset is small (7 km s^{-1}, or 5%), likely related to $\sigma_{\rm ap}^{\rm gal}$ capturing significant rotational broadening from galaxy disk that flattens any aperture-size dependence if the galaxy disk is viewed at high inclination (see

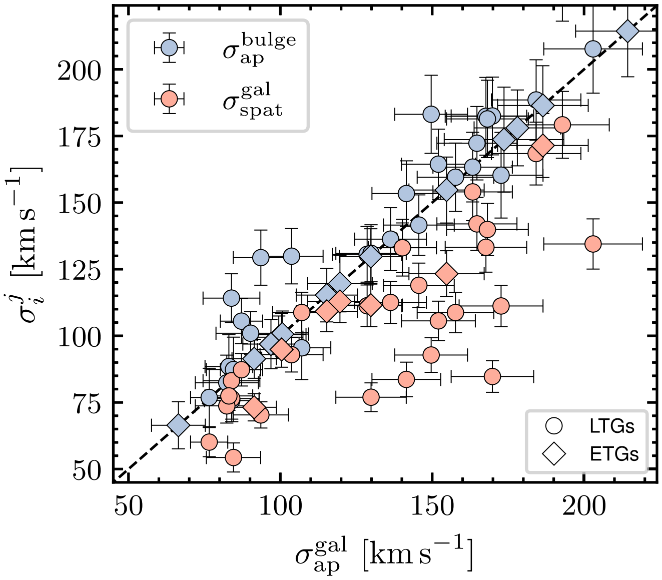

Figure 6. Comparing methods for measuring stellar velocity dispersion. Aperture-integrated dispersion measured over $R_{\rm eff}^{\rm gal}$ is shown on the x-axis. On the y-axis, we show the aperture-integrated dispersion over $R_{\rm eff}^{\rm bulge}$ (blue) and the spatially resolved dispersion over $R_{\rm eff}^{\rm gal}$ (orange), respectively. Compared to the one-to-one correlation, denoted by the dashed line, the mean bulge dispersion is on average slightly higher than the dispersion measured across the galaxy. In contrast, spatially resolving the kinematics results in significantly lower dispersion.

Section 5.1.1). More notably, on galaxy scales, $\sigma_{\rm spat}^{\rm gal}$ is smaller than $\sigma_{\rm ap}^{\rm gal}$ by, on average, 25 km s^{-1}, or 12%. Comparing the same for the bulge, $\sigma_{\rm spat}^{\rm bulge}$ versus $\sigma_{\rm ap}^{\rm bulge}$ yields a similar but less pronounced offset of 9%, suggesting an increased contribution from rotational broadening when using galaxy-integrated kinematics. The stellar velocity dispersion measurements reported in the literature often differ substantially from our measurements for individual objects. These discrepancies may arise not only from the different diagnostic features used to constrain the stellar kinematics, e.g., Mg Ib λλλ5167, 5173, 5184 (M. Batiste et al. 2017a; B. Husemann et al. 2019), Ca II λλλ8498, 8542, 8662 (C. A. Onken et al. 2004; J.-H. Woo et al. 2010; T. Caglar et al. 2023), Ca II H&K λλ3969 and 3934 (V. N. Bennert et al. 2015), and Mg I+CO (L. C. Watson et al. 2008; C. J. Grier et al. 2013). For instance, C. E. Harris et al. (2012) report that the average differences are $\langle \sigma_{\rm Mg\,Ib}/\sigma_{\rm CaT} \rangle = -0.02 \pm 0.01$, i.e., a 5% bias, which depends on aperture size. Furthermore, varying aperture sizes across which these literature values are reported may introduce additional scatter. While galaxy morphology is often unexplored in previous studies, our method for measuring stellar velocity dispersion controls for these systematic uncertainties, making our measurements more robust.

Aperture-integrated measurements can be reconstructed from spatially resolved measurements, as we demonstrate in Appendix C. Based on these results, we conclude that, across galaxy disks, we can robustly disentangle the contributions of rotation from those of chaotic motions. However, we note that substructures like fast- or counterrotating disks, which are often observed on scales of several hundred parsecs (S. Comeron et al. 2010; D. A. Gadotti et al. 2020) below the typical ∼arcsec sizes of our bulges, remain unresolved in the majority of AGNs in our sample.

4.4.4. Systematic Uncertainties for Measuring σ

To achieve a more accurate calibration of the $M_{\rm BH}$–host-galaxy scaling relations in AGNs, our approach involves the most precise $M_{\rm BH}$ and σ measurements available. Although the wide dynamic range of AGN parameters is a strength of the sample, it also presents technical challenges in identifying host-galaxy morphological components (see V. N. Bennert et al. 2024, in preparation). At the low-z end, for example, NGC 3227, NGC 4593, and NGC 7469 are cases where plenty of kinematic substructure is resolved, including spiral arms, dust lanes, nuclear rings, nuclear disks, or bulges. In such cases, the simplistic parameterization (s, sd, sdb) is insufficient to describe the morphology accurately (however, the photometry for the main components is adequately recovered even by a simple model). For the more distant and luminous AGNs in the sample, the PSF subtraction often leaves strong residuals that dominate over the host galaxy on arcsecond scales. In cases where these residuals coincide with the typical sizes of the bulges, it is impossible to measure accurate bulge sizes. Also, the choice of parameterizing host-galaxy morphology can affect $R_{\rm eff}^{\rm bulge}$ for individual objects. However, for most of the sample, the parameterization is clear, and even in ambiguous cases, adding a component has little impact on the measured sizes.

Another source of systematic uncertainty comes from measuring the kinematics from the IFU data. For the nearest AGNs, the FOV of the IFU is smaller than $R_{\rm eff}^{\rm gal}$. In contrast, for the more distant AGNs, the lower physical spatial resolution and AGN continuum blending does not allow us to measure σ within $R_{\rm eff}^{\rm gal}$. Moreover, beam smearing might contribute to smoothing the radial profiles of $\sigma_{\rm spat}$ on small scales, e.g., in Figure 5. However, this effect cannot be homogeneously controlled without degrading individual data sets. From the aperture sizes and methods defined in Section 4.4.1, $\sigma_{\rm ap}^{\rm gal}$ provides the measurement that is the least sensitive to systematic effects: only for four of 44 bright AGNs (PG 1211+143, PG 1617+175, PG 0026+129, 3C 273) is $\sigma_{\rm ap}^{\rm gal}$ impacted by the PSF subtraction, adding systematic uncertainties of ∼5%. This is caused by a few spaxels that contain signal from the host galaxy heavily blended by AGN emission. When excluding these four objects, the slope and intercept of the spatially resolved $\sigma_{\rm spat}^{\rm gal}$ relation is <3%. With such small variation, we consider the systematic uncertainty for calibrating the $M_{\rm BH}$–σ relation small.

4.5. Dynamical Masses

Based on the kinematics recovered in the previous section, we can derive dynamical masses as

$$M_{\rm dyn} = c R_{\rm eff} \sigma_{\rm ap}^2 / G, \tag{3}$$

where c is a structural constant that depends on the anisotropy of the system (S. Courteau et al. 2014). While the value of $M_{\rm dyn}$ for ETGs is best described by the coefficient $c = 2.5$ (M. Cappellari et al. 2006), we adopt $c = 3$ for both LTGs and ETGs, guaranteeing a consistent comparison with the literature (e.g., V. N. Bennert et al. 2021). For LTGs specifically, we adopt $R_{\rm eff}^{\rm bulge}$ and $\sigma_{\rm ap}^{\rm bulge}$ to get the dynamical bulge mass $M_{\rm bulge,dyn}$. For ETGs, we adopt the parameters that belong to the spheroid, i.e., $R_{\rm eff}^{\rm bulge}$ and $\sigma_{\rm ap}^{\rm bulge}$, and also refer to the derived dynamical mass as $M_{\rm bulge,dyn}$. With this definition, $M_{\rm bulge,dyn}$

provides a consistent metric for the dynamical mass of the spheroidal component for both LTGs and ETGs.

4.6. Fitting the M_{BH} Scaling Relations

The $M_{\rm BH}$ scaling relations are parameterized as

$$\log\left(\frac{M_{\rm BH}}{M_\odot}\right) = \alpha + \beta\log X, \tag{4}$$

where X is the host-galaxy parameter, in our case either $\sigma_\star/200\,{\rm km\,s^{-1}}$ or $M_{\rm bulge,dyn}/10^{11}M_\odot$. We fit the relation using the hierarchical Bayesian model `LINMIX_ERR` from B. C. Kelly (2007), which performs a linear regression to observed independent variables x_i and dependent variables y_i, accounting for the associated uncertainties of both. We rescale the variables to the mean of their respective distributions to reduce the covariance between the parameters. Monitoring the convergence to a well-sampled posterior distribution allows us to infer realistic uncertainties of the derived fitting parameters, which also include the intrinsic scatter of the relation ϵ. Compared to other regression methods that are often used to constrain the $M_{\rm BH}$ scaling relations, namely `BCES` (M. G. Akritas & M. A. Bershady 1996), `FITEXY` (S. Tremaine et al. 2002), or `maximum likelihood` (K. Gültekin et al. 2009; J.-H. Woo et al. 2010), `LINMIX_ERR` is more general and produces a larger intrinsic scatter (D. Park et al. 2012). For our analysis, we assume that the measurement uncertainties of $M_{\rm BH}$ and σ are symmetric in log space, and symmetrize the measurement uncertainties on $M_{\rm BH}$ from their upper and lower 1σ intervals listed in Table 1. We note that the adopted choice of uncertainties does not significantly impact the results, which has already been reported by D. Park et al. (2012).

5. Results and Discussion

5.1. Host-galaxy Morphologies

If major mergers are responsible for shaping the $M_{\rm BH}$ scaling relations, only the host-galaxy morphological components bearing the dynamical imprint of merger history should correlate with $M_{\rm BH}$, i.e., classical bulges (M. Cisternas et al. 2011a, 2011b; J. Kormendy & L. C. Ho 2013; V. N. Bennert et al. 2015). While the dependence of the $M_{\rm BH}$ scaling relations on host morphology has been extensively studied for quiescent galaxies (e.g., K. Gültekin et al. 2009; J. E. Greene et al. 2010; N. J. McConnell & C.-P. Ma 2013; G. A. D. Savorgnan & A. W. Graham 2015; N. Sahu et al. 2019; A. W. Graham 2023), they are less well constrained for AGNs due to the bright AGN emission (e.g., V. P. Debattista et al. 2013; M. Hartmann et al. 2014; see also Section 3.1.4) or the narrow dynamic range in $M_{\rm BH}$ covered (e.g., V. N. Bennert et al. 2021).

In our sample, 29/44 (66%) of AGNs are hosted by LTGs. However, disks may remain undetected at high bulge-to-disk ratios, so our estimate should be regarded as an upper limit. Nevertheless, the fraction is comparable to the fraction of Seyfert hosts with disk-like galaxies among the overall AGN population (e.g., ∼52% in CANDELS (D. D. Kocevski et al. 2012), or 74% of disk galaxies in CARS (B. Husemann et al. 2022)); the depth and angular resolution of the HST photometry in our study allow us to identify disk components more robustly than previous studies. V. N. Bennert et al. (2021), who used the same methodology as in this work, reported an even higher fraction (95%) of disk galaxies among local AGNs imaged with HST.

Among the sample of AGNs hosted by disk galaxies, 15/29 show a clear sign of a bar, and are better fitted when including a bar component in the model. The intrinsic fraction of bars might be higher, since we used a conservative approach by only including a bar when there are clear signs in the PSF-subtracted images. Moreover, a few galaxies have too high a disk inclination to identify a bar (for details, see V. N. Bennert et al. 2024, in preparation). Typically, the bar fractions of disk-like AGN hosts are reported to be higher (e.g., M. Cisternas et al. 2011a; M. S. Alonso et al. 2013; B. Husemann et al. 2022). However, we caution against direct comparisons of the bar incidence rate with other surveys, since identification methods, image quality, and intrinsic bar strengths have a significant impact on these numbers, similar to the disk/nondisk classification. In particular, the bar fraction also depends on wavelength range, where higher bar fractions are observed in the infrared compared to identification based on optical photometry (e.g., P. B. Eskridge et al. 2000; R. J. Buta et al. 2015; P. Erwin 2019).

While 10/44 galaxies have irregular or asymmetric morphologies, only two objects show strong signs of interaction or merger activity (Arp 151 and Mrk 1048). This corresponds to 5%, which is consistent with the low fraction of strongly disturbed hosts in the overall AGN population (e.g., M. Cisternas et al. 2011a; K. Schawinski et al. 2012; M. Mechtley et al. 2016; V. Marian et al. 2019; M. Kim et al. 2021). As we will demonstrate in Section 5.3.1, interacting galaxies do not represent the strongest outliers to the $M_{\rm BH}$ scaling relations and are included in the following analysis.

5.1.1. Correcting Aperture Effects

As spatially resolved studies will remain unavailable for the majority of distant type 1 AGNs in the Universe, aperture-integrated spectra are often the only means to trace stellar kinematics from bulge to galaxy scales. We therefore investigate the systematic differences induced by the aperture size, depending on host-galaxy morphology. While differences between $\sigma_{\rm ap}$ and $\sigma_{\rm spat}$ for individual AGNs are detailed in Appendix F, we shall here only focus on the sample-integrated behavior and dependencies on morphology.

The spatially resolved kinematics shown in Figure 5 illustrate how galaxy kinematic substructures may impact measurements of σ: for LTGs with spatially resolved kinematics, the sample-averaged normalized $\sigma_{\rm spat}$ exhibits a steep radial profile, underscoring the importance of considering the aperture over which $\sigma_{\rm spat}$ is extracted.

Aperture-correction recipes are often formulated in the form of a power law:

$$\frac{\sigma}{\sigma_{\rm eff}} = \left(\frac{R}{R_{\rm eff}}\right)^{\gamma}. \tag{5}$$

For quiescent ETGs, it is established that $\sigma_{\rm ap}$ typically decreases with increasing aperture size to the center, resulting in $\gamma = -0.04$ (I. Jorgensen et al. 1995), $\gamma = -0.06$ (D. Mehlert et al. 2003), or $\gamma = -0.066$ (M. Cappellari et al. 2006). The few

ETGs in our sample are poorly resolved, so that a statistical analysis of the aperture-size dependence is not possible.

For quiescent LTGs, recent studies have shown that aperture correction is more complex, due to multiple kinematic components and their anisotropy. However, compared to galaxy stellar mass and luminosity, we suspect that the galaxy inclination i has the largest effect on measuring $\sigma_{\rm ap}$ in our AGN sample (Section 5.3). Galaxy-scale kinematics derived from aperture-integrated spectra of highly inclined disk galaxies are more affected by rotational broadening compared to low-inclination disk galaxies. This is reflected in the top panels of Figure 7, where only disk galaxies viewed at lower inclinations exhibit a trend of $\sigma_{\rm ap}$ with varying $R_{\rm ap}$, whereas higher-inclination disk galaxies show no significant trend. This is a result of two opposing trends that cancel each other out at high inclination: stellar velocity dispersion increases toward the center due to either dynamically hotter bulges or spatially unresolved rotating nuclear disks (see discussion in Section 4.4.4), but rotational broadening from the galaxy disk only becomes important at a larger distance from the galaxy center. Although $\sigma_{\rm ap}$ is sometimes measured in elliptical apertures, as for instance in J. Falcón-Barroso et al. (2017), measurements in circular apertures are the default for survey data. To control for inclination, we included the disk inclination i in the parameterization of the aperture correction:

$$\frac{\sigma}{\sigma_{\rm eff}} = \left(\frac{R}{R_{\rm eff}}\right)^{\gamma\cdot\cos(i)}. \tag{6}$$

Fitting the logarithmic relation with a least-squares minimization provides the best-fit aperture-correction exponent $\gamma = -0.063 \pm 0.013$. This value is surprisingly consistent with the aperture correction suggested for ETGs, indicating that, when correcting for disk inclination, the $\sigma_{\rm ap}$ correction of disk galaxies is similar to that of pure spheroidals. However, the significant residual structure of individual galaxies demonstrates that additional parameters must be considered, such as galaxy stellar mass or luminosity (J. Falcón-Barroso et al. 2017; K. Zhu et al. 2023). For our AGNs, however, the small sample size does not allow us to further constrain second-order dependencies on host-galaxy luminosity or stellar mass.

5.2. The M_{BH} Scaling Relations of Quiescent Galaxies

The $M_{\rm BH}$–σ relation of the local quiescent galaxy population has been studied across a higher $M_{\rm BH}$ dynamic range compared to that of AGNs (K. Gültekin et al. 2009; J. Kormendy & L. C. Ho 2013; N. J. McConnell & C.-P. Ma 2013). KH13 compiled $M_{\rm BH}$ and the “effective dispersion” $\sigma_{\rm eff}$, which they measured within $R_{\rm eff}^{\rm gal}/2$. Their method involves the intensity-weighted mean of $v^2 + \sigma^2$, which is close to the definition of our $\sigma_{\rm ap}$ (see Appendix C). For a consistent analysis, we have refit the $M_{\rm BH}$–σ and $M_{\rm BH}$–$M_{\rm dyn}$ relation from KH13 with our method (Section 4.6). The results are listed in row (i) of Table 5 and reproduce the parameters that have originally been reported.

However, the KH13 sample mainly covers the high-$M_{\rm BH}$ regime, where RM AGNs are scarce. For LTGs at the low-$M_{\rm BH}$ end of the relation, rotational broadening from disk components are nonnegligible, and thus the aperture size over which the kinematics are extracted must be considered. Based on a sample of both LTGs and ETGs, M. Batiste et al. (2017a) made comparisons using an aperture-correction factor to estimate $\sigma_{\rm ap}^{\rm gal}$ versus direct measurements of $\sigma_{\rm spat}^{\rm gal}$. While the former approach has been widely used in the literature, M. Batiste et al. (2017a) stress that not only are the effective radii used in the literature uncertain, but also the recovered $\sigma_{\rm spat}^{\rm gal}$ are systematically lower by 13 km s^{-1} compared to $\sigma_{\rm ap}^{\rm gal}$. As a consequence, $M_{\rm BH}$–σ calibrations using $\sigma_{\rm ap}$ are offset toward higher intercepts, and tend to result in steeper slopes (e.g., C. J. Grier et al. 2013, $\beta = 5.04$; J.-H. Woo et al. 2013, $\beta = 5.31$; G. A. D. Savorgnan & A. W. Graham 2015, 6.34 ± 0.8). When using the spatially resolved σ measurements of LTGs and ETGs, equivalent to our definition of $\sigma_{\rm spat}$, M. Batiste et al. (2017a) found $\alpha = 8.66 \pm 0.09$ and $\beta = 4.76 \pm 0.60$, which are more consistent with the KH13 relation.

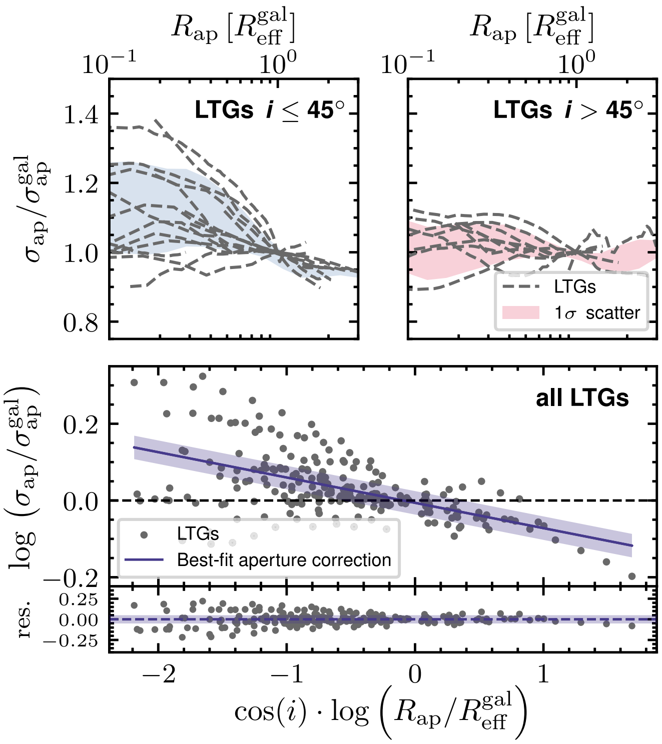

Figure 7. Inclination-dependent aperture correction for stellar velocity dispersion measurements. Top: left and right panels show the behavior of $\sigma_{\rm spat}$ as a function of aperture size normalized by the galaxy effective radius, split by disk inclination. Gray dashed lines correspond to individual galaxies, whereas shaded regions denote the scatter (16th–84th percentile in bins of $R_{\rm ap}$). Varying $R_{\rm ap}$ significantly affects $\sigma_{\rm ap}$ only for the lower-inclination systems. Bottom: considering all disk galaxies of the AGN sample, we control for inclination by parameterizing the aperture-correction formula with Equation (5). A first-order power law describes the overall trend of decreasing $\sigma_{\rm ap}$ with increasing $R_{\rm ap}$ (top panel), but a significant residual structure indicates that galaxy-to-galaxy variation remains likely driven by stellar mass or luminosity.

5.3. The M_{BH} Scaling Relations of AGNs

In previous studies, fitting the $M_{\rm BH}$–σ relation of type 1 AGNs required an additional free parameter, the unknown virial factor f. To overcome the limited dynamic range when inferring the AGN relation’s scatter and intercept (and thereby a sample-average $\langle f\rangle$), previous calibrations often required fixing the slope to that of quiescent galaxies. This implicitly assumes that AGNs and quiescent galaxies follow the same underlying relations, and selection effects are negligible. However, so far, this assumption does not have any empirical foundation. In fact, AGNs represent the sites of ongoing

Table 5
Results of Fitting the Scaling Relations of Local AGNs and Quiescent Galaxies

X in Relation (1)	Sample (2)	$M_{\rm BH}$ Distr. (3)	Aperture (4)	Method (5)	Symbol (6)	α (7)	β (8)	ϵ (9)	Row (10)
$\sigma/200$ km s^{-1}	KH13†	KH13	Galaxy*	ap.	$\sigma_{\rm ap}^{\rm gal}$	8.53 ± 0.05	4.53 ± 0.32	0.34 ± 0.04	(i)
	AGN	AGN	Bulge	ap.	$\sigma_{\rm ap}^{\rm bulge}$	**7.90 ± 0.16**	**2.53 ± 0.73**	**0.47 ± 0.08**	(ii)
	AGN	AGN	Galaxy	ap.	$\sigma_{\rm ap}^{\rm gal}$	7.93 ± 0.16	2.48 ± 0.72	0.47 ± 0.08	(iii)
	AGN	AGN	Galaxy	spat.	$\sigma_{\rm spat}^{\rm gal}$	8.06 ± 0.27	2.57 ± 0.89	0.45 ± 0.09	(iv)
	AGN	KH13	Bulge	ap.	$\sigma_{\rm ap}^{\rm bulge}$	**8.71 ± 0.13**	**4.10 ± 0.93**	**0.57 ± 0.09**	(v)
	AGN	KH13	Galaxy	ap.	$\sigma_{\rm ap}^{\rm gal}$	8.80 ± 0.13	4.51 ± 0.88	0.53 ± 0.08	(vi)
	AGN LTGs	AGN LTGs	Bulge	ap.	$\sigma_{\rm ap}^{\rm bulge}$	7.72 ± 0.16	2.80 ± 0.80	0.27 ± 0.11	(vii)
	AGN LTGs	AGN LTGs	Galaxy	ap.	$\sigma_{\rm ap}^{\rm gal}$	7.68 ± 0.18	2.17 ± 0.89	0.37 ± 0.10	(viii)
	AGN LTGs	AGN LTGs	Galaxy	spat.	$\sigma_{\rm spat}^{\rm gal}$	7.88 ± 0.27	2.47 ± 0.70	0.31 ± 0.10	(ix)
	AGN ETGs	AGN ETGs	Galaxy	ap.	$\sigma_{\rm ap}^{\rm bulge}$	8.44 ± 0.30	3.00 ± 1.28	0.54 ± 0.18	(x)
$M_{\rm bulge,dyn}/10^{11}M_{\odot}$	KH13	KH13	Bulge	ap.	$\sigma_{\rm ap}^{\rm bulge}$	8.78 ± 0.07	1.06 ± 0.10	0.45 ± 0.05	(xi)
	AGN	AGN	Bulge	ap.	$\sigma_{\rm ap}^{\rm bulge}$	**8.11 ± 0.16**	**0.70 ± 0.14**	**0.41 ± 0.08**	(xii)
	AGN	AGN	Galaxy	ap.	$\sigma_{\rm ap}^{\rm bulge}$	7.80 ± 0.19	0.83 ± 0.52	0.54 ± 0.10	(xiii)
	AGN	KH13	Bulge	ap.	$\sigma_{\rm ap}^{\rm bulge}$	**8.76 ± 0.11**	**0.87 ± 0.14**	**0.49 ± 0.07**	(xiv)

Note. All fits were calculated as part of this paper, including those to quiescent galaxies. Relations that are shown in Figure 10 are highlighted in bold. Column (1): scaling relation of the form $\log(M_{\rm BH}/M_{\odot}) = \alpha + \beta \log X$, with X given in the Table. Column (2): sample for which the $M_{\rm BH}$–σ relation was fitted. Column (3): $M_{\rm BH}$ distribution of the sample used for fitting the $M_{\rm BH}$–σ relation. The quiescent galaxy sample from KH13 serves as a reference. "AGN" refers to the (sub-)sample of AGNs, specified in column (2). "KH13" refers to the AGN sample being matched to the KH $M_{\rm BH}$ distribution, as described in Section 5.4. Column (4): aperture over which the kinematics are evaluated. Column (5): method by which the kinematics are measured; "ap." refers to aperture integrated, whereas "spat." refers to spatially resolved kinematics; see Section 4.4.1. Column (6): symbol for the stellar dispersion σ, indicating which aperture size and which method we used to measure it. Column (7): best-fit intercept of the $M_{\rm BH}$–σ relation (Equation (4)). Column (8): best-fit slope of the relation. Column (9): best-fit intrinsic scatter of the relation. Column (10): row number used to refer to the relation. (†) KH13 data refitted with our method. (*) Galaxy effective radius is poorly constrained from ground-based seeing-limited imaging, as discussed in KH13 and M. Batiste et al. (2017b).

SMBH growth, where the present-day SMBH growth may result in different $M_{\rm BH}$–host-galaxy scaling relations. To test this hypothesis, from here on, we will focus on the AGNs in our sample that have independent $M_{\rm BH}$ measurements. In contrast to previous studies, this allows us to fit the AGN $M_{\rm BH}$–σ relation without assumptions on any of the parameters. Furthermore, we control for host-galaxy morphology by using σ measured across the bulge or galaxy effective radius, and test how different methods of measuring stellar velocity dispersion impact the $M_{\rm BH}$–σ relation.

5.3.1. Impact of σ_{ap} versus σ_{spat}

The majority (29/44) of AGNs in our sample are hosted by LTGs, for which the best-fit $M_{\rm BH}$–σ relation depends on both the method by which the stellar velocity dispersion is measured (see Section 4.4.1), and aperture size. While the galaxy-wide integrated $\sigma_{\rm ap}^{\rm gal}$ is the closest to the definition used in previous studies (e.g., K. Gültekin et al. 2009; C. J. Grier et al. 2013; J. Kormendy & L. C. Ho 2013), $\sigma_{\rm spat}$ results in steeper slopes. This steepening occurs because $\sigma_{\rm spat}$ excludes rotational broadening, effectively shifting many LTGs toward lower σ (top versus bottom panel of Figure 8). This primarily affects high-inclination disk galaxies, whereas $\sigma_{\rm ap}$ includes this effect (as detailed in Section 5.1.1). The $M_{\rm BH}$–$\sigma_{\rm spat}$ relation is also offset toward a lower dispersion, consistent with findings by M. Batiste et al. (2017b), suggesting that, while $M_{\rm BH}$ *does* correlate with the velocity dispersion of galaxy disks, the underlying relations are different (see discussion in Section 5.3.2). This observation has been predicted by previous studies, which suggested that rotation effects should be corrected for the case of low-mass, disk-dominant galaxies (V. N. Bennert et al. 2011; C. E. Harris et al. 2012; J.-H. Woo et al. 2013). Despite the differences of how dispersion is extracted either with $\sigma_{\rm ap}$ or $\sigma_{\rm spat}$, the best-fit parameters listed in Table 4 rows (iii) and (iv) indicate that, on galaxy scales, both methods result in statistically consistent scaling relations. On scales of the bulge, many distant galaxies hosting a luminous AGN are dramatically blended by the AGN emission, effectively limiting our ability to resolve $\sigma_{\rm spat}$ close to the nucleus. As a result, the bulge size is smaller than $\sigma_{\rm spat}$ for 50% of the AGNs in our sample. For those objects, a robust measurement of $\sigma_{\rm spat}^{\rm bulge}$ is not feasible. The effect of fitting the $M_{\rm BH}$–σ relation of an incomplete sample is discussed in Section 5.3.5.

5.3.2. Impact of Host-galaxy Morphology

The dependence of the $M_{\rm BH}$ scaling relation on host-galaxy morphology is crucial for understanding its physical drivers (e.g., N. Sahu et al. 2019; A. W. Graham 2023). However, studying host galaxies in AGNs, especially at the high-$M_{\rm BH}$ end, has been challenging. With high-quality spectroscopic data, we can now examine the morphology dependence of the $M_{\rm BH}$–σ scaling relation, focusing on the relative behavior of LTGs and ETGs, with best-fit parameters detailed in rows (vii)–(x) of Table 5.

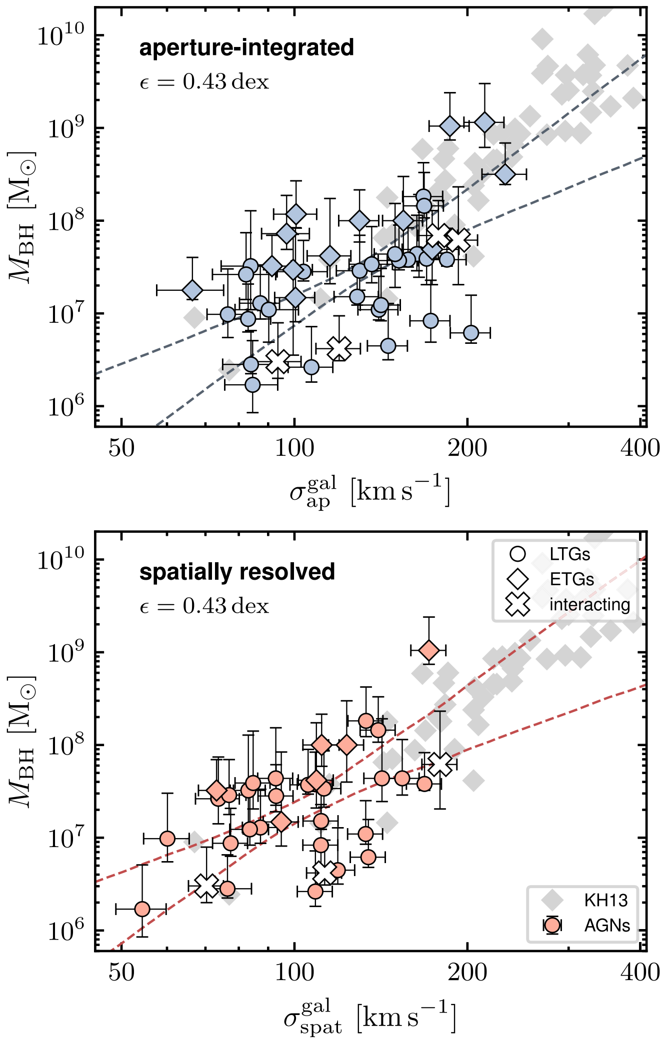

Figure 8. Effect of using aperture-integrated vs. spatially resolved σ on the $M_{\rm BH}$–σ scaling relation. Top: observed relation of AGNs based on $\sigma_{\rm ap}^{\rm gal}$ (row (iii) in Table 5). AGNs show a large scatter, and individual measurements have high uncertainty so that α and β are not well constrained. Overall, the AGNs in our sample form the extension of quiescent galaxies toward lower $M_{\rm BH}$. Interacting galaxies tend to have lower $M_{\rm BH}$, but they are not the ones that deviate the most from the relation. Bottom: observed relation of AGNs based on $\sigma_{\rm spat}^{\rm gal}$ (row (iv) in Table 5). Removing rotational broadening reduces the uncertainty of individual measurements. While the resulting $M_{\rm BH}$–σ correlation is more significant (larger β) and has a higher intercept, its intrinsic scatter is the same as when using $\sigma_{\rm ap}$.

5.3.3. Late-type AGN Hosts

Only 15/44 AGN host galaxies in our sample are classified as ETGs, whereas the majority (29/44) are hosted by LTGs. In general, constraining the AGN sample to LTGs significantly lowers the intercept and flattens the observed relation (see row (vii)–(iv) of Table 5). While this might partially be caused by quiescent LTGs following a shallower $M_{\rm BH}$–σ relation compared to ETGs (N. Sahu et al. 2019), the smaller $M_{\rm BH}$ dynamic range covered may also contribute to the observed shallower slope (see Section 5.1.1). Of any method and aperture size used for fitting LTGs, the correlation of $M_{\rm BH}$ with $\sigma_{\rm ap}^{\rm bulge}$ has parameters that are the closest to those of quiescent galaxies. This $M_{\rm BH}$–$\sigma_{\rm ap}^{\rm bulge}$ relation also shows the least intrinsic scatter of all AGN subsamples. However, this might be driven by selection effects: SMBHs are not detected in every LTG, whereas here we are only selecting those that harbor one. We might therefore only be sensitive to the upper envelope of the underlying scaling relation. As found for the entire AGN sample in Section 5.3.1, the galaxy-wide stellar velocity dispersion $\sigma^{\rm gal}$ correlates with $M_{\rm BH}$ of LTG AGNs in a relation that shows small intrinsic scatter. Compared to $\sigma_{\rm ap}^{\rm gal}$, the correlation is slightly more pronounced for $\sigma_{\rm spat}^{\rm gal}$, which is largely rotation free and thus traces the older, dynamically hot stellar component of the galaxy disk. Such a correlation is in contradiction to previous studies (e.g., J. E. Greene et al. 2010; J. Kormendy et al. 2011; J. Kormendy & L. C. Ho 2013), which argued that $M_{\rm BH}$ does not correlate with the properties of the disk. These studies suggest that stellar feedback, rather than BH feedback, plays a more significant role in regulating the growth of galaxy disks. While this might be true for the dynamically cold component, recently formed inside out through smooth gas accretion (e.g., C. Pichon et al. 2011; K. El-Badry et al. 2018), there is no a priori reason to assume that an old disk component should not be affected by early BH feedback, similar to classical bulges. Indeed, recent observations showed that galaxy disk progenitors had already formed at z>3 (e.g., F. Lelli et al. 2021; L. Ferreira et al. 2023; C. Jacobs et al. 2023; B. E. Robertson et al. 2023; F. Roman-Oliveira et al. 2023), well before the peak of cosmic SMBH growth, potentially carrying information about the SMBH-galaxy coevolution. In this context, the $M_{\rm BH}$–$\sigma_{\rm spat}^{\rm gal}$ correlation suggests that SMBHs *do* coevolve with galaxy disks, but this may be limited to early epochs of galaxy disk formation, as traced by the dynamically hot disk component.

5.3.4. Early-type AGN Hosts

Among the ETGs, only Arp 151, Mrk 110, and Mrk 335 have lower $M_{\rm BH}$, comparable to what is typically found in LTGs, whereas the remaining 12 ETGs occupy the high-$M_{\rm BH}$ end of the scaling relation. J.-H. Woo et al. (2013) argued that such massive SMBHs are typically hosted by massive galaxies for which the difference between the methods for measuring σ should be minimal. Assuming the $M_{\rm BH}$–$M_{\rm dyn}$ relation of AGNs from J. Kormendy & L. C. Ho (2013; $\alpha = 8.49$, $\beta = 1.16$), the average dynamical mass of ETGs is $\log(M_{\rm dyn}/M_\odot) \sim 11.1$, a regime where it is likely that the galaxies are slow rotators (E. Emsellem et al. 2007). Their stellar kinematics have negligible rotational support, as reflected in the parameter $\lambda_R < 0.1$, where $\lambda_R \equiv \langle R|v|\rangle \big/ \langle\sqrt{v^2 + \sigma^2}\rangle$ is a proxy to quantify the observed projected stellar angular momentum per unit mass (E. Emsellem et al. 2011). Therefore, the contribution from rotational broadening to the kinematics derived from their aperture spectra should be small. We confirm that, for ETGs, the difference between $\sigma_{\rm spat}$ and $\sigma_{\rm ap}$ is small: the choice of $\sigma_{\rm ap}^{\rm gal}$ and $\sigma_{\rm spat}^{\rm gal}$ has little effect on the dispersion (see Figure 6). In the $M_{\rm BH}$–σ plane, ETGs predominantly fall into the high-$M_{\rm BH}$ regime where their location aligns with the relation of quiescent galaxies. The observed relation of AGN ETGs is flatter than that of quiescent galaxies, but not as flat as that of LTGs. Since the ETGs sample a broader dynamic range in $M_{\rm BH}$, this flattening likely arises from differences in the $M_{\rm BH}$ distribution (see Section 5.4). Overall, the slope and intercept are similar to those of AGN LTGs within the uncertainties, suggesting that both follow the same underlying $M_{\rm BH}$–σ relation.

5.3.5. Intrinsic Scatter

Constraining the intrinsic scatter of the AGNs' $M_{\rm BH}$–σ relation is complicated by the narrow dynamic range in $M_{\rm BH}$. Furthermore, the f factor could historically only be constrained as a sample-average value, which introduced additional scatter to the $M_{\rm BH}$–σ relation. Individual f factors can vary due to different BLR geometries and viewing angles by more than an order of magnitude, and scatter by 0.41 dex (L. Villafaña et al. 2023; see also Section 5.5). J.-H. Woo et al. (2010), who were the first to simultaneously constrain slope and intrinsic scatter on the RM AGN sample, report $\epsilon = 0.43$ based on the RM AGN sample. Since then, calibrations for AGNs seem to have converged around this value; e.g., J.-H. Woo et al. (2015) find $\epsilon = 0.41 \pm 0.05$, V. N. Bennert et al. (2021) find $\epsilon = 0.42 \pm 0.08$, and T. Caglar et al. (2023) determine $\epsilon = 0.32 \pm 0.06$. However, previous studies have either suffered from a narrow dynamic range in $M_{\rm BH}$ covered (e.g., J.-H. Woo et al. 2015; V. N. Bennert et al. 2021) and/or the use of less precise single-epoch $M_{\rm BH}$ estimators (e.g., C. J. Grier et al. 2013; T. Caglar et al. 2023), which increase ϵ by about 0.15 dex due to uncertain sample-averaged f factors (J.-H. Woo et al. 2015). For individual AGNs, the systematic uncertainties can be as large as ~0.4 dex (A. Pancoast et al. 2014). These $M_{\rm BH}$ measurement uncertainties alone may account for a significant portion of the intrinsic scatter in the $M_{\rm BH}$–σ relation reported in the literature. Moreover, systematic uncertainties from the host-galaxy side may introduce scatter to the $M_{\rm BH}$–σ relation. Various apertures have been used for measuring σ in quiescent galaxies, such as $R_{\rm eff}/8$ (L. Ferrarese & D. Merritt 2000), $R_{\rm eff}/2$ (e.g., J. Kormendy & L. C. Ho 2013), and $R_{\rm eff}$ (e.g., K. Gültekin et al. 2009). For AGNs, the situation is even worse, as aperture size is often ignored (with the exception of, e.g., V. N. Bennert et al. 2015; M. Batiste et al. 2017b; J. Molina et al. 2024). While there is no physical motivation for which spatial scales σ should correlate the closest with $M_{\rm BH}$, the choice of the right aperture size is crucial: In our sample, we were able to resolve kinematic substructures, such as fast-rotating disks (see Figure 4, NGC 3227, NGC 7469), counter-rotating disks (e.g., Mrk 1310), or circumnuclear spirals (e.g., Mrk 1044). Such complex kinematic substructures will affect σ measurements, depending on what aperture size is used.

5.3.6. Optimal Aperture for Minimizing Intrinsic Scatter

A generally applicable approach is needed to to define $\sigma_\star$ consistently across different morphological components. We propose using an aperture size in units of the galaxy effective radius, $R_{\rm eff}^{\rm gal}$, to address varying spatial resolution and morphological complexity, thereby enhancing the consistency of the $M_{\rm BH}$–σ relation. This straightforward and self-consistent definition aims to minimize scatter in the $M_{\rm BH}$–σ relation. Figure 9 shows the behavior of the best-fit parameters to the $M_{\rm BH}$–$\sigma_{\rm ap}$ relation of AGNs hosted by LTGs, as a function of varying aperture size $R_{\rm ap}$. Overall, we observe that the $M_{\rm BH}$–σ relation becomes marginally tighter for smaller aperture sizes below $R_{\rm ap}/R_{\rm eff}^{\rm gal}$. This may be caused by apertures larger than $R_{\rm ap}^{\rm gal}$; the larger-scale outskirts of galaxies are decoupled from the galaxy-intrinsic processes that shape the $M_{\rm BH}$–σ relation. For instance, galaxy interactions, mergers, or stellar accretion streams might affect $\sigma_{\rm ap}$ at large $R_{\rm ap} > R_{\rm eff}^{\rm gal}$ of individual galaxies, increasing the scatter of the relation. Within $R_{\rm eff}^{\rm gal}$, the intrinsic scatter ϵ decreases mildly with decreasing $R_{\rm ap}$. Overall, it stays consistent with $\epsilon = 0.47$ dex, the typical scatter of the relation on galaxy scales (see row (iii) of Table 5). For the $M_{\rm BH}$–$M_{\rm gal,dyn}$ relation, this behavior is slightly more pronounced: the $M_{\rm BH}$–$M_{\rm bulge,dyn}$ relation shows the more significant slope and has a smaller intrinsic scatter compared to the $M_{\rm BH}$–$M_{\rm gal,dyn}$ relation (see columns (xii) and (xiii) of Table 5), suggesting that the bulge represents the spatial scale on which the correlations are the tightest. However, for many AGNs, stellar kinematics near the galaxy center are often missing, reducing sample completeness from 1 at $R_{\rm eff}^{\rm gal}$ to about 0.5 at $\langle R_{\rm eff}^{\rm bulge} \rangle$. As $R_{\rm ap}$ decreases, the intercept α varies significantly, indicating substantial effects from sample downselection. Specifically, smaller apertures preferentially exclude distant galaxies, leading to an overrepresentation of lower-luminosity AGNs hosted by less massive LTGs. We therefore caution interpreting α and β on scales of the bulge as the "best" parameters for $M_{\rm BH}$–σ, as this AGN subsample is likely biased.

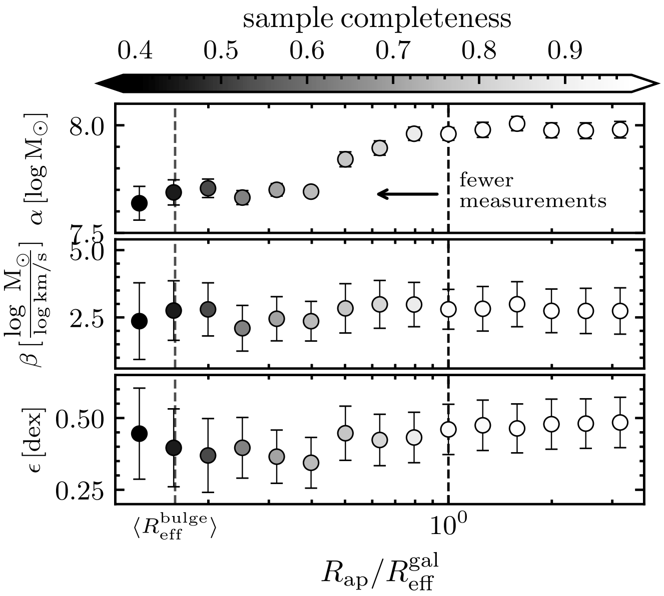

Figure 9. Parameters of the best-fit observed $M_{\rm BH}$–$\sigma_{\rm ap}$ relation of AGNs hosted by LTGs, as a function of aperture size $R_{\rm ap}$. Data points are color coded by the fraction of AGNs for which we can robustly measure $\sigma_{\rm ap}$, which decreases with decreasing $R_{\rm ap}$: while $\sigma_{\rm ap}$ is constrained for the full the sample at $R_{\rm eff}^{\rm gal}$, measuring σ close to the galaxy center becomes increasingly more challenging for more distant and luminous AGNs. The three panels show the parameters of the best-fit $M_{\rm BH}$–$\sigma_{\rm ap}$ model parameters to the data, as a function of aperture size. The intrinsic scatter ϵ reaches its global minimum close to $R_{\rm eff}^{\rm bulge}$, also reflected by the lowest ϵ of the corresponding scaling relation in row (v) of Table 5. This $M_{\rm BH}$–σ correlation is tightest on scales of the bulge.

5.4. Controlling Selection Effects

T. R. Lauer et al. (2007) pointed out that flux-limited AGN samples are biased toward overmassive BHs compared to local samples of quiescent galaxies. This introduces a bias because overmassive BHs are preferentially selected due to the intrinsic scatter of the scaling relations (see also C. Y. Peng 2007; T. Treu et al. 2007). As such, selection effects can significantly impact BH mass scaling relations if not properly accounted for. In principle, these biases can be corrected if the selection function is well defined and based solely on AGN parameters (X. Ding et al. 2020, 2023), or if it can be statistically modeled using simple assumptions (e.g., J. Li et al. 2021). For AGNs, the biases in the $M_{\rm BH}$–σ relation are dominated by two criteria: (i) measuring a reliable $\sigma_\star$, which is often drowned by the bright AGN emission, and (ii) the narrow $M_{\rm BH}$ range, limited by the detection of low-luminosity AGNs and scarcity of luminous nearby AGNs. In Section 4.4.1, we have directly addressed (i) by using a standardized recipe for consistently measuring σ in AGN host galaxies. Regarding (ii), we note that the selection of the AGNs in our sample is purely based on an $M_{\rm BH}$ measurement technique, with the vast majority (40/44) having been monitored in RM campaigns. The selection for such RM campaigns is, to first order, blind to host-galaxy properties and purely based on AGN properties. As a prerequisite for measuring robust time lags, AGNs must exhibit a broad line that shows sufficient BLR flux variability as well as continuum variability on the relevant timescales. Compared to higher-mass BHs, lower-mass BHs are more likely to be active and thus included in optically selected type 1 AGN samples (A. Schulze & L. Wisotzki 2011, although not in X-ray selected AGN samples; see, e.g., F. Zou et al. 2024). This "active fraction bias" is inherent to the RM AGN sample. Additionally, low-luminosity AGNs with weak broad lines (J. E. Greene & L. C. Ho 2007; I. V. Chilingarian et al. 2018) are typically excluded from RM campaigns, introducing an additional luminosity bias. As a result, the $M_{\rm BH}$ distribution is truncated at both low and high $M_{\rm BH}$ (A. Schulze & L. Wisotzki 2011), reducing the dynamic range in the $M_{\rm BH}$–$\sigma_\star$ plane and skewing the relation.

5.4.1. Matching the M_{BH} Distribution

These selection effects can be addressed by matching $M_{\rm BH}$ distributions between AGN and quiescent samples, assuming that differences in $M_{\rm BH}$ distributions are the primary driver of varying scaling relations. We correct it by matching the $M_{\rm BH}$ distribution function of the quiescent population to that of our AGN sample, following the empirical method outlined by J.-H. Woo et al. (2013). For the implementation, we use a Monte Carlo approach: for each $M_{\rm BH}$ in the quiescent galaxy sample, we assign a random $\sigma_\star$ chosen from AGNs that have the same $M_{\rm BH}$ (within a ±0.15 dex bin, the typical uncertainty of $M_{\rm BH}$). By construction, the resulting mock quiescent sample follows the same $M_{\rm BH}$ distribution as the AGN sample. We repeat this step for 1000 Monte Carlo samples, and fit the $M_{\rm BH}$–$\sigma_\star$ relation for each, using the method described in Section 5.3. The left panel of Figure 10 shows the results of this experiment. Indeed, when the $M_{\rm BH}$ of quiescent galaxies is resampled to the AGNs' distribution (gray contours), their relation (gray shades) is flattened, and the best-fit intercept $\alpha = 8.02 \pm 0.12$ slope $\beta = 2.38 \pm 0.61$ are consistent with the relation recovered from directly fitting the AGN (i.e., the values in row (ii) of Table 5).

By construction, the inverse experiment recovers the AGN $M_{\rm BH}$–$\sigma_{\rm ap}^{\rm bulge}$ relation for AGNs if they followed the same $M_{\rm BH}$ distribution as the quiescent KH13 galaxy sample. We refer to this quiescent-matched relation, highlighted in Table 5, as the *corrected* scaling relation of AGNs. The top-right panel of Figure 10 illustrates that, after the $M_{\rm BH}$ resampling, the AGNs (colored contours) follow the same $M_{\rm BH}$–$\sigma_{\rm ap}^{\rm bulge}$ (colored stripes) as quiescent galaxies (gray stripes). The posterior distribution of the best-fit parameters in Figure 11 confirms that the offsets in α and β are statistically insignificant (below the 1σ confidence level). At our measurement uncertainty, the scaling relations for both populations are indistinguishable. Thus, the observed differences in the $M_{\rm BH}$–$\sigma_\star$ relation between AGNs and quiescent galaxies can be attributed to differing $M_{\rm BH}$ distributions alone.

The relation of $M_{\rm BH}$ with dynamical bulge mass, shown in the bottom panels of Figure 10, confirms what we find for the $M_{\rm BH}$–σ relation: AGNs and quiescent galaxies form their own scaling relations that fall in complementary parts of the $M_{\rm BH}$–$M_{\rm bulge,dyn}$ plane. Fitting the observed $M_{\rm BH}$–$M_{\rm bulge,dyn}$ of AGNs returns a relation with a shallower slope compared to that of quiescent galaxies. After matching their $M_{\rm BH}$ distributions, the relations are indistinguishable, suggesting that both populations share the same underlying scaling relation.

We note that the RM AGN sample might still contain additional biases, which were not considered here. Their BLR geometry might sample only a fraction of the parameter space (G. T. Richards et al. 2011). From the host-galaxy side, BLR variability may be coupled to gas-transport processes on host-galaxy scales, which could entail a secondary correlation with galaxy interactions (J. E. Barnes & L. Hernquist 1996), or secular processes triggered by, e.g., bars (e.g., S. García-Burillo et al. 2005). Furthermore, is worth also noting that the quiescent sample suffers from selection biases, as pointed out by, e.g., M. Bernardi et al. (2007) and R. C. E. van den Bosch (2016): host galaxies with dynamically measured $M_{\rm BH}$ tend to have higher σ compared to ETGs of the same luminosity, which may artificially increase the normalization $M_{\rm BH}$–σ relation by a factor of ∼3 (see F. Shankar et al. 2016, 2020; but also see J. Kormendy 2020).

5.5. The Virial Factor f

The classical approach for measuring a sample-average virial factor *f* involves matching the $M_{\rm BH}$–σ relation of RM AGNs to that of quiescent galaxies. This is usually done by fitting the VP–σ relation with a fixed slope and determining the sample-average virial factor via the difference of the intercepts $\log f = \alpha_{\rm qui} - \alpha_{\rm AGN}$. However, this step implicitly assumes that AGNs and quiescent galaxies follow the same $M_{\rm BH}$–σ relation, which so far has little empirical foundation. Furthermore, the matching is prone to systematic uncertainties introduced by different selection functions between AGN and quiescent galaxy samples; $\langle f \rangle$ can vary by 0.3 dex depending on what quiescent galaxy sample is used as a reference (L. C. Ho & M. Kim 2014). In addition, individual *f* factors vary by one order of magnitude across the sample, limiting the precision of this approach.

To test the implicit assumptions and reduce systematic uncertainties, we used the independently measured individual *f* factors from `CARAMEL` modeling. The sample-average $\langle f \rangle$ can be derived from comparing the intercept between active and inactive galaxies. We fit the $M_{\rm BH}$–σ relation for the CARAMEL sample, this time fixing the slope to that of quiescent galaxies due to the limited dynamic range in $M_{\rm BH}$ ($\alpha_{\rm qui} = 4.53 \pm 0.32$; see Section 5.2). This step is justified, since we demonstrated that both share the same underlying relations (see Section 5.4). As opposed to the classical approach, the average of the dynamically measured values, $\langle \log f_{\rm dyn}, \rangle$, must be added to account for the sample-average virial factor that is already incorporated in the AGNs' $M_{\rm BH}$ (i.e., is already included in $\alpha_{\rm qui}^{\rm AGN}$):

$$\langle \log f \rangle = \alpha^{\rm qui} - \alpha_{\rm dyn}^{\rm AGN} + \langle \log f_{\rm dyn} \rangle. \tag{7}$$

Fitting the AGNs' observed $M_{\rm BH}$–$\sigma_{\rm ap}^{\rm bulge}$ relation with the slope fixed to the KH13 relation yields $\alpha_{\rm dyn}^{\rm AGN} = 8.20 \pm 0.11$ and $\langle \log f \rangle = 0.65 \pm 0.18$. This result closely matches

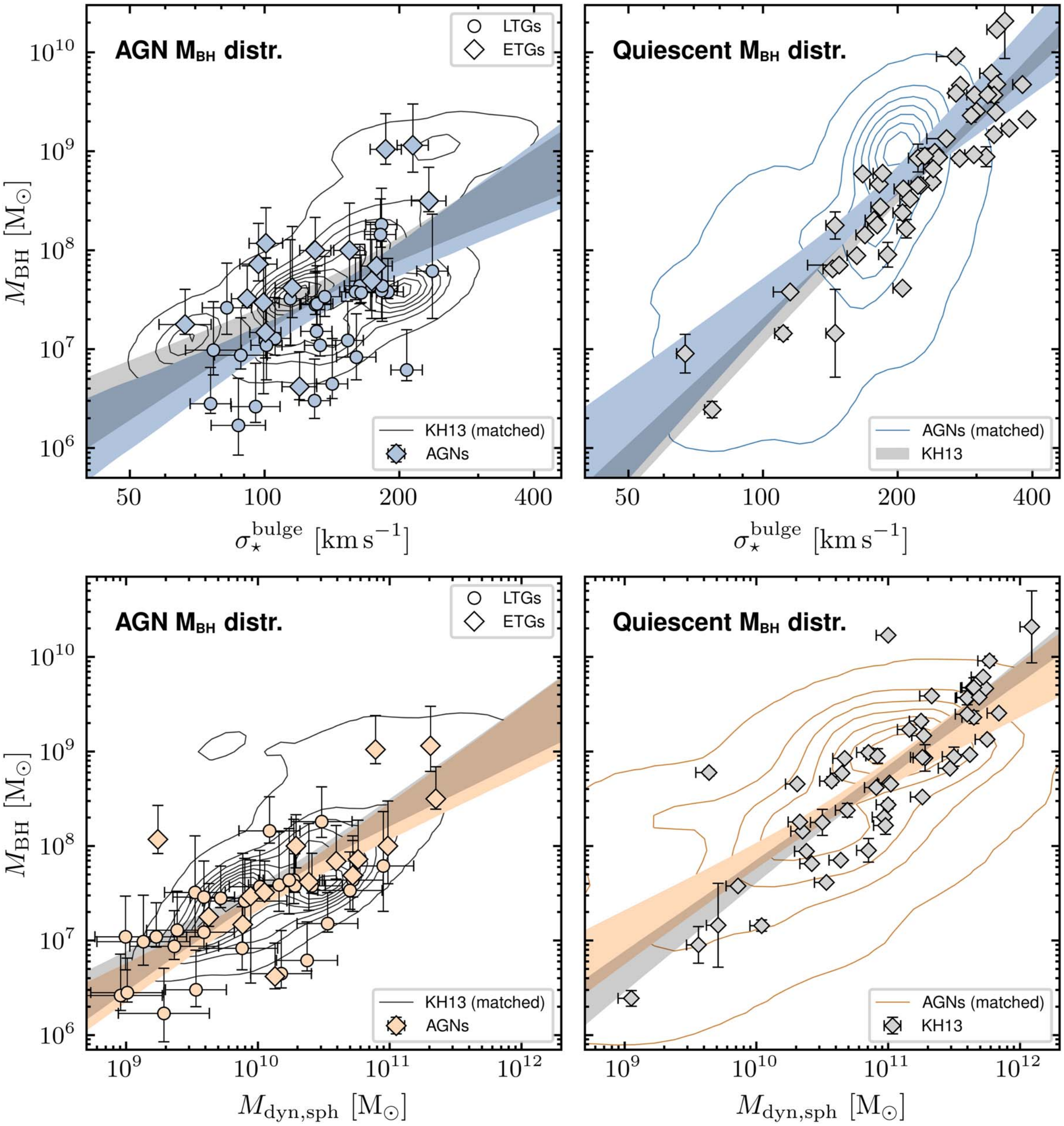

Figure 10. M_{BH}–host-galaxy scaling relations of AGNs and quiescent galaxies. Top left: colored data points show AGNs hosted by LTGs (circles) and ETGs (squares), with the best-fit observed relation shown as a blue stripe (corresponding to row (ii) in Table 5). For AGNs, no clear distinction between the relations of ETGs and LTGs is observed. The gray contours show the KH13 sample that is resampled in M_{BH} to match the AGNs' M_{BH} distribution (see Section 5.4), with the fitted relations shown as a shaded gray stripe. The relation of the M_{BH}-matched quiescent sample agrees with the AGNs' observed relation and is significantly flatter than the observed relation of quiescent galaxies shown in the right panel. Top right: after empirically matching the M_{BH} distribution of AGNs (blue contours) to that of quiescent galaxies (KH13 sample, gray data points), both fall into the same region of the M_{BH}–$\sigma_\star$ plane. The best-fit relations of AGNs are shown as blue and gray stripes, and correspond to the relations in rows (v) and (i), respectively, in Table 5. Bottom left: the same for the M_{BH}–$M_{bulge,dyn}$ relation, with the observed AGN listed in row (xii) of Table 5. After matching the M_{BH} distribution, the relations of AGNs and quiescent galaxies are indistinguishable. Bottom right: same for matching the AGNs to the distribution of quiescent galaxies. The M_{BH} and $M_{bulge,dyn}$ relation correspond to row (xiv) of Table 5.

$\langle \log f \rangle = 0.65 \pm 0.12$, the value obtained from applying the classical method to the RM AGN sample (J.-H. Woo et al. 2015). It also aligns well with the average of individual f factors from dynamically modeling their BLR lags, $\langle \log f_{dyn} \rangle = 0.66 \pm 0.07$ (column (11) of Table 1). We conclude that the classical approach of determining the sample-average virial factor from matching the M_{BH}–σ relation of RM AGNs agrees with the independent measurements of M_{BH} in AGNs. Importantly, neither do we find significant dependencies of the sample-average f on host-galaxy morphology (as opposed to, e.g., L. C. Ho & M. Kim 2014), nor do we observe such a dependency among the f_{dyn} (see L. Villafaña et al. 2023 for more discussion).

5.6. Uniform M_{BH}–Host-galaxy Scaling Relations of Active and Quiescent Galaxies: Consequences

AGNs represent a special stage of BH evolution where the ongoing gas accretion may significantly contribute to grow the SMBH. However, AGN lifetime and the associated contribution to SMBH growth are only scarcely constrained, so that it

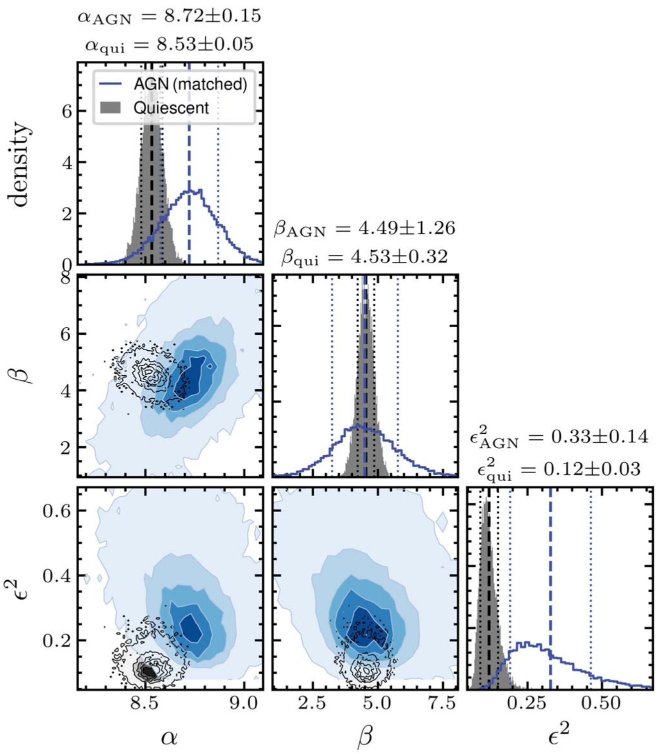

Figure 11. Corner plot of the free parameters of the linear $M_{\rm BH}$–σ model after matching the $M_{\rm BH}$ distribution. The posterior distributions of the quiescent population from KH13 are shown as black lines/contours, and the AGNs from our sample are shown with blue colors. The intercept α and both populations are not significantly different, although associated with larger uncertainties for AGNs. This indicates that quiescent galaxies and AGNs follow similar intrinsic $M_{\rm BH}$–σ relations.

is not clear how this should affect the AGN $M_{\rm BH}$ scaling relations. Regardless, there has been no independent and conclusive observational evidence for whether AGNs follow the same $M_{\rm BH}$–host-galaxy scaling relations as quiescent galaxies. While J.-H. Woo et al. (2013) demonstrated that selection effects can account for differences in slopes, our independent $M_{\rm BH}$ measurements reveal for the first time that both the slope β and intercept α of the scaling relations for AGNs and quiescent galaxies are the same, indicating that both populations share the same underlying $M_{\rm BH}$ scaling relation. This suggests, and we have explicitly tested, that matching the $M_{\rm BH}$–σ relation of AGNs with that of quiescent galaxies is justified for constraining the sample-average virial factor *f*. In other words, our results reinforce previous calibrations of *f* and individual measurements of $f_{\rm dyn}$ from dynamical modeling the BLR lags. By covering a larger dynamic range in both host galaxies and BHs, our results also support the use of the single-epoch method for estimating $M_{\rm BH}$ across the explored parameter range, up to $\log(M_{\rm BH}/M_\odot) \sim 10^{8.5}$.

6. Summary

After more than two decades of study, the $M_{\rm BH}$ scaling relations have emerged as essential probes of the coevolution between SMBHs and their host galaxies. For AGNs, state-of-the-art observational and computational techniques have enabled more precise measurements of $M_{\rm BH}$ and $\sigma_\star$ than were previously possible. In this work, we used spatially resolved stellar kinematics to calibrate the $M_{\rm BH}$–$\sigma_\star$ relation of the local AGN population. For a sample of 44 AGNs, the majority of which have precise and independent $M_{\rm BH}$ measurements from dynamical modeling, we presented IFU data from Keck/KCWI, VLT/MUSE, and VLT/VIMOS. We tested different AGN deblending and analysis techniques that are required to precisely trace the spatially resolved stellar kinematics. Based on HST imaging data, we spatially resolved σ across different galaxy morphological components, and studied dependencies of the scaling relation $M_{\rm BH}$ on morphology and aperture size. Our key findings can be summarized as follows:

1. We find mild evidence that the $M_{\rm BH}$–$\sigma_\star$ correlation of AGNs hosted by LTGs is tightest if the kinematics are measured on scales of the galaxy bulge.
2. Rotational broadening from the galaxy disk introduces scatter in the $M_{\rm BH}$–host-galaxy relations of AGNs hosted by LTGs. Comparative studies based on higher-redshift AGNs hosted by disk galaxies can use the derived aperture-correction method to statistically infer the underlying $M_{\rm BH}$–$\sigma_\star$ scaling relation.
3. After removing the contribution from disk rotation, LTGs follow an $M_{\rm BH}$–σ relation that is similar to that of quiescent galaxies, but offset to lower $\sigma_\star$ by 0.2 dex. This suggests that the dynamically hot disk component of LTGs does coevolve with the SMBH.
4. The $M_{\rm BH}$–$\sigma_\star$ relation in AGNs is robust, regardless of whether the host galaxies have late-type or early-type morphologies. The intrinsic scatter is primarily driven by galaxy-to-galaxy variations. However, further constraining this scatter is challenging due to the scarcity of AGNs with dynamically measured $M_{\rm BH} > 10^8$, $M_\odot$, and the fact that σ in such luminous AGNs can only be marginally spatially resolved.
5. The observed flattening of both $M_{\rm BH}$–σ and $M_{\rm BH}$–$M_{\rm dyn}$ relations of AGNs is driven by selection biases that limit the $M_{\rm BH}$ dynamic range. We demonstrated for the first time that, after correcting for this effect, the slope *and* intercept of the underlying AGN scaling relations match those of quiescent galaxies. This suggests that, on average, the current AGN phase does not significantly grow $M_{\rm BH}$ compared to $M_{\rm BH}$ in quiescent galaxies.
6. The $M_{\rm BH}$ of our sample was determined independently of the virial factor. Thus, we present a self-consistent empirical calibration of $\langle f\rangle$ based on spatially resolved kinematics of type 1 AGNs. The derived value of $\log f = 0.65 \pm 0.18$ matches previous calibrations based on the classical RM AGN sample, as well as the average $\langle f\rangle$ determined from individually measured *f*. A robust understanding of the virial factor is essential for estimating $M_{\rm BH}$ measurements in the distant Universe via the single-epoch method.

Spatially resolving $\sigma_\star$ in AGNs is currently feasible only for the local AGN population, which we used in this study to provide the local reference of the $M_{\rm BH}$ scaling relations. It remains an important objective to identify the morphological components and spatial scales across which the $M_{\rm BH}$–$\sigma_\star$ relation of the quiescent population is the tightest. This can be best tested on nearby galaxies, for which a larger sample size, higher spatial resolution, and the lack of a bright AGN PSF make this analysis less sensitive to systematic uncertainties.

Acknowledgments

We thank the anonymous referee for their valuable comments that improved the quality of the paper. We thank

Rogemar A. Riffel for providing access to data that supported the development of this work. N.W. is a fellow of the International Max Planck Research School for Astronomy and Cosmic Physics at the University of Heidelberg (IMPRS-HD). This work is cofunded by the DFG under grant HU 1777/3-1. V.N.B. gratefully acknowledges assistance from the National Science Foundation (NSF) through grant AST-1909297. This work is based on observations with the NASA/ESA Hubble Space Telescope obtained from the Data Archive at the Space Telescope Science Institute, which is operated by the Association of Universities for Research in Astronomy, Incorporated, under NASA contract NAS5-26555. Support for Program number HST-GO 17103 (PI: Bennert) and HST-AR 17063 (PI: Bennert) was provided through a grant from the STScI under NASA contract NAS5-26555. Note that findings and conclusions do not necessarily represent views of the NSF. V.N.B. is also grateful for funding provided by a NASA-ADAP grant (grant No. 80NSSC19K1016). T.T. acknowledges support by the National Science Foundation through grant NSF-AST-1907208. V.U. acknowledges funding support from NSF Astronomy and Astrophysics Research grant No. AST-2408820, NASA Astrophysics Data Analysis Program (ADAP) grant No. 80NSSC23K0750, and STScI grant Nos. HST-GO-17285.001-A and JWST-GO-01717.001-A. Some of the data presented herein were obtained at Keck Observatory, which is a private 501(c)3 nonprofit organization operated as a scientific partnership among the California Institute of Technology, the University of California, and the National Aeronautics and Space Administration. The Observatory was made possible by the generous financial support of the W. M. Keck Foundation. The authors wish to recognize and acknowledge the very significant cultural role and reverence that the summit of Maunakea has always had within the Native Hawaiian community. We are most fortunate to have the opportunity to conduct observations from this mountain.

Facilities: Keck:II (KCWI), VLT:Yepun (MUSE), VLT: Melipal (VIMOS), HST (ACS, WFCP2, WFC3).

Software: `Astropy` (Astropy Collaboration et al. 2013, 2018), `SciPy` (P. Virtanen et al. 2020), `Lenstronomy` (S. Birrer & A. Amara 2018), `PyParadise` (B. Husemann et al. 2016a), `pPXF` (M. Cappellari & Y. Copin 2003; M. Cappellari 2017), `VorBin` (M. Cappellari & Y. Copin 2003), `CubePCA` (B. Husemann et al. 2022), `BADASS` (R. O. Sexton et al. 2021), `QDeblend`^{3D} (B. Husemann et al. 2013, 2014), MUSE data processing pipeline (P. M. Weilbacher et al. 2020), `LinMix` (B. C. Kelly 2007).

Appendix A
AGN Spectral Fitting

In order to estimate the AGN parameters $M_{\rm BH}$, $L_{\rm bol}$, and $\lambda_{\rm Edd}$, as discussed in Section 4.2, we model the AGN spectrum in the Hβ–[O III] wavelength region. As a first step, we correct the Galactic foreground extinction, which can significantly reduce the observed flux and alter the overall shape of the spectra recorded for our extragalactic targets. We correct all KCWI, MUSE, and VIMOS data cubes for Galactic extinction by dividing with the J. A. Cardelli et al. (1989) Milky Way optical extinction curve, before fitting the AGN spectra. The extinction curve is scaled to the line-of-sight *V*-band extinction as reported by NED, which is based on SDSS stars (E. F. Schlafly & D. P. Finkbeiner 2011).

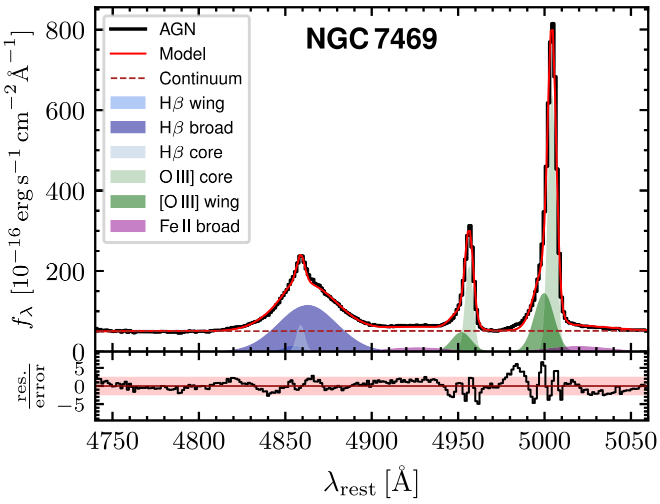

Figure 12. Example of the AGN spectral modeling for the case of NGC 7469. The modeled wavelength range is limited to the rest-frame wavelength range 4750 Å–5100 Å covering the prominent Hβ and [O III] emission lines. The spectrum with the full best-fit model and various line components for the BLR and the narrow and core component for Hβ and [O III] are individually shown with different line styles and colors. The residual spectrum and the 3σ limiting band are shown in the lower panel.

To get a pure AGN spectrum free from host emission, we collapse the host-deblended AGN data cube along the spatial axes. We then subtract the best-fit stellar continuum as determined via `pPXF` (see Section 4.3). For a consistent analysis between the data sets that cover different wavelength ranges, we restrict the spectral fitting to the common rest-frame wavelength range 4750 Å to 5100 Å. To describe the AGN power-law continuum in this narrow wavelength range, we adopt a linear pseudocontinuum. For the strong emission lines Hβ and [O III], we use a superposition of broad and narrow Gaussian line profiles: two broad components for the Hβ line and two broad Fe II $\lambda\lambda$ 4923,5018 lines are sufficient to describe the spectral variations across the sample. In addition to the narrow components for each [O III] and Hβ, we often require a wing component to reproduce the typical asymmetry of those lines in AGN (J. E. Greene & L. C. Ho 2005b; J. R. Mullaney et al. 2013). We kinematically couple the broad narrow and wing components to each other and tie the [O III] doublet line ratio to its theoretical value of 3 (P. J. Storey & C. J. Zeippen 2000) and that of Fe II components to their empirical ratio of 0.81. With these constraints, we reduce the number of free parameters and increase the robustness of the fit.

An example of the modeling is shown in Figure 12. We list the corresponding line fluxes of the broad Hβ and Fe II lines together with their line widths as well as the total [O III] flux in Table 6. The corresponding errors are estimated from Monte Carlo sampling, plus an addition of 10% systematic uncertainty introduced from the AGN host deblending and continuum-subtraction process.

Table 6
AGN Parameters Estimated from Fitting the AGN Spectrum

AGN Name (1)	$\sigma_{\mathrm{H}\beta}$ (km s^{-1}) (2)	f_λ(5100 Å) (10^{-15} erg s^{-1} cm^{-2} Å^{-1}) (3)	L_{bol} (10^{43} erg s^{-1}) (4)	log λ_{Edd} (5)
NGC 3227	1656 ± 83	7.7 ± 0.4	1.23 ± 0.07	−2.0 ± 0.2
NGC 6814	1466 ± 73	2.3 ± 0.3	0.69 ± 0.09	−1.7 ± 0.3
NGC 4593	1655 ± 83	2 ± 0.4	1.6 ± 0.3	−1.6 ± 0.4
NGC 3783	2170 ± 110	10.2 ± 0.2	10.9 ± 0.2	−1.5 ± 0.2
NGC 2617	2100 ± 110	1.13 ± 0.08	2.6 ± 0.2	−2.2 ± 0.2
IC 4329 A	2860 ± 430	2.08 ± 0.09	5.4 ± 0.2	−2.0 ± 0.2
Mrk 1044	805 ± 40	3.2 ± 0.2	9.6 ± 0.7	−0.6 ± 0.2
NGC 5548	3500 ± 170	6.8 ± 0.2	20.7 ± 0.7	−1.4 ± 0.2
NGC 7469	1046 ± 52	5.2 ± 0.4	16.4 ± 1.2	−1.1 ± 0.3
Mrk 1310	1360 ± 180	0.16 ± 0.03	0.7 ± 0.1	−2.7 ± 0.4
Mrk 1239	1093 ± 55	3.3 ± 0.2	14.7 ± 0.7	−1.4 ± 0.2
Arp 151	1170 ± 350	0.46 ± 0.06	2.3 ± 0.3	−1.4 ± 0.3
Mrk 50	1992 ± 100	1.16 ± 0.1	7.3 ± 0.6	−1.7 ± 0.3
Mrk 335	1800 ± 200	2 ± 0.3	15.2 ± 2.4	−1.2 ± 0.4
Mrk 590	3580 ± 180	1.39 ± 0.07	11 ± 0.5	−1.6 ± 0.2
SBS 1116+583A	1845 ± 92	0.28 ± 0.03	2.6 ± 0.3	−1.7 ± 0.3
Zw 229-015	1386 ± 69	0.65 ± 0.02	5.9 ± 0.2	−1.3 ± 0.2
Mrk 279	2010 ± 100	3.24 ± 0.1	35.3 ± 1.1	−1.1 ± 0.2
Ark 120	1200 ± 60	4.11 ± 0.06	51.8 ± 0.8	−1.6 ± 0.2
3C 120	1658 ± 83	13.1 ± 0.1	168.1 ± 1.9	−0.7 ± 0.2
MCG +04-22-042	1410 ± 70	0.68 ± 0.03	8.9 ± 0.4	−1.7 ± 0.2
Mrk 1511	1906 ± 95	0.22 ± 0.01	3 ± 0.2	−1.7 ± 0.2
PG 1310–108	1589 ± 79	1.31 ± 0.04	18.1 ± 0.6	−0.3 ± 0.2
Mrk 509	2060 ± 100	13 ± 0.1	185 ± 1.8	−0.8 ± 0.2
Mrk 110	1797 ± 90	1.6 ± 0.02	23.8 ± 0.3	−0.9 ± 0.2
Mrk 1392	1983 ± 99	0.65 ± 0.02	9.9 ± 0.3	−2.3 ± 0.2
Mrk 841	2030 ± 100	3.03 ± 0.05	47.6 ± 0.8	−1.0 ± 0.2
Zw 535-012	1916 ± 96	1.6 ± 0.03	43.7 ± 0.8	−1.0 ± 0.2
Mrk 141	2780 ± 140	0.89 ± 0.09	18.5 ± 1.8	−1.3 ± 0.3
RBS 1303	1249 ± 62	2.6 ± 0.08	54.1 ± 1.7	−0.2 ± 0.2
Mrk 1048	2080 ± 100	8.4 ± 0.7	183 ± 15	−0.6 ± 0.3
Mrk 142	1291 ± 65	0.7 ± 0.02	16.8 ± 0.4	−0.1 ± 0.2
RXJ 2044.0+2833	898 ± 45	2.49 ± 0.04	75 ± 1.3	−0.3 ± 0.2
IRAS 09149–6206	2310 ± 120	27.7 ± 1.7	1110 ± 67	−0.1 ± 0.2
PG 2130+099	1690 ± 510	3.85 ± 0.08	194.1 ± 4.1	0.3 ± 0.2
NPM1G +27.0587	1228 ± 61	1.88 ± 0.05	88.8 ± 2.3	−0.8 ± 0.2
RBS 1917	1390 ± 70	1.14 ± 0.08	59.6 ± 4.1	−0.4 ± 0.2
PG 2209+184	1908 ± 95	0.56 ± 0.02	34.2 ± 1.3	−1.1 ± 0.2
PG 1211+143	1736 ± 87	4.5 ± 0.7	375 ± 54	−0.6 ± 0.4
PG 1426+015	2630 ± 140	4.29 ± 0.08	402.8 ± 7.9	−1.5 ± 0.2
Mrk 1501	1870 ± 170	1.08 ± 0.04	103.5 ± 3.4	−0.9 ± 0.2
PG 1617+175	2030 ± 140	2.67 ± 0.08	439 ± 13	−0.1 ± 0.2
PG 0026+129	921 ± 92	1.7 ± 0.2	500 ± 60	−0.9 ± 0.3
3C 273	2120 ± 110	20.9 ± 1.2	7300 ± 420	−0.3 ± 0.2

Note. AGNs are listed in order of increasing redshift (as in Table 1). Column (1): AGN name. Column (2): line dispersion of the Hβ BLR component. Column (3): AGN continuum spectral flux density at 5100 Å. Column (4): approximate AGN bolometric luminosity from using a bolometric correction factor of 10. Column (5): Eddington ratio $\lambda_{\mathrm{Edd}}=L_{\mathrm{bol}}/L_{\mathrm{Edd}}$.

Appendix B
The Importance of AGN Host Deblending

Since close to the galaxy center the AGN is typically orders of magnitude brighter than the host-galaxy stellar continuum, the AGN emission blends the kinematic diagnostic features, making an accurate extraction of host-galaxy parameters challenging. This can drastically affect the kinematics measured for any extended host-galaxy component. While this is a well-known problem for tracing ionized gas emission lines of outflows and the extended narrow-line region (e.g., B. Husemann et al. 2016b; M. Villar-Martin et al. 2016), here we demonstrate the impact of the AGN emission on extracting the host-galaxy stellar kinematics.

The AGN spectrum can be described by a power-law spectrum, with an additional contribution from the BLR clouds. Depending on the observational setup, atmospheric conditions, AGN/host luminosity ratio, and AGN spectral classification, the AGN outshines the stellar continuum within the central $0\farcs4$ to $\sim6\farcs0$, especially for some luminous AGNs, e.g., the narrow-line Seyfert 1 galaxies Mrk 335 and Mrk 1044, with strong Fe II blending the Mg Ib wavelength region. In these cases, an accurate extraction of the stellar kinematics close to their nuclei is limited by the contrast between the AGN emission and the

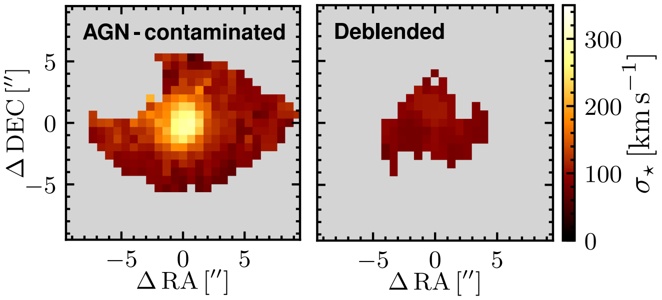

Figure 13. AGN deblending impacts the extraction of σ in Mrk 110. The left panel shows the spatially resolved $\sigma_{\rm spat}$ of Mrk 110 as extracted from the AGN-contaminated cube (left panel). Its profile shows a steep rise toward the galaxy nucleus, caused by the prominent Fe II broad emission lines blending with important σ diagnostic lines. After carefully subtracting the bright AGN emission, the measured central $\sigma_{\rm spat}$ is smaller by a factor of 3 (right panel).

host galaxy, together with the accuracy by which the PSF can be modeled and subtracted.

There are two approaches to handle the AGN contamination: (i) the AGN spectrum can be included in the spectral synthesis modeling, as performed by R. Remigio et al. (2024, in preparation), for example, who use the package `BADASS` for analyzing a subsample of our AGNs. While this approach is free of parameters, such as, e.g., the host-galaxy surface brightness profile, it requires a sophisticated treatment of the kinematic coupling between the spectral components, plus a well-considered choice of the starting parameters. (ii) We make the well-justified assumption that the broad lines exclusively originate from the spatially unresolved BLR. The package `QDeblend`$^{\rm 3D}$ uses this to extract an empirical PSF, whose subtraction is described in Section 3.1.4.

Figure 13 shows the results for σ from fitting the stellar continuum emission of Mrk 110 with `pPXF`, before and after the PSF subtraction with `QDeblend`$^{\rm 3D}$. In the AGN-contaminated case, i.e., before PSF subtraction, σ within the central 3″ reaches a central value of 295 ± 15 km s^{-1}. These formal errors drastically underestimate the systematic offset that arises from the AGN contamination: after the AGN host deblending, the spectral synthesis modeling of the faint host-galaxy signal results in a flat radial profile, where the central spaxel at the AGN location has $\sigma_{\rm spat} = 103 \pm 4$ km s^{-1}. This value is consistent with the 95 ± 8 km s^{-1} reported by L. Ferrarese et al. (2001), which were measured from CaT in a 2″ × 4″ long-slit aperture, which is less affected by AGN contamination. We note that Mrk 110 represents an extreme case, where the AGN contamination offsets the central σ by a factor of 3. However, within the bulge effective radii $R_{\rm eff}^{\rm bulge}$, we observe an average increase of 30% when measuring σ after not properly subtracting the AGN emission.

Appendix C
Spatially Resolved versus Aperture-integrated σ

In Section 4.4.1, we have defined two methods for measuring the stellar velocity dispersion: the dispersion measured from aperture-integrated $\sigma_{\rm ap}$ and the spatially resolved $\sigma_{\rm spat}$. As a consistency check, we reconstruct aperture-integrated kinematics from spatially resolved measurements in individual Voronoi cells. To achieve this, both contributions from ordered rotation $v_{\rm res}$ and chaotic motion $\sigma_{\rm res}$ must be considered, as has been done, e.g., for quiescent galaxies by J. Pinkney et al. (2003) and K. Gültekin et al. (2009), and for AGNs by V. N. Bennert et al. (2015). In our case of 2D kinematic fields, the surface area (i.e., number of spaxels) and the associated surface brightness of the host-galaxy stellar emission varies between different Voronoi cells. To derive consistent flux-weighted kinematics, the spatially resolved values must be weighted by the luminosity of the respective Voronoi cell. Thus, we reconstruct the aperture-integrated kinematics from spatially resolved measurements as

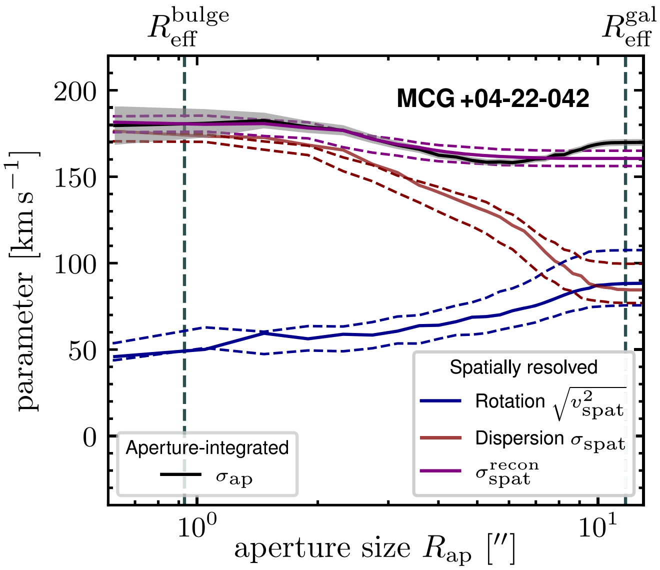

Figure 14. Comparing different methods to measure σ in MCG +04-22-042. The black line shows the aperture-integrated stellar velocity dispersion as a function of aperture size $R_{\rm ap}$, with the uncertainty indicated by gray shades. By integrating over the intensity-weighted contributions from the spatially resolved measurements of the rotational component $v_{\rm spat}$ and dispersion $\sigma_{\rm spat}$, we can reconstruct the aperture-integrated value across a large dynamic range in aperture sizes ($\sigma_{\rm spat}^{\rm recon}$, purple line).

$$(\sigma_{\rm ap}^{\rm recon})^2 = \frac{\int_0^{R_{\rm eff}} [\sigma^2_{\rm spat}(r) + v^2_{\rm spat}(r)] \cdot I(r) \cdot dr}{\int_0^{R_e} I(r) \cdot dr}, \qquad \text{(C1)}$$

with the surface brightness $I(r)$. In the case of reconstructing the kinematics of the bulge, $I(r) = I(R_e) \times \exp(-\kappa_n[(r/R_e)^{1/n} - 1])$ is described by a Sérsic profile, where the R_e is the bulge effective radius as measured from the photometry presented in V. N. Bennert et al. (2024, in preparation). This approach is equivalent to the prescription of the Nuker team (e.g., J. Pinkney et al. 2003; K. Gültekin et al. 2009), but for AGNs has only been applied to long-slit spectra (V. N. Bennert et al. 2015). From the ionized gas kinematics (see R. Remigio et al. 2024, in preparation), we noticed that $\sigma_{\rm ap}^{\rm recon}$ and $\sigma_{\rm ap}$ are not necessarily equal (also see KH13, supplementary material, for a discussion), although very complex emission-line profiles with high-velocity components are required for the differences to matter. Within the context of stellar kinematics where the gradients are small, we detect no significant differences between $\sigma_{\rm ap}^{\rm recon}$ and $\sigma_{\rm ap}$; MCG, +04-22-042 is an arbitrarily selected AGN for which we have coverage of $\sigma_{\rm spat}$ from scales below $R_{\rm eff}^{\rm bulge}$ to beyond $R_{\rm eff}^{\rm gal}$. In Figure 14, we show that, with increasing distance from the center, the relative contribution from the bulge component ($\sigma_{\rm spat}$) decreases, while the relative contribution of the ordered disk-like rotation ($v_{\rm spat}$) increases. When combined, the reconstructed radial profile of $\sigma_{\mathrm{ap}}^{\mathrm{recon}}$ matches that of σ_{ap} as directly measured from the coadded spectra corresponding to that aperture size. We have confirmed this behavior for LTGs in the sample, demonstrating the feasibility of disentangling the contributions from random orbital motions versus disk-like galaxy-scale rotation. Therefore, we conclude that our approach of inferring the M_{BH} scaling relation from rotation-corrected σ_{spat} is self-consistent (see Section 5.3).

However, we note that the spatial resolution in many data sets is too low to spatially resolve the bulge. In addition, the bright AGN emission often prevents measuring robust $\sigma_{\mathrm{spat}}^{\mathrm{bulge}}$ for 10 out of 38 LTGs. In these cases, the finite spatial resolution also impacts our ability to resolve the stellar kinematics on the relevant scales of the disk (a few arcseconds), so that rotational broadening likely contributes even to the spatially resolved quantity $\sigma_{\mathrm{spat}}^{\mathrm{gal}}$. As a result, disk rotation is poorly spatially resolved, so that the lower spatial resolution might bias σ_{spat} of individual AGNs toward higher values if the disk rotation is not resolved.

Appendix D
Stellar Kinematics from Different IFU Data Sets

A handful of AGNs in our sample (five of 44) have been observed with multiple optical IFU instruments, offering different field coverage, depth, spectral, and spatial resolution. We have demonstrated in Appendix B that the extraction of the stellar kinematics is limited by the accurate subtraction of the PSF, which is specific to each data set. For the multiply observed objects, observations taken under different conditions with different instruments allow us to obtain independent measurements of the host-galaxy stellar kinematics for consistency checks. MCG +04-22-042 is one of the AGNs that has been observed with both Keck/KCWI and VLT/MUSE. We processed each data set as outlined in Sections B and 4.3, and here compare the radial profiles of the aperture-integrated σ and the spatially resolved σ_{spat} measurements (described in Section 4.4.1). Figure 15 shows the comparison between the radial behavior of the spatially resolved kinematics extracted in MCG +04-22-042. Compared to the relatively small FOV of our KCWI setup ($16'' \times 20''$), the MUSE FOV covers a much larger fraction of the host galaxy. Within the overlapping field, the radial profile of σ_{spat} shows a steep decrease with increasing distance to the center. The radial profiles extracted from the two data sets agree within the uncertainties, out to the radius where the KCWI coverage stops. Different observing conditions and instrumental characteristics are reflected in the PSF width, $\theta_{\mathrm{FWHM}}^{\mathrm{MUSE}} = 1.2$, and $\theta_{\mathrm{FWHM}}^{\mathrm{KCWI}} = 1.8$. However, this difference does not significantly impact σ_{spat} on scales of the galaxy bulge $R_{\mathrm{eff}}^{\mathrm{bulge}}$; analyzing the MUSE and KCWI data sets yields $\sigma_{\mathrm{spat}}^{\mathrm{bulge}} = 173 \pm 5\ \mathrm{km/s}$ and $\sigma_{\mathrm{spat}}^{\mathrm{bulge}} = 169 \pm 6\ \mathrm{km/s}$, respectively.

For the remaining four objects (RBS 1303, NGC 5548, NGC 4593, PG 1310–108, all observed with VLT/VIMOS), we have carried out the same test for σ_{ap}, which is less sensitive to the differences between instrument characteristics. While the results generally agree with each other within the error margin, the depth and resolution of the MUSE and KCWI cubes are superior to the VIMOS data sets. We therefore adopted MUSE and KCWI for the analysis in the main part of this work.

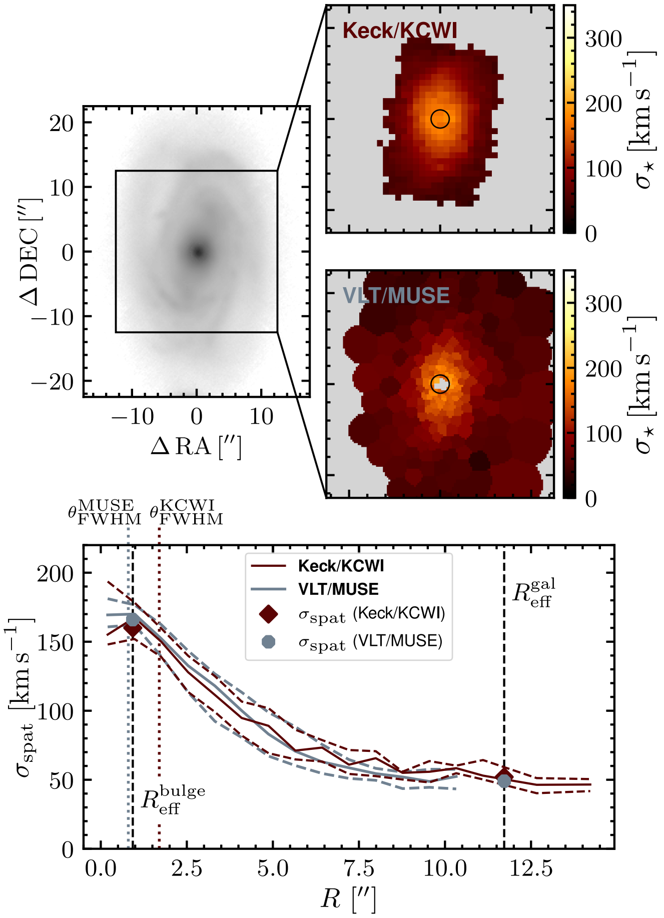

Figure 15. Comparing σ_{spat} in MCG +04-22-042, extracted from two different data sets. Top panels: the top-left panel shows the V-band AGN-subtracted continuum image of MCG +04-22-042, with σ_{spat} measured from the Keck/KCWI and VLT/MUSE data sets (top-right inset panels). While the field coverage of MUSE is superior, we can measure accurate σ_{spat} at the AGN location only in the KCWI data set. Bottom panels: the radial profiles of σ_{spat} measured from the two data sets are shown, together with the PSF FWHM θ_{FWHM} of the respective data set. Across the entire host galaxy, the spatially resolved radial profiles of σ_{spat} agree within the uncertainty, which confirms that our method is valid independent of the observational setup.

Appendix E
Stellar Kinematics from Different Diagnostic Features

In Figure 16, we compare how the choice of the wavelength range used for fitting the host-galaxy emission affects the extracted stellar kinematics (see Section 4.3). Specifically, we compare the kinematics obtained from the galaxy aperture-integrated spectra in the wavelength ranges 8400 Å8750 Å (CaT), 5100 Å–5700 Å (Mg Ib+Fe), and 4700 Å–5700 Å (“full”). We find that, in general, maximizing the wavelength range is favorable to increase the robustness of the parameters inferred through spectral synthesis modeling. However, the PSF subtraction required to remove the AGN emission can severely affect the faint host-galaxy stellar emission. As a result, spatially coadding spectra can introduce nonphysical artifacts in the spectra, especially near the galaxy nucleus, severely impacting the measured stellar kinematics. This effect is pronounced in two of the brightest AGNs, PG 1617+175 and PG 0026+129, where the choice of wavelength range can lead to systematic differences as large as 32 km s^{-1}. This is caused by Hβ AGN residual emission swamping the Mg Ib and Fe stellar absorption features, leading to nonphysically high σ (see

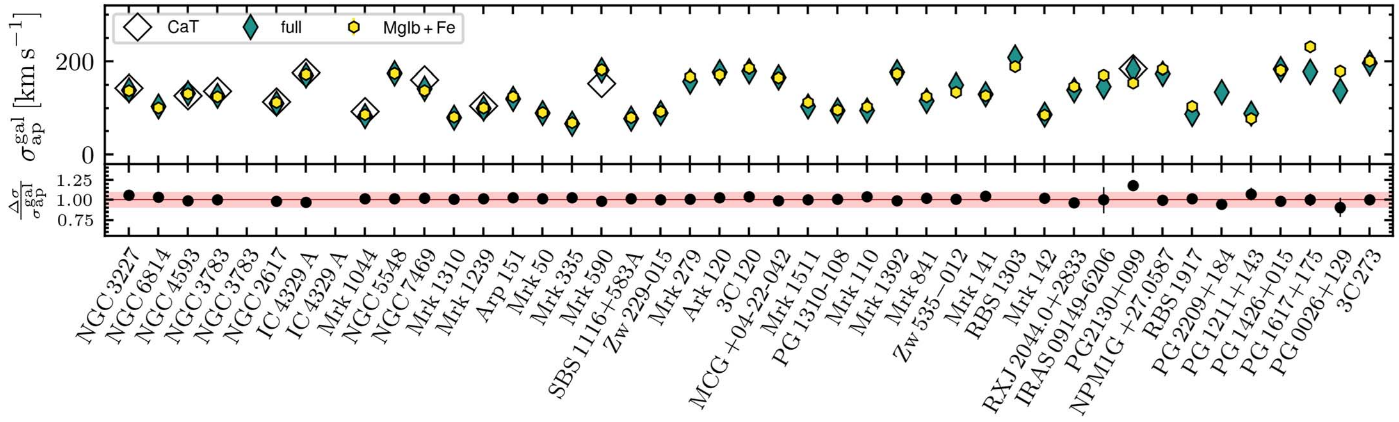

Figure 16. Comparison of extracting stellar velocity dispersion from different spectral windows. The top panel shows $\sigma_{\rm ap}^{\rm gal}$, the aperture-integrated dispersion from coadded spectra within and aperture matched to $R_{\rm eff}^{\rm gal}$, itemized after AGNs in the sample. Colors refer to the different spectral windows within which we measured $\sigma_{\rm ap}^{\rm gal}$. The bottom row shows the residual dispersion between measurements from Mg Ib vs. "full" measurements, with the 5% uncertainty, a typical uncertainty of $\sigma_{\rm ap}$, indicated by the shaded red stripe. The differences usually remain below the nominal uncertainties returned by `pPXF`. Mg Ib +Fe and full wavelength windows usually provide consistent within the 5% margin, and we consider both to be similarly robust and consistent tracers for the stellar kinematics across the sample.

Appendix B). A consistent choice of the wavelength range is therefore a trade-off between narrow wavelength ranges that provide more robust results in bright AGNs versus larger wavelength ranges that provide the more robust results in faint AGNs. Moreover, the coverage of stellar absorption features varies due to varying spectral coverage between the data sets used in this work; while CaT is available for almost all objects observed with MUSE, KCWI only covers the Mg Ib and Fe features. Overall, choosing the maximum common wavelength range between the data sets provides the best compromise between the three constraints. We therefore settled on using the wavelength range 4700 Å–5700 Å for the spectral synthesis modeling in Section 4.3.

Appendix F
Impact of Aperture Size on σ

As a primary objective of this work, we investigate the dependency of the $M_{\rm BH}$–$\sigma_\star$ relation on aperture size in Section 5.3. While the crucial role of aperture size on the spatially resolved kinematics of LTGs is discussed in Section 4.4.1, we here examine the effect of aperture size on measuring the aperture-integrated stellar velocity dispersion $\sigma_{\rm ap}$.

Figure 17 presents $\sigma_{\rm ap}$ for each AGN, measured from aperture-integrated spectra with aperture sizes corresponding to $R_{\rm eff}^{\rm bulge}$, $R_{\rm eff}^{\rm gal}$, or fixed to 3″ (corresponding to the SDSS fiber size). The distinction between bulge and galaxy is applicable only for LTGs, which have an identifiable disk component. For ETGs, $\sigma_{\rm ap}^{\rm gal}$ is the sole indicator of morphology-matched kinematics since no substructure is detected in these systems. Additionally, small bulge sizes in several galaxies precluded the measurement of $\sigma_{\rm ap}^{\rm bulge}$ on such small scales (e.g., for Mrk 1044; see also Section 5.3 and the discussion in Section 5.3.5). For the majority of AGNs, changing the aperture size has a marginal impact on the stellar kinematics. For ETGs, as long as $R_{\rm eff}^{\rm gal}$ is covered by the aperture, this is to be expected since their bright cores dominate the luminosity and kinematic profiles, which are typically covered by both the 3″ and $R_{\rm eff}^{\rm gal}$-matched aperture. For LTGs, using bulge- versus galaxy-size apertures makes a significant difference in approximately 50% of the cases. This can be understood from the aperture size-dependent profiles, shown in Figure 7. For

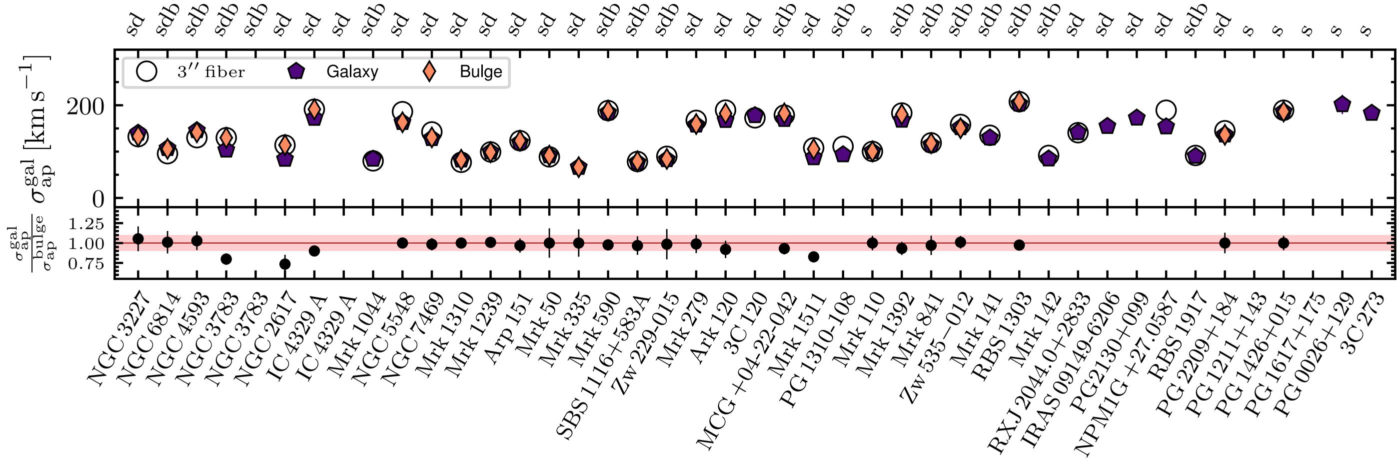

Figure 17. Comparing integrated $\sigma_{\rm ap}$ across different host-galaxy morphological components and aperture sizes. For each object, we show $\sigma_{\rm ap}$ color coded by the aperture size over which the host-galaxy emission was integrated prior to spectral synthesis modeling (see Section 4.1). The bottom panel shows the residual between $\sigma_{\rm ap}^{\rm bulge}$ and $\sigma_{\rm ap}^{\rm gal}$ for galaxies where we could robustly measure both quantities. For disk galaxies viewed at low inclination, $\sigma_{\rm ap}^{\rm bulge}$ is systematically larger than $\sigma_{\rm ap}^{\rm gal}$, a difference that can be as large as 40%.

LTGs viewed at high inclination, rotational broadening compensates for the drop of $\sigma_{\rm spat}$ on galaxy scales, resulting in a flat $\sigma_{\rm ap}$ profile. These are the galaxies for which $\sigma_{\rm ap}^{\rm gal} \approx \sigma_{\rm ap}^{\rm bulge}$. Conversely, if LTGs are observed at low inclination, e.g., NGC 3783, NGC 26717, or Mrk 1511, the high $\sigma_{\rm spat}$ in their centers contributes less and less with increasing aperture size, leading to $\sigma_{\rm ap}^{\rm gal} < \sigma_{\rm ap}^{\rm bulge}$. For individual AGNs in our sample, this effect can be as large as 30%, which is the dominant driver behind differing scaling relations inferred from $\sigma_{\rm spat}^{\rm gal}$ versus $\sigma_{\rm spat}^{\rm bulge}$ (see Section 5.3).

Appendix G

Comparing Stellar and SSP Libraries

To understand the robustness of our kinematic measurements, we have tested if the stellar kinematics are sensitive to the choice of stellar or SSP libraries used for fitting the spectra. In Figure 18, we show the velocity dispersion obtained from fitting AGNs' PSF-subtracted aperture-integrated spectra across the rest-frame 4700 Å–5700 Å wavelength range. We compared the kinematics recovered with templates from M11, Indo-U.S., and XSL. Motivated by the assumption that the light from the bulges of LTGs and ETGs in general is dominated by old stars, we also selected subsets of G and K giant stars from the XSL and Indo-U.S. libraries. Specifically, we selected temperatures $4400 < T_{\rm eff} < 5000$, surface gravity $0.15 < \log(g) < 3.59$, and metallicity $-2.5 < [{\rm Fe/H}] < 0.34$. We refer to these templates as XSL-GK and Indo-U.S.-GK, respectively.

We found that the systematic offsets in σ are typically $<10\,{\rm km\,s^{-1}}$ and therefore indistinguishable from the nominal uncertainties returned by `pPXF`. However, we recognized that, on an individual basis, the best-fit σ can differ by up to $30\,{\rm km\,s^{-1}}$. This is predominantly the case for objects for which the spectra have low S/N due to a strong AGN or a faint host galaxy (e.g., PG 2130+099). In these cases, the higher-resolution templates XSL and M11 provide consistent solutions, whereas the lower-resolution template spectra from Indo-U.S. lead to larger uncertainties. Overall, we do not recognize a significant systematic difference when constraining the library to G and K giants, possibly because the aperture covers the entire galaxy disk. However, stellar absorption features of Mg Ib and Fe are better modeled when choosing the full template library. We therefore prefer the XSL library, which we adopted for the spectral synthesis modeling in Section 4.3.

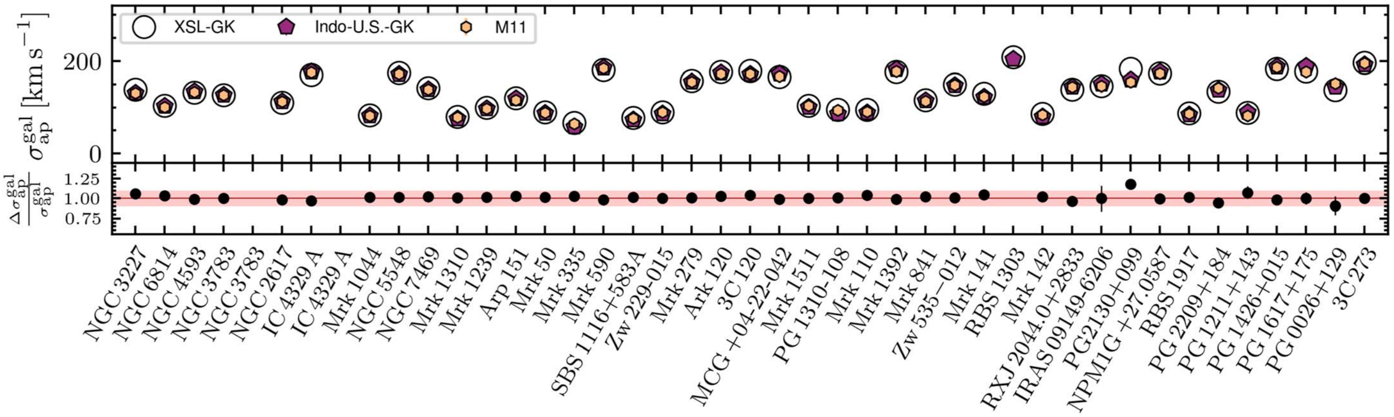

Figure 18. Comparing stellar and SSP libraries for $\sigma_{\rm ap}$ of individual AGNs. For each galaxy, we show the aperture-integrated galaxy stellar velocity, color coded by different template libraries used for the spectral synthesis modeling (see Section 4.3). The differences between the results are small, and typically range between $5\,{\rm km\,s^{-1}}$ and $10\,{\rm km\,s^{-1}}$.

Appendix H
Comparing Spectral Synthesis Modeling Codes

We have tested three different codes for fitting the stellar continuum via stellar population synthesis modeling. We employed `pPXF`, `PyParadise`, and `BADASS`, which differ in their fitting methodologies. `pPXF` and `PyParadise` fit the stellar continuum emission separately from narrow and broad emission lines, which need to be subtracted first. For the stellar continuum emission, `pPXF` describes large-scale continuum variations with a polynomial, whereas `PyParadise` first normalizes the continuum with a running mean before fitting kinematics with the normalized template spectra. This approach effectively removes nonphysical continuum variations caused by PSF subtraction with `QDeblend`$^{\mathrm{3D}}$. Since the continuum shape contains important information about the stellar populations (if AGN contamination is negligible), such a normalization removes information contained in the spectra and thus effectively reduces the S/N. As expected, we observed that the performance of each code depends on the respective data set. If the data set covers a large wavelength range, as is the case for the MUSE data sets, `PyParadise` produces more stable results. However, if the analysis is constrained to the wavelength range shared between KCWI, VIMOS, and MUSE, the polynomial used by `pPXF` provides sufficient accuracy to describe the nonphysical continuum variations. Moreover, `pPXF` tends to provide better fits at lower S/N compared to `PyParadise`, likely due to the S/N loss during continuum normalization in `PyParadise`. Since our analysis is constrained to the common wavelength range of 4700 Å–5700 Å, we adopted `pPXF` for our study. We note that, for individual AGNs, spurious spectral features near the galaxy need to be masked, otherwise they would dominate the continuum variation modeled with the polynomial (see Figure 3).

The full Bayesian analysis code, `BADASS`, offers a different approach to fitting AGN spectra. Unlike `pPXF` and `PyParadise`, which require the point-like AGN emission to be subtracted first, `BADASS` fits the AGN spectrum, emission-line templates, and stellar spectra simultaneously. An accurate knowledge of the AGN spectrum, combined with sophisticated coupling of the emission-line parameters, allows for the robust inference of emission-line and stellar-kinematic parameters across the FOV of the IFU. With this method, `BADASS` provides a fundamentally different approach that is independent of the PSF subtraction method. However, running the full Markov Chain Monte Carlo for `BADASS` is time consuming, and fine-tuning for individual AGNs is required, depending on the AGN spectral features, absorption line strength, and spectral masking. The details for individual AGNs will be presented in our companion paper (R. Remigio et al. 2024, in preparation). Here, we focus solely on the quantitative comparison of the inferred stellar kinematics parameters with those obtained using `pPXF`. Figure 19 shows the radial behavior of σ_{spat} for a subset of AGNs (chosen for good coverage within the effective radius to compare radial trends). We note that the same trends found for this subset also hold for a larger sample, which will be presented in R. Remigio et al. (2024 in preparation). Within the range where we can robustly measure σ_{spat}, the radial profiles extracted from `QDeblend`$^{\mathrm{3D}}$+`pPXF` are in agreement within the uncertainties. This suggests that the two independent methods provide consistent results, regardless of the distance from the AGN. We conclude that the method used to measure the stellar kinematics in Section 4.3 is robust. Furthermore, the nominal uncertainties returned by `pPXF` do not systematically underestimate the systematic uncertainties induced by the PSF subtraction with `QDeblend`$^{\mathrm{3D}}$.

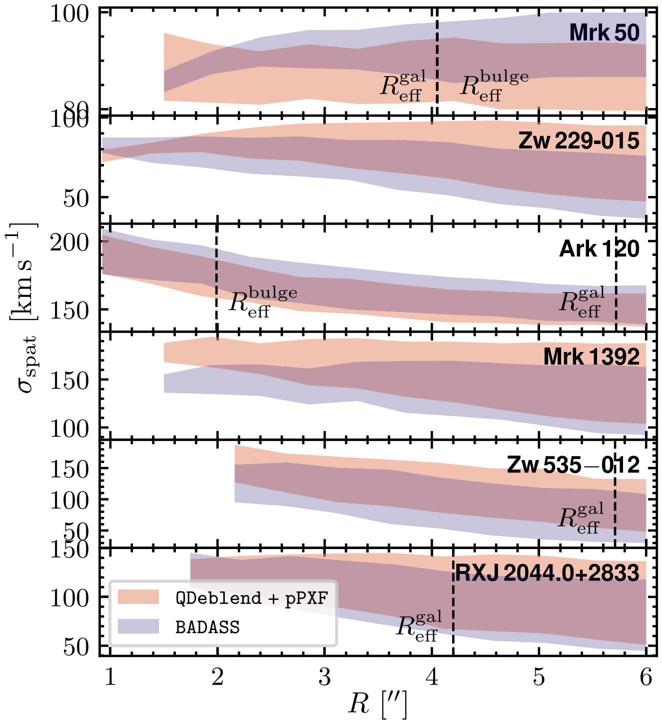

Figure 19. Comparing kinematics extracted using different spectral synthesis modeling codes. The panels show σ_{spat} for a subset of AGNs for which the spectra were also fitted by `BADASS`. Shades indicate the uncertainty range of the kinematic profile, and colors indicate the method by which we extracted σ_{spat}. Dashed lines indicate the bulge and galaxy effective radius. For the range across which we can measure σ_{spat}, the radial profiles extracted from `QDeblend`$^{\mathrm{3D}}$+`pPXF` agree within the uncertainties that we find when using `BADASS`.

ORCID iDs

Nico Winkel https://orcid.org/0000-0001-9428-6238
Vardha N. Bennert https://orcid.org/0000-0003-2064-0518
Raymond P. Remigio https://orcid.org/0000-0002-0164-8795
Tommaso Treu https://orcid.org/0000-0002-8460-0390
Knud Jahnke https://orcid.org/0000-0003-3804-2137
Vivian U https://orcid.org/0000-0002-1912-0024
Aaron J. Barth https://orcid.org/0000-0002-3026-0562
Matthew Malkan https://orcid.org/0000-0001-6919-1237
Bernd Husemann https://orcid.org/0000-0003-2901-6842
Xuheng Ding https://orcid.org/0000-0001-8917-2148
Simon Birrer https://orcid.org/0000-0003-3195-5507

References

Akritas, M. G., & Bershady, M. A. 1996, ApJ, 470, 706
Alonso, M. S., Coldwell, G., & Lambas, D. G. 2013, A&A, 549, A141
Ann, H. B., Seo, M., & Ha, D. K. 2015, ApJS, 217, 27
Astropy Collaboration, Robitaille, T. P., Tollerud, E. J., et al. 2013, A&A, 558, A33
Astropy Collaboration, Price-Whelan, A. M., Sipőcz, B. M., et al. 2018, AJ, 156, 123
Bahcall, J. N., Kirhakos, S., Saxe, D. H., & Schneider, D. P. 1997, ApJ, 479, 642
Barnes, J. E., & Hernquist, L. 1996, ApJ, 471, 115
Barth, A. J., Nguyen, M. L., Malkan, M. A., et al. 2011, ApJ, 732, 121

Barth, A. J., Bennert, V. N., Canalizo, G., et al. 2015, ApJS, 217, 26
Batiste, M., Bentz, M. C., Manne-Nicholas, E. R., Onken, C. A., & Bershady, M. A. 2017a, ApJ, 835, 271
Batiste, M., Bentz, M. C., Raimundo, S. I., Vestergaard, M., & Onken, C. A. 2017b, ApJL, 838, L10
Beifiori, A., Courteau, S., Corsini, E. M., & Zhu, Y. 2012, MNRAS, 419, 2497
Bellovary, J. M., Holley-Bockelmann, K., Gültekin, K., et al. 2014, MNRAS, 445, 2667
Bennert, V. N., Auger, M. W., Treu, T., Woo, J.-H., & Malkan, M. A. 2011, ApJ, 726, 59
Bennert, V. N., Treu, T., Auger, M. W., et al. 2015, ApJ, 809, 20
Bennert, V. N., Treu, T., Ding, X., et al. 2021, ApJ, 921, 36
Bentz, M. C., Denney, K. D., Grier, C. J., et al. 2013, ApJ, 767, 149
Bentz, M. C., Markham, M., Rosborough, S., et al. 2023a, ApJ, 959, 25
Bentz, M. C., Onken, C. A., Street, R., & Valluri, M. 2023b, ApJ, 944, 29
Bentz, M. C., Peterson, B. M., Netzer, H., Pogge, R. W., & Vestergaard, M. 2009a, ApJ, 697, 160
Bentz, M. C., Street, R., Onken, C. A., & Valluri, M. 2021a, ApJ, 906, 50
Bentz, M. C., Walsh, J. L., Barth, A. J., et al. 2009b, ApJ, 705, 199
Bentz, M. C., Williams, P. R., Street, R., et al. 2021b, ApJ, 920, 112
Bentz, M. C., Williams, P. R., & Treu, T. 2022, ApJ, 934, 168
Bernardi, M., Sheth, R. K., Tundo, E., & Hyde, J. B. 2007, ApJ, 660, 267
Birrer, S., & Amara, A. 2018, PDU, 22, 189
Blandford, R. D., & McKee, C. F. 1982, ApJ, 255, 419
Brewer, B. J., Treu, T., Pancoast, A., et al. 2011, ApJL, 733, L33
Bruzual, G., & Charlot, S. 2003, MNRAS, 344, 1000
Buta, R. J. 2019, MNRAS, 488, 590
Buta, R. J., Sheth, K., Athanassoula, E., et al. 2015, ApJS, 217, 32
Caglar, T., Burtscher, L., Brandl, B., et al. 2020, A&A, 634, A114
Caglar, T., Koss, M. J., Burtscher, L., et al. 2023, ApJ, 956, 60
Cappellari, M. 2017, MNRAS, 466, 798
Cappellari, M., & Copin, Y. 2003, MNRAS, 342, 345
Cappellari, M., & Emsellem, E. 2004, PASP, 116, 138
Cappellari, M., Bacon, R., Bureau, M., et al. 2006, MNRAS, 366, 1126
Cappellari, M., McDermid, R. M., Alatalo, K., et al. 2013, MNRAS, 432, 1862
Cardelli, J. A., Clayton, G. C., & Mathis, J. S. 1989, ApJ, 345, 245
Chilingarian, I. V., Katkov, I. Y., Zolotukhin, I. Y., et al. 2018, ApJ, 863, 1
Cisternas, M., Jahnke, K., Bongiorno, A., et al. 2011a, ApJL, 741, L11
Cisternas, M., Jahnke, K., Inskip, K. J., et al. 2011b, ApJ, 726, 57
Comeron, S., Knapen, J. H., Beckman, J. E., et al. 2010, MNRAS, 402, 2462
Courteau, S., Cappellari, M., de Jong, R. S., et al. 2014, RvMP, 86, 47
Croton, D. J. 2006, MNRAS, 369, 1808
Dalla Bontà, E., Peterson, B. M., Bentz, M. C., et al. 2020, ApJ, 903, 112
Davies, R. I., Thomas, J., Genzel, R., et al. 2006, ApJ, 646, 754
de Nicola, S., Marconi, A., & Longo, G. 2019, MNRAS, 490, 600
de Vaucouleurs, G., de Vaucouleurs, A., Corwin, H. G., J., et al. 1991, Third Reference Catalogue of Bright Galaxies (New York, NY: Springer)
Debattista, V. P., Kazantzidis, S., & van den Bosch, F. C. 2013, ApJ, 765, 23
Di Matteo, T., Springel, V., & Hernquist, L. 2005, Natur, 433, 604
Ding, X., Silverman, J., Treu, T., et al. 2020, ApJ, 888, 37
Ding, X., Onoue, M., Silverman, J. D., et al. 2023, Natur, 621, 51
Du, P., Hu, C., Lu, K.-X., et al. 2015, ApJ, 806, 22
Dubois, Y., Devriendt, J., Slyz, A., & Teyssier, R. 2012, MNRAS, 420, 2662
Dubois, Y., Pichon, C., Devriendt, J., et al. 2013, MNRAS, 428, 2885
El-Badry, K., Quataert, E., Wetzel, A., et al. 2018, MNRAS, 473, 1930
Emsellem, E., Cappellari, M., Krajnovi, D., et al. 2007, MNRAS, 379, 401
Emsellem, E., Cappellari, M., Krajnovic, D., et al. 2011, MNRAS, 414, 888
Erwin, P. 2019, MNRAS, 489, 3553
Eskridge, P. B., Frogel, J. A., Pogge, R. W., et al. 2000, AJ, 119, 536
Falcón-Barroso, J., Lyubenova, M., van de Ven, G., et al. 2017, A&A, 597, A48
Fausnaugh, M. M., Grier, C. J., Bentz, M. C., et al. 2017, ApJ, 840, 97
Ferrarese, L., & Merritt, D. 2000, ApJL, 539, L9
Ferrarese, L., Pogge, R. W., Peterson, B. M., et al. 2001, ApJL, 555, L79
Ferreira, L., Conselice, C. J., Sazonova, E., et al. 2023, ApJ, 955, 94
Gadotti, D. A., Bittner, A., Falcón-Barroso, J., et al. 2020, A&A, 643, A14
Gannon, J. S., Forbes, D. A., Romanowsky, A. J., et al. 2020, MNRAS, 495, 2582
García-Burillo, S., Combes, F., Schinnerer, E., Boone, F., & Hunt, L. K. 2005, A&A, 441, 1011
Gebhardt, K., Bender, R., Bower, G., et al. 2000, ApJL, 539, L13
Graham, A. W. 2008, ApJ, 680, 143
Graham, A. W. 2023, MNRAS, 518, 6293
Graham, A. W., Onken, C. A., Athanassoula, E., & Combes, F. 2011, MNRAS, 412, 2211
GRAVITY Collaboration, Sturm, E., Dexter, J., et al. 2018, Natur, 563, 657
GRAVITY Collaboration, Amorim, A., Bauböck, M., et al. 2020, A&A, 643, A154
GRAVITY Collaboration, Amorim, A., Bauböck, M., et al. 2021, A&A, 654, A85
GRAVITY Collaboration, Amorim, A., Bourdarot, G., et al. 2024, A&A, 684, A167
Greene, J. E., & Ho, L. C. 2005a, ApJ, 630, 122
Greene, J. E., & Ho, L. C. 2005b, ApJ, 630, 122
Greene, J. E., & Ho, L. C. 2007, ApJ, 670, 92
Greene, J. E., Peng, C. Y., Kim, M., et al. 2010, ApJ, 721, 26
Grier, C. J., Pancoast, A., Barth, A. J., et al. 2017, ApJ, 849, 146
Grier, C. J., Peterson, B. M., Pogge, R. W., et al. 2012, ApJ, 755, 60
Grier, C. J., Martini, P., Watson, L. C., et al. 2013, ApJ, 773, 90
Gültekin, K., Richstone, D. O., Gebhardt, K., et al. 2009, ApJ, 698, 198
Häring, N., & Rix, H.-W. 2004, ApJL, 604, L89
Harris, C. E., Bennert, V. N., Auger, M. W., et al. 2012, ApJS, 201, 29
Harrison, C. M. 2017, NatAs, 1, 0165
Hartmann, M., Debattista, V. P., Cole, D. R., et al. 2014, MNRAS, 441, 1243
Hickox, R. C., Mullaney, J. R., Alexander, D. M., et al. 2014, ApJ, 782, 9
Hirschmann, M., Khochfar, S., Burkert, A., et al. 2010, MNRAS, 407, 1016
Ho, L. C., & Kim, M. 2014, ApJ, 789, 17
Hopkins, P. F., Robertson, B., Krause, E., Hernquist, L., & Cox, T. J. 2006, ApJ, 652, 107
Horne, K., Peterson, B. M., Collier, S. J., & Netzer, H. 2004, PASP, 116, 465
Hu, C., Li, S.-S., Yang, S., et al. 2021, ApJS, 253, 20
Hu, J. 2008, MNRAS, 386, 2242
Husemann, B., Bennert, V. N., Scharwächter, J., Woo, J. H., & Choudhury, O. S. 2016a, MNRAS, 455, 1905
Husemann, B., Jahnke, K., Sanchez, S. F., et al. 2014, MNRAS, 443, 755
Husemann, B., Scharwächter, J., Bennert, V. N., et al. 2016b, A&A, 594, A44
Husemann, B., Wisotzki, L., Sánchez, S. F., & Jahnke, K. 2013, A&A, 549, A43
Husemann, B., Bennert, V. N., Jahnke, K., et al. 2019, ApJ, 879, 75
Husemann, B., Singha, M., Scharwächter, J., et al. 2022, A&A, 659, A124
Jacobs, C., Glazebrook, K., Calabrò, A., et al. 2023, ApJL, 948, L13
Jahnke, K., Kuhlbrodt, B., & Wisotzki, L. 2004, MNRAS, 352, 399
Jahnke, K., & Macciò, A. V. 2011, ApJ, 734, 92
Jorgensen, I., Franx, M., & Kjaergaard, P. 1995, MNRAS, 276, 1341
Kaspi, S., Smith, P. S., Netzer, H., et al. 2000, ApJ, 533, 631
Kelly, B. C. 2007, ApJ, 665, 1489
Kim, M., Barth, A. J., Ho, L. C., & Son, S. 2021, ApJS, 256, 40
King, A. 2003, ApJL, 596, L27
Kocevski, D. D., Faber, S. M., Mozena, M., et al. 2012, ApJ, 744, 148
Kormendy, J. 2020, in IAU Symp. Vol. 353, Galactic Dynamics in the Era of Large Surveys, ed. M. Valluri & J. A. Sellwood (Cambridge: Cambridge Univ. Press), 186
Kormendy, J., Bender, R., & Cornell, M. E. 2011, Natur, 469, 374
Kormendy, J., & Ho, L. C. 2013, ARA&A, 51, 511
Kormendy, J., & Kennicutt, R. C., J. 2004, ARA&A, 42, 603
Kormendy, J., & Richstone, D. 1995, ARA&A, 33, 581
Lauer, T. R., Tremaine, S., Richstone, D., & Faber, S. M. 2007, ApJ, 670, 249
Le Fèvre, O., Saisse, M., Mancini, D., et al. 2003, Proc. SPIE, 4841, 1670
Lelli, F., Di Teodoro, E. M., Fraternali, F., et al. 2021, Sci, 371, 713
Li, J., Silverman, J. D., Ding, X., et al. 2021, ApJ, 922, 142
Li, Y.-R., Wang, J.-M., Ho, L. C., Du, P., & Bai, J.-M. 2013, ApJ, 779, 110
Li, Y.-R., Wang, J.-M., Songsheng, Y.-Y., et al. 2022, ApJ, 927, 58
Li, Y.-R., Songsheng, Y.-Y., Qiu, J., et al. 2018, ApJ, 869, 137
Lu, K.-X., Wang, J.-G., Zhang, Z.-X., et al. 2021, ApJ, 918, 50
Magorrian, J., Tremaine, S., Richstone, D., et al. 1998, AJ, 115, 2285
Maraston, C., & Stromback, G. 2011, MNRAS, 418, 2785
Marconi, A., & Hunt, L. K. 2003, ApJL, 589, L21
Marian, V., Jahnke, K., Mechtley, M., et al. 2019, ApJ, 882, 141
Martel, A. R., Ford, H. C., Tran, H. D., et al. 2003, AJ, 125, 2964
Massonneau, W., Volonteri, M., Dubois, Y., & Beckmann, R. S. 2023, A&A, 670, A180
McConnell, N. J., & Ma, C.-P. 2013, ApJ, 764, 184
McLeod, K. K., & McLeod, B. A. 2001, ApJ, 546, 782
Mechtley, M., Jahnke, K., Windhorst, R. A., et al. 2016, ApJ, 830, 156
Mehlert, D., Thomas, D., Saglia, R. P., Bender, R., & Wegner, G. 2003, A&A, 407, 423
Merloni, A. 2004, MNRAS, 353, 1035
Merritt, D., & Ferrarese, L. 2001, ApJ, 547, 140
Mo, H., Chen, Y., & Wang, H. 2024, MNRAS, 532, 3808
Molina, J., Ho, L. C., & Knudsen, K. K. 2024, A&A, 691, A114
Morrissey, P., Matuszewski, M., Martin, D. C., et al. 2018, ApJ, 864, 93
Mullaney, J. R., Alexander, D. M., Fine, S., et al. 2013, MNRAS, 433, 622

Nair, P. B., & Abraham, R. G. 2010, ApJS, 186, 427
Nelson, C. H., Green, R. F., Bower, G., Gebhardt, K., & Weistrop, D. 2004, ApJ, 615, 652
Nelson, C. H., & Whittle, M. 1995, ApJS, 99, 67
Onken, C. A., Ferrarese, L., Merritt, D., et al. 2004, ApJ, 615, 645
Pancoast, A., Brewer, B. J., & Treu, T. 2011, ApJ, 730, 139
Pancoast, A., Brewer, B. J., Treu, T., et al. 2014, MNRAS, 445, 3073
Pancoast, A., Barth, A. J., Horne, K., et al. 2018, ApJ, 856, 108
Park, D., Kelly, B. C., Woo, J.-H., & Treu, T. 2012, ApJS, 203, 6
Pei, L., Fausnaugh, M. M., Barth, A. J., et al. 2017, ApJ, 837, 131
Peng, C. Y. 2007, ApJ, 671, 1098
Peterson, B. M. 1993, PASP, 105, 247
Peterson, B. M., Wanders, I., Bertram, R., et al. 1998, ApJ, 501, 82
Peterson, B. M., Ferrarese, L., Gilbert, K. M., et al. 2004, ApJ, 613, 682
Pichon, C., Pogosyan, D., Kimm, T., et al. 2011, MNRAS, 418, 2493
Pinkney, J., Gebhardt, K., Bender, R., et al. 2003, ApJ, 596, 903
Planck Collaboration, Ade, P. A. R., Aghanim, N., et al. 2016, A&A, 594, A13
Richards, G. T., Lacy, M., Storrie-Lombardi, L. J., et al. 2006, ApJS, 166, 470
Richards, G. T., Kruczek, N. E., Gallagher, S. C., et al. 2011, AJ, 141, 167
Robertson, B., Hernquist, L., Cox, T. J., et al. 2006, ApJ, 641, 90
Robertson, B. E., Tacchella, S., Johnson, B. D., et al. 2023, ApJL, 942, L42
Roman-Oliveira, F., Fraternali, F., & Rizzo, F. 2023, MNRAS, 521, 1045
Saglia, R. P., Opitsch, M., Erwin, P., et al. 2016, ApJ, 818, 47
Sahu, N., Graham, A. W., & Davis, B. L. 2019, ApJ, 887, 10
Salvato, M. 2002, PhD thesis, Univ. Potsdam, Germany
Savorgnan, G. A. D., & Graham, A. W. 2015, MNRAS, 446, 2330
Schawinski, K., Koss, M., Berney, S., & Sartori, L. F. 2015, MNRAS, 451, 2517
Schawinski, K., Simmons, B. D., Urry, C. M., Treister, E., & Glikman, E. 2012, MNRAS, 425, L61
Schlafly, E. F., & Finkbeiner, D. P. 2011, ApJ, 737, 103
Schulze, A., & Wisotzki, L. 2010, A&A, 516, A87
Schulze, A., & Wisotzki, L. 2011, A&A, 535, A87
Schulze, A., Bongiorno, A., Gavignaud, I., et al. 2015, MNRAS, 447, 2085
Sexton, R. O., Matzko, W., Darden, N., Canalizo, G., & Gorjian, V. 2021, MNRAS, 500, 2871
Shankar, F., Bernardi, M., Sheth, R. K., et al. 2016, MNRAS, 460, 3119
Shankar, F., Bernardi, M., Richardson, K., et al. 2019, MNRAS, 485, 1278
Shankar, F., Weinberg, D. H., Marsden, C., et al. 2020, MNRAS, 493, 1500
Shen, Y., Grier, C. J., Horne, K., et al. 2024, ApJS, 272, 26
Silk, J., & Rees, M. J. 1998, A&A, 331, L1
Skielboe, A., Pancoast, A., Treu, T., et al. 2015, MNRAS, 454, 144
Slavcheva-Mihova, L., & Mihov, B. 2011, A&A, 526, A43
Somerville, R. S., Hopkins, P. F., Cox, T. J., Robertson, B. E., & Hernquist, L. 2008, MNRAS, 391, 481
Storey, P. J., & Zeippen, C. J. 2000, MNRAS, 312, 813
Tremaine, S., Gebhardt, K., Bender, R., et al. 2002, ApJ, 574, 740
Treu, T., Malkan, M. A., & Blandford, R. D. 2004, ApJL, 615, L97
Treu, T., Woo, J.-H., Malkan, M. A., & Blandford, R. D. 2007, ApJ, 667, 117
U, V., Barth, A. G., Vogler, H. A., et al. 2022, ApJ, 925, 52
Valdes, F., Gupta, R., Rose, J. A., Singh, H. P., & Bell, D. J. 2004, ApJS, 152, 251
van den Bosch, R. C. E. 2016, ApJ, 831, 134
Verro, K., Trager, S. C., Peletier, R. F., et al. 2022, A&A, 660, A34
Vestergaard, M., & Peterson, B. M. 2006, ApJ, 641, 689
Villafaña, L., Williams, P. R., Treu, T., et al. 2022, ApJ, 930, 52
Villafaña, L., Williams, P. R., Treu, T., et al. 2023, ApJ, 948, 95
Villar-Martin, M., Arribas, S., Emonts, B., et al. 2016, MNRAS, 460, 130
Virtanen, P., Gommers, R., Oliphant, T. E., et al. 2020, NatMe, 17, 261
Volonteri, M., & Natarajan, P. 2009, MNRAS, 400, 1911
Watson, L. C., Martini, P., Dasyra, K. M., et al. 2008, ApJL, 682, L21
Weilbacher, P. M., Palsa, R., Streicher, O., et al. 2020, A&A, 641, A28
Williams, P. R., & Treu, T. 2022, ApJ, 935, 128
Williams, P. R., Pancoast, A., Treu, T., et al. 2018, ApJ, 866, 75
Williams, P. R., Pancoast, A., Treu, T., et al. 2020, ApJ, 902, 74
Winkel, N., Husemann, B., Davis, T. A., et al. 2022, A&A, 663, A104
Wisotzki, L., Christlieb, N., Bade, N., et al. 2000, A&A, 358, 77
Woo, J.-H., Schulze, A., Park, D., et al. 2013, ApJ, 772, 49
Woo, J.-H., Yoon, Y., Park, S., Park, D., & Kim, S. C. 2015, ApJ, 801, 38
Woo, J.-H., Treu, T., Barth, A. J., et al. 2010, ApJ, 716, 269
Xiao, T., Barth, A. J., Greene, J. E., et al. 2011, ApJ, 739, 28
Zhang, Z.-X., Du, P., Smith, P. S., et al. 2019, ApJ, 876, 49
Zhu, K., Li, R., Cao, X., et al. 2023, RAA, 23, 085001
Zou, F., Yu, Z., Brandt, W. N., et al. 2024, ApJ, 964, 183